NOVA SCHOOL OF SCIENCE & TECHNOLOGY

DEPARTMENT OF PHYSICS

RICARDO MIGUEL FERREIRA BISPO CASTELHANO

Bachelor in Sciences of Biomedical Engineering

Effects of formalin fixation in soft tissue light element composition by PIGE analysis

MASTER IN BIOMEDICAL ENGINEERING

NOVA University Lisbon

September, 2022

NOVA SCHOOL OF SCIENCE & TECHNOLOGY

DEPARTMENT OF PHYSICS

Effects of formalin fixation in soft tissue light element composition by PIGE analysis

RICARDO MIGUEL FERREIRA BISPO CASTELHANO

Bachelor in Sciences of Biomedical Engineering

Adviser: Prof. Dr. João Duarte Neves Cruz
Associate Professor, NOVA School of Science and Technology

Co-adviser: Prof. Dr. Jorge Felizardo Dias Cunha Machado
Principal Researcher, NOVA School of Science and Technology

Examination Committee

Chair: Dr. Maria de Fátima Guerreiro da Silva Campos Raposo
Associate Professor, NOVA SST

Rapporteur: Dr. Ana Luísa Monteiro da Silva
Auxiliary Professor, Universidade de Aveiro

Adviser: Dr. João Duarte Neves Cruz
Associate Professor, NOVA SST

MASTER IN BIOMEDICAL ENGINEERING

NOVA University Lisbon
September, 2022

Effects of formalin fixation in soft tissue light element composition by PIGE analysis

This document was created with the (pdf/Xe/Lua)LaTeX processor and the NOVAthesis template (v6.9.4) [1].

To my grandparents, Margarida and Manuel.

Acknowledgements

Over the course of this master's thesis' development, a lot of resilience and sacrifice were needed in order to cope with stress and sleepless nights. If it wasn't for the presence of so many supportive people around me, this project wouldn't have been as successful as it was.

Firstly, I would like to thank my adviser, Professor João Cruz, for the unceasing amount of support, availability and patience throughout the last few months, whether by meeting promptly with me to help in any way he could or by spending countless hours with me in the accelerator. The company, the coffee and the pizza were also very nice. I would also like to thank my co-adviser, Professor Jorge Machado, Professor Sofia Pessanha and my colleague João Silva for helping with the sample acquisition and preparation and always welcoming me warmly in their work environment. Last but not least, and on a very special note, I would like to thank Professor Adelaide Jesus for allowing this project to happen in the first place. Without her availability, this thesis would not exist right now.

A very heartfelt and tender thank you to all my family, for constantly listening to me complaining about how much work I had to do and for supporting me in every step of this journey. To my mother, for being my source of inspiration to go the extra mile in all aspects of my life and for being my most loyal friend; to my father, for his everlasting witty personality and companionship and for helping me relax when times got tough; to my sister, for all the good moments and for helping me with her sarcasm and irony in the midst of chaos.

I would also like to thank my Physics and Biomedical Engineering friends for turning the last 5 years into an unforgettable experience and for being such faithful friends along the way.

To my childhood friends, and in no particular order, Vasco, Lua, Calado, David and Tomás, thank you for being the most loyal friends in the world. Thank you for all the laughter, for all the improvised plans, for being there in the best and worst of times and for the memories that were and will be.

To Maria, the **b**est friend these last 5 years c**o**uld have given me, thank y**o**u for becoming such a huge part of my life and for being my partner in crime every single day. Without your humour and silliness to distract me, this journey would have been much harder.

Finally, a very big thank you to my very good friends Silva, Paulino, Tomás, Afonso and Queiroz. All of you became a constant presence in my daily life and for that I could not be more grateful. Thank you for all the moments we shared, for clearing my head after those hard days and for all the (many) drinks we had together.

"When you reach the end of your rope, tie a knot in it and hang on." (Franklin D. Roosevelt)

Abstract

Cancer has been one of the most deadly and prevalent diseases of modern society, and its genesis and treatments are still not fully comprehended to this day. The scientific community has taken great interest in better understanding elementary tissue changes that might correlate to carcinogenesis.

Particle Induced Gamma-ray Emission (PIGE) is an ion beam analysis (IBA) technique very suitable for biological sample analysis due to its great sensitivity for light elements of interest. Resorting to biopsied human tissue samples stored in formalin, made available by institutions dedicated to cancer studies such as Instituto Português de Oncologia (IPO), it is possible to quantify said light elements and describe how formalin influences the samples' elementary matrix.

This thesis sought to employ a quantification method based on backscattering and gamma spectra analysis to accurately describe the behaviour of light elements in formalin-fixated samples.

The developed work included successful measurements of sodium and phosphorus in colon, ileon, spleen and muscle tissue samples. For the organ samples, both sodium and phosphorus presented, on average, a very large increase of concentration after a few days in formalin, that would either plateau or decline over longer periods of time. For muscle tissue, since the formalin fixation (FF) times were much shorter, it was possible to witness a sudden and steep sodium and phosphorus concentration increase in the first few minutes of FF.

Future work aims to improve upon a few analysis methods used throughout this thesis, as well as acquiring further data to fill out some important data gaps and to validate the current results for these and more types of biological tissue.

Keywords: Cancer, PIGE, FF, IPO, Sodium, Phosphorus

Resumo

O cancro tem sido uma das doenças mais prevalentes e mortais da sociedade moderna, e a sua génese e tratamentos ainda não são completamente compreendidos. A comunidade científica tem gerado um grande interesse no entendimento das alterações elementares ao nível dos tecidos biológicos que possam estar por detrás da carcinogénese.

A emissão de raios-gama induzida por partículas (PIGE) é uma técnica de análise por feixe de iões muito indicada ao estudo de amostras de tecido biológico, dada a sua elevada sensibilidade a elementos leves de interesse. Recorrendo a amostras de biópsia de tecido humano preservadas em formol, fornecidas por institutos dedicados ao estudo do cancro como o IPO, é possível quantificar esses mesmos elementos leves e descrever a influência do formol na matriz elementar dessas amostras.

Esta tese procurou empregar um método de quantificação baseado na análise de espetros gama e de retrodispersão de partículas, de modo a descrever com precisão o comportamento de elementos leves em amostras fixadas em formol.

Os resultados deste trabalho incluíram medidas de sódio e fósforo em amostras de colon, íleo, baço e tecido muscular. Para as amostras de órgãos, tanto o sódio como o fósforo apresentaram, em média, um grande aumento de concentração após alguns dias de fixação em formol, cuja tendência era manter-se ou diminuir para períodos de tempo mais longos. Para o tecido muscular, como os tempos de fixação foram muito mais curtos, foi possível observar um aumento intenso e repentino da concentração de sódio e fósforo nos primeiros minutos de fixação.

Perspetivas futuras incluem o aperfeiçoamento de alguns métodos de análise usados ao longo desta tese, tal como a aquisição de mais amostras que permitam complementar falhas de informação e que permitam validar os resultados atuais para estes e mais tipos de tecidos biológicos.

Palavras-chave: Cancro, PIGE, Formol, IPO, Sódio, Fósforo

Contents

List of Figures

List of Tables

Acronyms

CS Compton scattering 18–20, 22

EBS Elastic backscattering spectrometry xix, 14, 16, 17, 36–38, 40, 44, 47, 62, 66
ERYA Emitted Radiation Yield Analysis 2, 24, 44, 62

FF formalin fixation xi, 2, 25–27, 29, 47–50, 53, 54, 56, 57, 59, 61, 65

IBA ion beam analysis xi, 1, 26
IPO Instituto Português de Oncologia xi, xiii, 2

NKA Na,K-ATPases 3, 4

OCT optimal cutting temperature 7

PE photoelectric effect 18
PIGE Particle Induced Gamma-ray Emission xi, xiii, 1, 2, 22, 27, 30, 38, 47, 65
PIXE Particle Induced X-ray Emission 22, 27
PMF Phosphorus mass fraction 56, 57, 59, 61
PP pair production 18, 21, 22

RBS Rutherford backscattering spectrometry 16

SMF Sodium mass fraction 48–50, 53, 54, 56, 61
SRIXE Synchrotron Radiation Induced X-ray Emission 27

TXRF Total Reflection X-ray Fluorescence 27

XRF X-ray fluorescence 2, 26, 27, 29, 65

1 Introduction

1.1 Motivation and context

Cancer is one of the most prevalent diseases in society, as well as one of the deadliest, on a global scale. Carcinogenesis consists on fundamental changes to the metabolic processes in the cells. These changes promote a chaotic and uncontrolled proliferation of these cells, sometimes leading to their migration to other organs or regions of the body. This migration flux is called metastization [2].

In 2018, demographic studies point to 18.1 million new cases of cancer being diagnosed and 9.6 million deaths being registered, as a consequence of this disease [3]. These numbers have grown in severity more recently, especially in 2020, in which 19.3 million new cases and 10.0 million deaths were registered. In that year, the cancers with the most number of diagnostics were breast cancer, rectal cancer and lung cancer. The latter two are also among the most lethal, followed by stomach and liver cancer. According to the current demographic trends, a rise to 28.4 million new yearly cases by 2040 is foreseeable, which translates to an increase of 47% in comparison to the cases registered in 2020 [4, 5].

With this in mind, one of the essential steps to understand the evolution of this pathology is to try to establish a correlation between the development of cancer and the elementary composition of the affected tissues. Currently, there is a considerable focus in the study of the biological concentration of trace elements, such as arsenic, zinc, selenium and iron [6].

The IBA technique PIGE has been used to study and quantify light elements in solid samples. This technique allows for the study of biological tissue composition through biopsy samples [7, 8].

However, one can only proceed with this type of analysis after collecting biopsy specimens under the form of tissue sections. Normally, these samples are fixated in formalin, which is the traditional preservation method used to preserve the tissue architecture and its biological properties [9]. This interaction between the cancer tissue and the formalin in which it is fixated may result in elementary losses under the form of depletion of

metabolites with functional groups [10]. Hence, it is necessary the evaluate the temporal evolution of the elementary trade-offs between the formalin and the tissues.

1.2 Objectives and approach

The main goal of this dissertation is to parameterise the elementary content of several formalin fixated biological samples, throughout variable and increasing time intervals.

This work aims to corroborate previous studies in which other analytical techniques like X-ray fluorescence (XRF) were used to quantify heavier elements. PIGE will prove as a resourceful technique by allowing the measurement of lighter elements, like Na, F, Al and P. A previous study brought forth by LIBPhys concluded there was a change in elementary content in biological tissue, after 3 days of FF. Hence, studying sodium variations between fresh tissue and formalin-fixated tissue will be the main focus of this work.

The development of this thesis seeks the analysis of non-pathological tissue samples, as these were the ones made available by IPO. Therefore, results taken from this work will lay the foundation for preliminary conclusions on how FF affects the elementary composition of biological tissue. Later on, these results may be used and taken into consideration when studying pathological samples, effectively bridging the gap to allow for an in-depth elementary cancer study.

Since PIGE is a multi-element technique, it will be possible to establish several relations between sodium and other light elements present in the tissue samples, as a means to understand if there is any element migration to the formalin or the other way around.

For absolute measurements, *software* Emitted Radiation Yield Analysis (ERYA)-Bulk (for homogeneous samples) will be utilized. Given the yield of the occurring nuclear reactions, this *software* can calculate the mass and atomic fractions of an element in that specific specimen [11].

2

Theoretical concepts

2.1 Medical and Biological concepts

This section provides an overview of the fundamental concepts necessary to understand how human tissue works on a molecular level and its respective treatment and preparation procedures.

2.1.1 Cellular Na-K mechanisms

The regulation and exchange of sodium (Na^+) and potassium (K^+) ions between the intracellular and extracellular environments are the base mechanisms of physiological cellular activity in human tissues. These ionic exchange mechanisms are responsible for activities mediated by physiological stimuli, like water and ion cell content homeostasis, polarization and depolarization of the cellular membranes and transportation of various substances tethered to the Na^+ ion. The outcome of these mechanisms will be the maintenance of functions such as neural activity, muscular contraction and body water content regulation [12].

Intracellular and extracellular Na^+ and K^+ equilibrium is mediated by transmembrane proteins called Na,K-ATPases (NKA), through hydrolysis of ATP. These proteins are heterodimers, that is, they are made of two distinct subunits, α and β, which have, respectively, 4 and 3 isoforms. The isoforms have minor structural differences between themselves, and each α/β isoform combination has certain physiological specificities. On the one hand, subunit α is dominantly responsible for catalytic activity, which is to say the movement of ions in and out of the cell. On the other hand, subunit β does not have any catalytic activity role, but is essential to the formation, maturation and function of these ATPases [12, 13]. The enzymatic and ionic cycle of a NKA is represented in figure 2.1.

2.1.1.1 Skeletal muscle regulation

Many data sets analyzed throughout this work were comprised of muscle samples. Knowing how ionic regulation works in this tissue is, therefore, relevant and important.

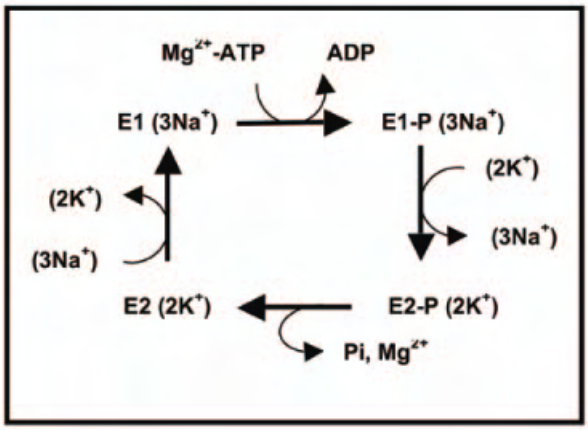

Figure 2.1: Enzymatic cycle of a Na,K-ATPase. E1 and E2 refer to changes in the conformation of the ATPase. Retrieved from [13].

NKA activation in the skeletal muscles essentially depends on 3 factors: the NKAs' intrinsic activity, the abundance of NKAs in the plasmatic membrane and the total number of NKAs in the skeletal muscle. Intrinsic activity of the NKAs and its abundance in the plasmatic membrane of the cells result from the adaptation and fluctuation of Na^+ and K^+ transportation, for example, after a meal or during peak physical performance. The total number of NKAs in the skeletal muscle is associated with a chronic adaptation of Na^+ and K^+ transportation, influenced by eating habits or regular physical exercise [12].

The enzymatic activity of a single NKA is directly dependant of Na^+ and ATP levels in the cytosol and K^+ levels in the extracellular environment [14]. During physical exercise, NKA activation opposes K^+ and Na^+ flux through the sarcolemma, preserving muscular contractility. Additionally, by limiting K^+ losses, NKA activity helps to prevent exercise-induced hyperkalemias. Hormones also play a big role with regard to NKA activity. Insulin, as an example, controls K^+ levels, promoting an increased absorption of that ion to the inside of the cell. Other hormones, such as amylin and epinephrine also stimulate the NKAs [12].

2.1.1.2 Renal regulation

The main function of NKAs in the nephrons is to maintain the electrochemical gradients of sodium through active transport, which contributes to the water and salt homeostasis in the body [15, 16].

In all sodium reabsorption renal epithelium, more specifically in the tubular cells, the NKAs are located in the basolateral membrane. The activity of these NKAs naturally creates a Na^+ gradient, which is only dissipated throughout the apical membrane, where there are multiple sodium entryways. This process facilitates the reabsorption mechanism, since a higher number of entryways promotes a high number of ions moved by active transport [15–17].

2.1.2 Major, Minor and Trace elements

The human body is made of a large variety of elements. These can be divided into categories according to their abundance: major elements, minor elements and trace elements. Major elements are, specifically, hydrogen (H), oxygen (O), carbon (C), nitrogen (N), calcium (Ca) and phosphorus (P) whereas minor elements are sulfur (S), sodium (Na), potassium (K), magnesium (Mg), chlorine (Cl) and silicon (Si). These elements add up to 98.8 % of the human organism. Trace elements are designated this way due to their low concentrations in the human body. Trace elements concentrations can vary between 0.01 and 100 mgkg^{-1}. whereas concentration of major and minor elements is in the gkg^{-1} range. Tables 2.1 and 2.2 present standard values for these elements.

Table 2.1: Concentration of major and minor elements (standard values). Retrieved from [18].

Major elements	%	Minor elements	%
O	61	S	0.2
C	23	K	0.2
H	10	Na	1.4
N	2.6	Cl	1.2
Ca	1.4	Mg	0.03
P	1.1	Si	0.03

Table 2.2: Concentrarion range of trace elements in the human body. Retrieved from [18].

Trace elements	mgkg^{-1}
Fe, F, Zn	100.0
Rb, Sr, Cu, Pb, Br	10.0
Sn, Sc, Cd, Mn, Ba, Al	1.0
Cs, Co, Cr, Mo, Au, Ni	0.1

Trace elements can be classified according to their role in the body and how they're involved in the metabolism. They can be essential, potentially essential or toxic, even though there is toxicity associated with every trace element in case of high exposure or excessive consumption for long periods of time [18].

2.1.2.1 Essential trace elements

Essential trace elements include cromium, iron, cobalt, copper, zinc, selenium, molibdenium and iodine. The daily necessary intake values for each one of them varies between 50 μg and 20 mg, and the effects of each of these elements in the body cannot be entirely replaced by any other element [18].

2.1.2.2 Potentially essential trace elements

Potentially essential trace elements are elements whose general impact on the human tissues still lacks some further knowledge, even though they possess some beneficial

characteristics already studied [19]. Among these elements are manganese, silicon, nickel, boron, selenium and vanadium.

2.1.2.3 Toxic trace elements

This class of elements includes cadmium, aluminium, lead and uranium. Their activity in the body is mostly associated with pathologic events, even in small amounts. Cadmium, as an example, has great affinity to biological molecules with the -SH group, replacing other ions and disrupting molecular activity [19, 20].

2.1.3 Biological tissue processing

2.1.3.1 Formalin

Formalin is a chemical compound produced through an aqueous solution of 37-40% formaldehyde, and is one of the most fabricated chemical products on a global scale. This compound is highly important in the crafting process of resins, sanitizers, adherents and other very useful industrial products. Formalin is most commonly made by oxidation of methanol (CH_3OH), which turns into formaldehyde (CH_2O) [21].

Usage of conventional formalin is not suited for biological tissue fixation due to the presence of high concentrations of formaldehyde, which can lead to dehydration, stiffening and decoloration of the tissues. As an alternative to this kind of formalin, a diluted variant of this compound is utilized. This variant is 10% buffered formalin, which is the same as an aqueous solution of 3.7-4.0% formaldehyde [9, 22]. Formalin buffering is usually done by adding pH altering compounds to the aqueous solution of formaldehyde, such as sodium phosphate or calcium carbonate [23]. With this in mind, observable changes in soft tissue elementary content will certainly be correlated to the chemical composition of the buffering compounds, since the interactions between the tissue samples and the formalin occur in a closed system.

Formaldehyde has been used for over a century as a human tissue preserving and embalming technique. This is due to the fact of it having excellent antiseptic properties, which prevents contamination of the sample by foreign decaying agents. This molecule is also known for reacting with proteins, lipids and nucleic acids [22].

2.1.3.2 Preservation Procedures

Elementary content analysis of biological tissue is a fundamental step in understanding the pathogenesis of diseases such as cancer. Additionally, it allows the study of elementary alterations as consequence of the interaction between the tissue and the fixation agent to which it is exposed [9]. Currently, there are two traditional methods for processing biological tissue samples: *snap-freezing* and fixation and embedding. Figure 2.2 portrays the procedure associated with each one.

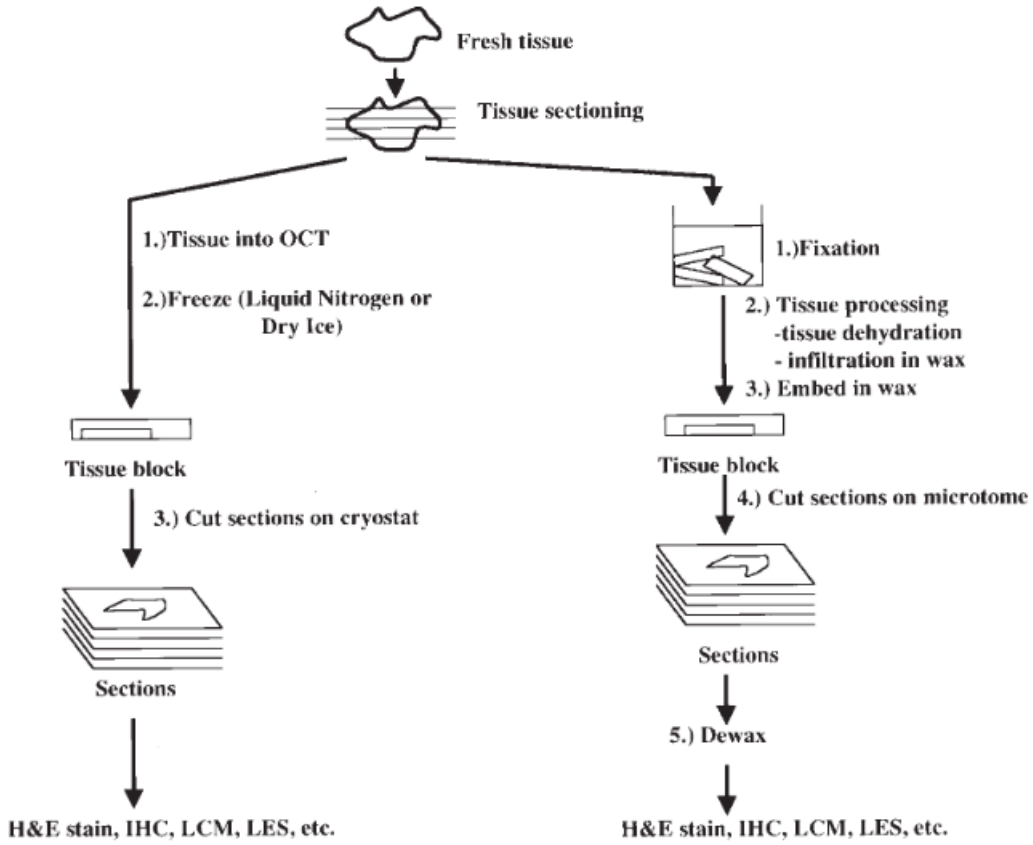

Figure 2.2: Phases of biological tissue processing through *snap-freezing* and fixation and embedding. H&E, IHC, LCM and LES stand for, respectively, hematoxylin & eosin, immunohistochemistry, Laser Capture Microdissection and Layered Expression Scanning, which are some of the processes in which the tissue sections are used [9].

On the one hand, *Snap-freezing* relies on retrieving a fresh tissue sample and placing it in a cryomold, which is then embedded in an optimal cutting temperature (OCT) compound through liquid nitrogen or dry ice. A block is subsequently formed and stored at temperatures ranging from -80ºC to -120ºC [9]. The OCT's main role is to lock the tissue in the block and to cover the entire sample.

This process can be subject to the formation of ice crystals and air bubble entrapment, which might lead, respectively, to the shearing and folding of the tissue during cryosectioning. Hence, it is necessary to be mindful of excessive water quantities when the sample is frozen [24].

On the other hand, when a tissue ceases to have a supplying bloodstream, cellular apoptosis begins to occur, which breaks the homeostasis mechanisms and modifies water and electrolyte dynamics within the cell, as well as its enzymatic activity. This chain of events is propitious to bacterial and fungal growth, resulting in the destruction of the tissue [25].

As such, a fixation agent is needed to avoid the decaying of the tissue not only by the activity of micro organisms but also by the activity of proteolytic enzymes whose

function is to digest and damage the tissue if not inhibited. The most common fixative is the 10% buffered formalin, even though other fixatives can be utilized depending on the circumstances, such as aldehydes, alcohols, oxidation agents or others. Tissue fixation is subject to several factors. Among those there is penetration, volume and concentration of the fixation agents, as well as the volume and type of tissue, its fixation time and the temperature it is fixated at. [9, 24, 25].

After the tissue is fixated, it must be correctly processed, to allow the cutting of sections for analysis. Initially, all tissues are dehydrated for water removal and are thereafter washed and placed in a miscible solution with liquid paraffin [24].

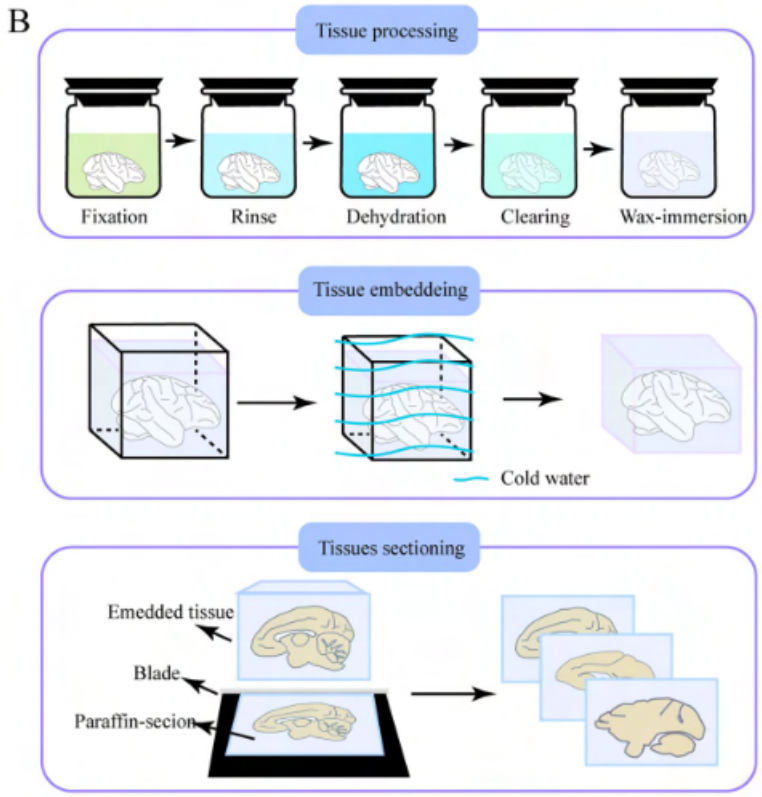

Figure 2.3: Schematic diagram of fixation and embedding for organs. Adapted from [26].

Paraffin is a wax made of long chains of hydrocarbons, and it derives from petroleum. This compound is the embedding agent most frequently used in histology laboratories, since it's compatible with the procedures and protocols of immunohistochemistry.

Paraffin specificities can be adjusted according to its fusion point and the respective tissue. The fusion temperature for paraffin is usually between 56ºC and 57ºC. These values are best suited for generic embedding of tissues. This fusion point makes the paraffin rigid enough at room temperature to obtain sections within the μm range [25, 27]. A schematization of the above process is observable in figure 2.3.

2.2 Physics Concepts

This section aims to elaborate on the most important physics concepts that lay the foundation for the work developed, mainly those concerning how charged particles and photons interact with the samples and the respective detectors.

2.2.1 Protons and Interaction with Matter

There are four possible interaction mechanisms of protons with atoms: coulombic interactions with electrons, elastic interactions with atomic nuclei, nuclear reactions and Bremsstrahlung. Figure 2.4 displays how these mechanisms work, except for Bremsstrahlung which is a rare and, most of the times, negligible interaction and the least likely to occur. Bremsstrahlung is only relevant for proton energies in the GeV range, and these energies are much higher than the ones used in the scope of this work [28–30].

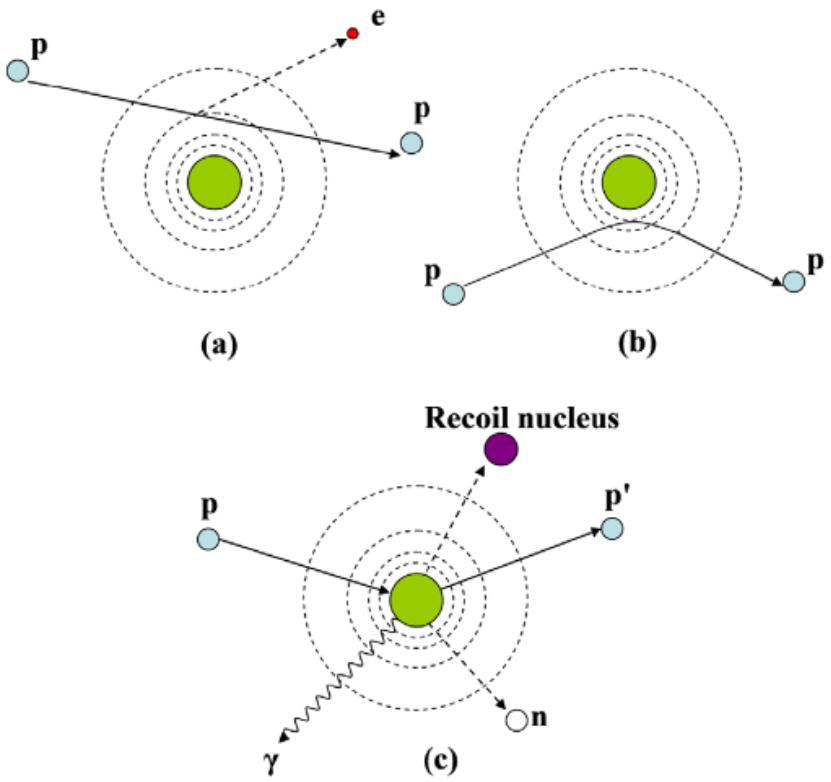

Figure 2.4: a) Coulombic interaction with electrons; b) Elastic scattering with the nucleus, deflecting the primary particle; c) Non-elastic nuclear interaction originating secondary particles like gamma-rays (γ), neutrons (n) or secondary protons (p'). Retrieved from [28].

Inelastic collisions with atomic electrons represent one of the main forms of continuous kinetic energy loss, since these interactions are the most frequent. However, because

the resting mass of the protons is 1832 timer higher than the resting mass of the electrons, there will be almost no deflection of the primary particles and the protons will have essentially a straight-line trajectory. At the same time, protons interact elastically or non-elastically with atomic nuclei. In the elastic interaction, the particles remain unchanged. This interaction can only be Coulombian (Rutherford scattering) but, if the proton enters the nucleus, elastic scattering governed by a nuclear potential also enters into play. Atomic nuclei have comparable or higher mass than that of the proton, deflecting it from its original trajectory. In non-elastic nuclear interactions (nuclear reactions), the primary proton may cease to exist as its own, being incorporated into the the nucleus of a given atom. This will destabilize the atom and, as a result, it may emit secondary particles like protons or heavier ions, neutrons and γ-rays [28–30].

2.2.1.1 Energy and range

All of the above mechanisms involve some form of energy loss. The rate at which a charged particle beam loses energy (dE) as it passes through a thickness dx of the absorbing target is called linear stopping power, and is given as the quotient between dE and dx (equation 2.1). Linear stopping power is more commonly written as mass stopping power as a way to incorporate the absorbing material's density in the equation, making it more convenient for general usage (equation 2.2).

$$S = -\frac{dE}{dx} \tag{2.1}$$

$$\frac{S}{\rho} = -\frac{dE}{\rho \cdot dx} \tag{2.2}$$

Equation 2.2 can also be rewritten in order to fit relativistic theory and quantum mechanical effects. Equation 2.3 was developed by Bethe and Block and is written as

$$\frac{S}{\rho} = -\frac{dE}{\rho \cdot dx} = 4\pi N_A r_e^2 m_e c^2 \frac{Z}{A}\frac{z^2}{\beta^2}\left[ln\frac{2m_e c^2\gamma^2\beta^2}{I} - \beta^2 - \frac{\delta}{2} - \frac{C}{Z}\right] \tag{2.3}$$

where N_A is Avogadro's number, r_e is the classical electron radius, m_e is the electron mass, z is the projectile charge, Z is the atomic number of the target material, A is the atomic weight of that same material, c is the speed of light, $\beta = v/c$ where v is the projectile velocity, $\gamma = (1-\beta^2)^{-\frac{1}{2}}$, I is the mean excitation potential of the material, δ is the density corrections from shielding of remote electrons by close electrons and C is the shell correction item [28].

It is observable in equation 2.3 that the energy loss rate is proportional to the inverse of the velocity squared (both classically, through $1/v^2$, and relativistically, through $1/\beta^2$) and the charge of the ion squared (which is 1 for protons). At the same time, the energy loss rate is also highly dependant on the characteristics of the absorbing material: the higher the mass density of the material, the higher the linear stopping power [28, 29, 31]. Figure 2.5 illustrates the behaviour of a proton beam in water. For energies ranging from 0

to 0.1 MeV, the mass stopping power steadily increases until it peaks. For energies higher than 0.1 MeV, the mass stopping power rapidly decreases. The CSDA range, which stands for continuous slowing down approximation range, is also represented in the figure and shows the average distance travelled by a proton in water.

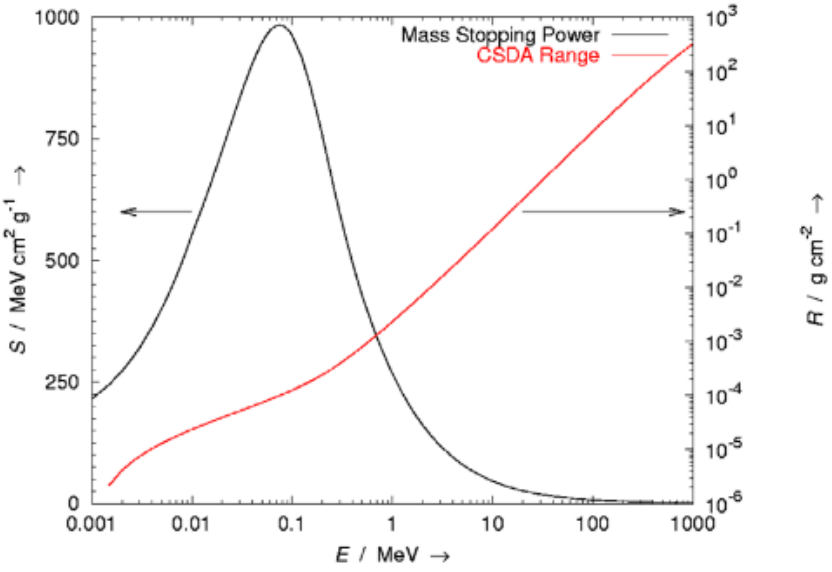

Figure 2.5: Plot of Mass Stopping Power and CSDA for protons in water. Retrieved from [28].

As the protons lose energy across the absorbing material, they will travel in depth. The definition of range is the depth at which 50% of the protons lost all their kinetic energy. The concept of range can only be applied to an ion beam and not single particles, due to energy straggling. Figure 2.6 portrays how the fluence of a proton beam evolves as it traverses the target material. The initial loss of fluence is triggered by the removal of protons by nuclear reactions whereas the rapid fluence decrease is consequence of ions running out of energy and being stopped by the medium [28, 30].

Range can be calculated assuming the particles travel in a straight line (by ignoring lateral scattering) and lose energy continuously. With this assumption in mind, the equation can be written as

$$R(E) = \int_{E}^{0} \left(\frac{dE'}{dx}\right)^{-1} dE' \approx \sum \left(\frac{dE'}{dx}\right)^{-1} \Delta E' \tag{2.4}$$

where E is the initial kinetic energy of the ions [28, 30, 32].

2.2.1.2 Nuclear Reactions

Nuclear reactions are the main source of proton depletion within the beam range inside a given material. In order to achieve a non-elastic nuclear interaction, protons

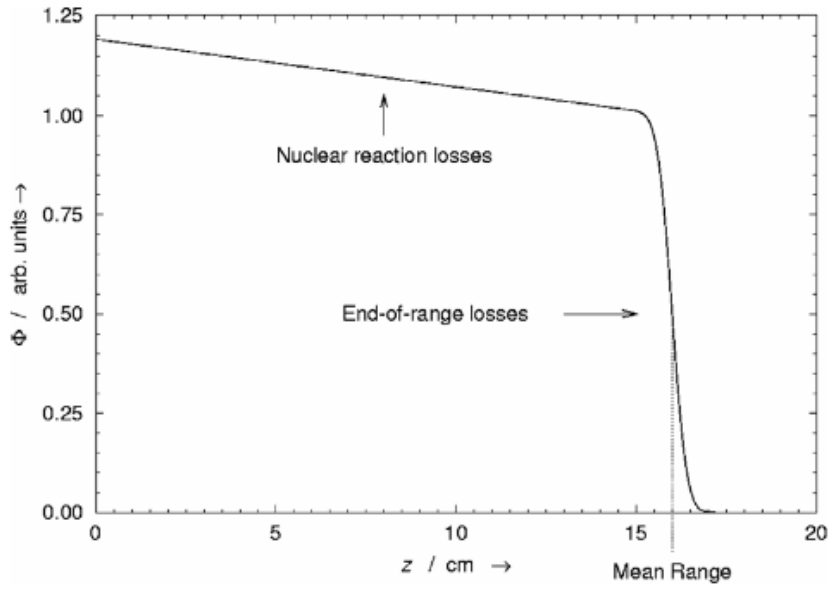

Figure 2.6: Plot of proton beam fluence as a function of its depth in water. Retrieved from [28].

tend to have enough energy to penetrate the Coulomb barrier even though, in some cases, interaction in also possible with energies under this threshold by quantum tunneling. The probability of nuclear reactions by quantum tunneling, excluding coulombian scattering, decays exponentially the lower the energy is below the Coulomb barrier. Figure 2.7 shows how the non-elastic cross section for nuclear reactions in an oxygen medium evolves with the beam energy: proton energies under the threshold value of 6 MeV are commonly unable to penetrate the Coulomb barrier. In rare occasions, particles with less energy than that of the threshold value can still penetrate the Coulomb barrier through quantum tunneling. For biologically relevant atomic nuclei, the energy threshold to overcome the Coulomb barrier rises to about 8 MeV.

In terms of kinematics, one can represent a nuclear reaction with the following notation (equation (2.5))

$$a + A \longrightarrow b + B \tag{2.5}$$

or even a more simplified one (equation (2.6))

$$A(a,b)B \tag{2.6}$$

Normally, a and b are light nuclei, A is a resting heavy nucleus and B is another heavy nucleus. Since b is emitted at an angle θ and B has short range, the conservation of momentum and energy will be as follows (equation (2.7)):

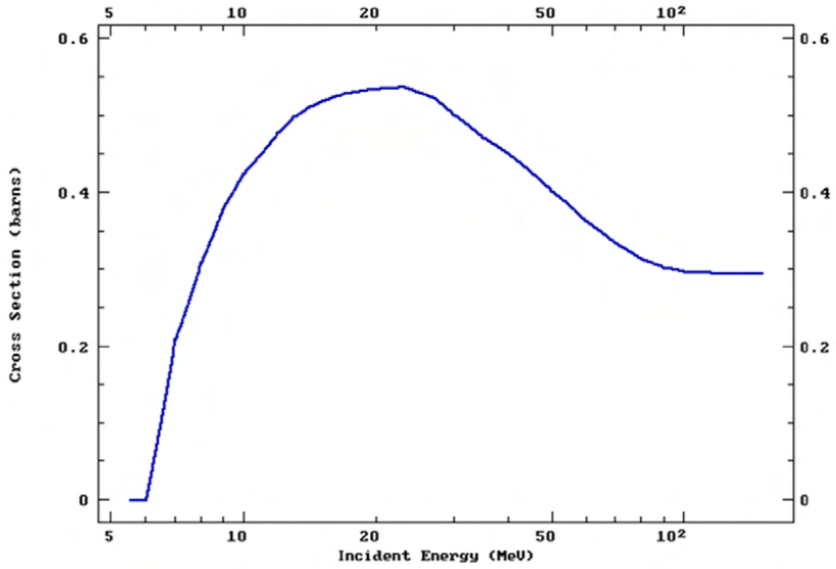

Figure 2.7: Proton-induced nuclear reaction cross section in oxygen, as a function of beam energy. Retrieved from [28].

$$E_a{+}Q = E_b{+}E_B \Longleftrightarrow \sqrt{2m_aE_a} = \sqrt{2m_bE_b}cos\theta{+}\sqrt{2m_bE_b}cos\phi \Longleftrightarrow \sqrt{2m_bE_b}sin\theta = \sqrt{2m_BE_B}sin\phi \tag{2.7}$$

where E_a is the initial projectile energy, E_b is the energy of the emitted secondary particle, E_B is the energy of the target nuclei after the reaction has occurred, ϕ is the scattering angle of heavy nucleus B, Q is the energy balance resulting from the nuclear interaction due to the differences between the initial and the final system mass. Therefore, Q can be written as (2.8)

$$Q = (m_a + m_A - m_b - m_B)^2 \tag{2.8}$$

By merging equations (2.8) and (2.7), Q can be rewritten according to collision parameters such that

$$Q = E_b\left(1 + \frac{m_b}{m_B}\right) - E_a\left(1 - \frac{m_a}{m_B}\right) - \frac{2}{m_B}\sqrt{m_am_bE_aE_b}cos\theta \tag{2.9}$$

The value of Q will dictate whether a nuclear reaction is physically possible. If $Q > 0$, the nuclear reaction will be classified as exothermic, and will occur for any initial projectile energy, If $Q < 0$, the nuclear reaction is endothermic and there is a threshold beam energy that must be fulfilled in order to achieve the reaction. The value of that threshold energy is given by

$$E_t = \frac{-Qm_B(m_B + m_b)}{m_am_bcos^2\theta + (m_B + m_b)(m_B - m_a)} \tag{2.10}$$

The smallest possible threshold energy value for equation (2.10) is when $cos\theta$ equals 1. At this stage, $Q = 0$ and secondary particles, represented above as b, can only be emitted for $\theta = 0$. If E_a becomes greater than E_t, other values of θ become accessible [28, 31, 33].

2.2.2 EBS - *Elastic Backscattering Spectrometry*

Elastic Backscattering Spectrometry (EBS) is a nuclear technique very useful for analysis of surface layers of solid samples. This method consists on bombarding a target with energetic ions (in the 0.5-4 MeV range, typically) and registering their energy as they are backscattered from the target, resorting to energy sensitive detectors. EBS allows the quantitative measurement of materials' elementary matrices and their stoichiometry and is also extremely important for depth profiling of individual elements. This technique has no need for standard samples, has a good resolution depthwise and has great sensitivity for heavy elements. However, this method has low sensitivity for lighter elements, and must be complemented with other nuclear based techniques. EBS is a method that incorporates all types of elastic ion backscattering, with protons and alpha particles being the most common projectiles. Typical backscattering angles are within the 150º-170º range [34, 35].

The geometry of particle movement and particle scattering can be represented by figure 2.8. This geometry serves as base for the kinematic study behind EBS [35].

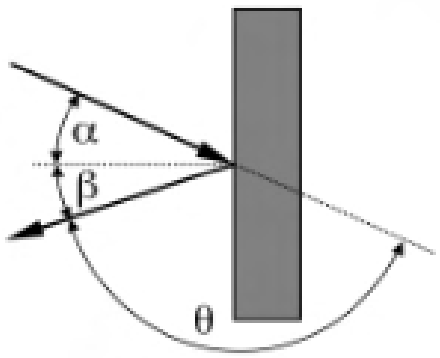

Figure 2.8: Scattering geometry for an incident particle beam. α is the incident angle, β is the exit angle and θ is the scattering angle. Retrieved from [35].

In terms of kinematics, the incident particle energy can be related to the scattered particle energy through the use of the kinematic factor K (2.11)

$$\frac{E_1}{E_0} = K \tag{2.11}$$

where E_0 and E_1 represent the incident and the scattered particle energy, respectively.

The kinematic factor is a specific parameter for the interaction between a particle and an atomic nucleus. It is solely dependant on the mass of the projectile, the mass of the target nucleus and the scattering angle, and can be written as (2.12)

$$K = \frac{M_1^2}{(M_1 + M_2)^2}\left[cos\theta \pm \sqrt{\left[\left(\frac{M_2}{M_1}\right)^2 - sin^2\theta\right]}\right]^2 \tag{2.12}$$

where M_1 is the mass of the incident particle, M_2 is the mass of the target nucleus and θ is the scattering angle in the laboratory system. By having, typically, a solid state energy detector at a known angle and knowing the mass, the primary energy and the scattered energy of the projectile, equation (2.12) can be solved for M_2, identifying the target nucleus. On a special note, the $\pm$ operator in equation (2.12) only applies if $M_1 > M_2$. Otherwise, only the plus sign is taken into consideration when solving for a solution [34, 35]. Kinematic factor as a function of M_2 at a 165º scattering angle, for three different projectiles (^{1}H, ^{4}He, ^{7}Li) is displayed in figure 2.9.

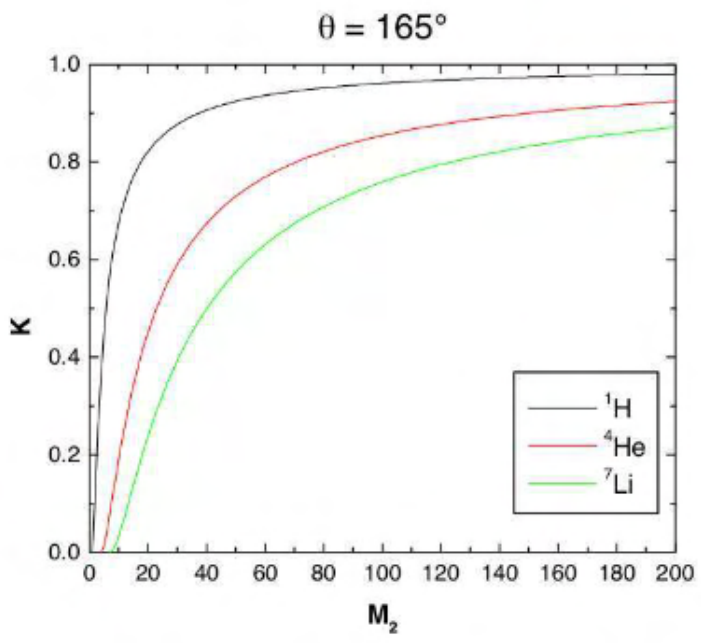

Figure 2.9: Kinematic factor K as a function of target nucleus mass, M_2, for a 165º scattering angle. Each different projectile has a different K curve. Retrieved from [35].

Not all particles that come in contact with the absorbing target are backscattered. The Rutherford cross-section for backscattering translates into the probability of this type of coulombian interaction, as a function of the scattered angle and the initial beam energy. The equation below represents the Rutherford differential cross-section for coulombian interactions (equation (2.13)),

$$\sigma_R(E,\theta)[mb/sr] = 5.1837436 \times 10^6 \left(\frac{Z_1 Z_2}{E}\right)^2 \frac{\left[\sqrt{M_2^2 - M_1^2 sin^2\theta} + M_2 cos\theta\right]^2}{M_2 sin^4\theta \sqrt{M_2^2 - M_1^2 sin^2\theta}} \tag{2.13}$$

where Z_1 and M_1 are the atomic number and the mass of the projectile, respectively, Z_2 and M_2 are the atomic number and the mass of the target atom, respectively, E is the beam energy in keV and θ is the scattering angle. For Rutherford backscattering spectrometry (RBS), only the cross-section above is considered. For EBS, the nuclear potential interactions also come into play.

Nonetheless, for high and low energies, cross-section values start to deviate from those calculated resorting to equation (2.13), and correction factors need to be taken into consideration for these cases. For $\theta > 90^o$, the correction factor by L'Ecuyer is most commonly used, even though corrections tend to be fairly small for this angle range. For small scattering angles, the correction factor of Andersen *et al.* is the most appropriate. Figure 2.10 shows each type of correction according to the respective scattering angle [34, 35]

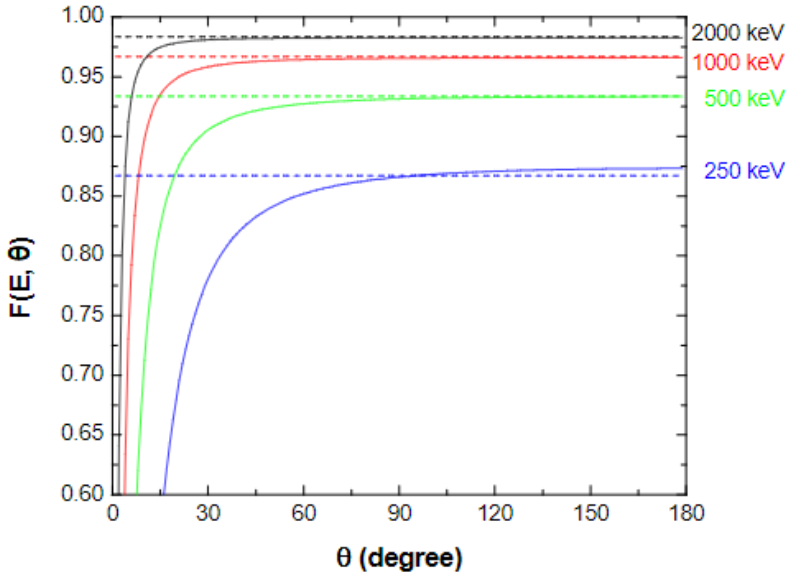

Figure 2.10: L'Ecuyer (dashed lines) and Andersen (solid lines) corrections for varying scattering angles. Retrieved from [35].

An example of a EBS spectrum is shown below, in figure 2.11. It shows a cobalt and niobium sample with multiple intertwined layers. The further away the layer is from the initial contact point with the beam, the less energetic the peak for the corresponding element.

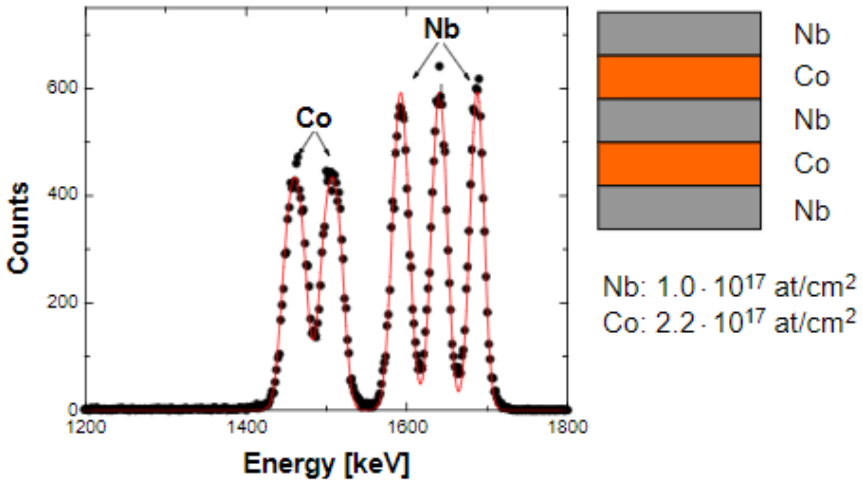

Figure 2.11: EBS spectrum taken with 2MeV alpha particles at a 165º scattering angle. Dots are the experimental data and the solid line is a computer simulation through SIMNRA software. Retrieved from [35].

2.2.3 Gamma-rays and Interaction with Matter

These particles have the shortest wavelength in the entire electromagnetic spectrum: around 10^{-12} m, which is about the size of atomic nuclei [36].

γ-rays originate from the atomic nucleus, and are emitted as a byproduct of radioactive decay and nuclear reactions [37].

2.2.3.1 Energy and attenuation

Unlike charged particles, the concept of energy loss and range is not applicable to photons. Instead, a photon beam loses intensity throughout the material, which means less photons reach higher depths.
For this specific case, kinetic energy is given by (2.14)

$$E = h\nu = h\frac{c}{\lambda} \tag{2.14}$$

where h is Planck's constant, ν is the wave frequency of the photon, c is the speed of light and λ is the wavelength of the photon.

As a photon beam traverses a certain medium, photons start to decline in number due to exponential attenuation as they are scattered or absorbed. Let I_0 be the photon beam's initial intensity and σ_{tot} the total cross section for scattering and absorption. As a photon beam passes through a thickness equal to dx, a number of photons represented by $-dI$ is removed per unit of time. $-dI$ is proportional to the beam intensity, I, at depth x, and to the number of atoms per volume unit, n_A (2.15).

$$-dI = I n_A \sigma_{tot} dx \tag{2.15}$$

By solving the differential equation above, integrating between I_0 and I, the equation of exponential attenuation for photons is given by (2.16)

$$I = I_0 e^{-\mu_{att,l} x} \tag{2.16}$$

where $\mu_{att,l}$ is the linear attenuation coefficient, given by (2.17).

$$\mu_{att,l} = n_A \sigma_{tot} \tag{2.17}$$

This linear attenuation coefficient can be converted into the mass attenuation coefficient ($\mu_{att,m}$) by dividing (2.17) by the absorber density. If that absorber is a compound, $\mu_{att,m}$ can be calculated through the mass attenuation coefficient of every individual element in the compound (2.18)

$$\mu_{att,m} = \sum_i w_i \mu_{att,m,i} \tag{2.18}$$

where w_i is is the mass fraction of the ith element in the compound.

The total cross section of photons' interaction with matter is mostly dependant on 4 processes: photoelectric effect (PE), Compton scattering (CS), pair production (PP) and Rayleigh scattering [36–38]. The first 3 are the most dominant and will be further explored below.

2.2.3.2 Photoelectric effect

PE is a physical mechanism that is most common at low energies, depending on the absorbing material. It occurs when a photon interacts with an atomic bound electron and its energy is greater than the electron's binding energy. The photon is then absorbed in the process and the electron is detached from the atom [36–38]. Figure 2.12 illustrates this interaction.

The energy balance of the PE is given by equation (2.19)

$$E_\gamma = E_e + E_a + E_B \tag{2.19}$$

where E_γ is the energy of the incident photon, E_e is the energy of the ejected electron, E_a is the recoil energy of the atom as a whole and E_B is the binding energy of the electron in the atom. The recoil kinetic energy of the atom is directly proportional to the kinetic energy of the electron and to the quotient between the mass of the electron and the mass of the atom. Since the mass of the atom is, approximately, 10000 times greater than that of the electron, the recoil energy is negligible. Hence, equation (2.19) can be simply rewritten as equation (2.20) [36–38].

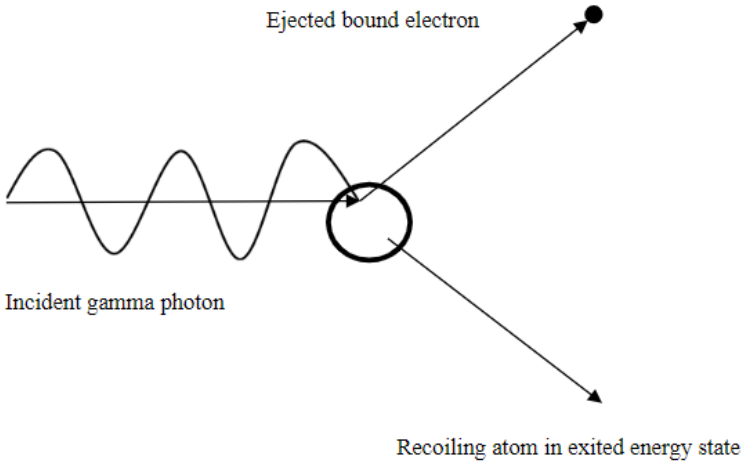

Figure 2.12: Photoelectric effect. Retrieved from [37].

$$E_e = E_\gamma - E_B \tag{2.20}$$

The photoelectric absorption cross section is proportional to the atomic number Z of the absorbing element and is inversely proportional to the energy of the incident photon, according to equation (2.21)

$$\sigma_{photoelectric} = \frac{CZ^n}{(h\nu)^m} \tag{2.21}$$

where m and n are values ranging from 1 to 3 and from 4 to 5, respectively. This implies that for elements with higher atomic number and for lower photon energies, the probability of photoelectric effect occurring increases, as long as the photon's energy is greater than the electron's binding energy [37].

2.2.3.3 Compton scattering

CS is a process in which the incident photon interacts with a free electron or a very weakly bound electron, such that $E_\gamma \gg E_B$, according to the notation above. With this in mind, the electron binding energy should be negligible. The photon is scattered at an angle θ with the photon's initial trajectory and the free electron gains kinetic energy and is scattered at an angle ϕ with the photon's initial trajectory. CS is represented in figure 2.13.

The energy balance for this interaction obeys the following relativistic equation (2.22)

$$E_\gamma + E_e = E_{\gamma'} + \sqrt{E_e^2 + c^2 p^2} \tag{2.22}$$

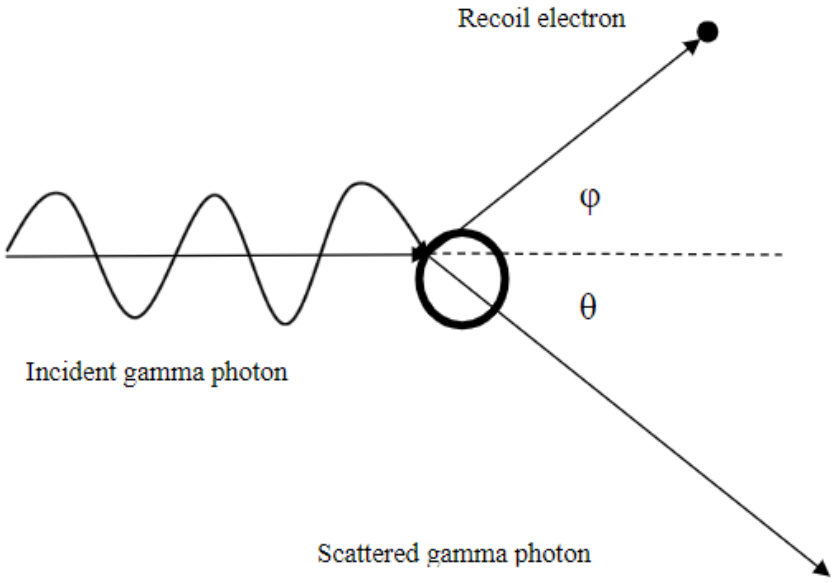

Figure 2.13: Compton scattering. Retrieved from [37].

where E_γ is the energy of the incident photon, E_e is the energy of the electron at rest ($m_e c^2$ = 511 keV), E'_γ is the energy of the scattered photon, c is the speed of light and p is the linear electron momentum after the interaction.

Conservation of momentum along the photon's initial trajectory is verified (2.23)

$$\frac{E_\gamma}{c} = \frac{E_{\gamma'}}{c} cos\theta + pcos\phi \tag{2.23}$$

as well as along the perpendicular direction to the photon's initial path (2.24)

$$0 = -\frac{E_{\gamma'}}{c} sin\theta + psin\phi \tag{2.24}$$

By isolating and squaring the ϕ terms in both equations, we can eliminate them through the trigonometric relationship $\cos^2\phi + \sin^2\phi = 1$. Therefore, we get equation (2.25)

$$p^2c^2 = E_\gamma^2 - 2E_\gamma E_{\gamma'} cos\theta + E_{\gamma'}^2 \tag{2.25}$$

This last equation can be merged with equation (2.22) to yield an expression that correlates the energy of the scattered photon to the initial photon energy, the scattering angle θ and the rest energy of the electron (2.26).

$$\frac{1}{E_{\gamma'}} - \frac{1}{E_\gamma} = \frac{1 - cos\theta}{E_e} \tag{2.26}$$

Since photons are particles with no charge, CS is barely influenced by the atomic nucleus, causing the atomic number to be irrelevant for cross section calculations. Its

cross section value depends on the electronic density, which is mostly constant for all elements and proportional to the ratio between the atomic number and the mass number, Z/A, and depends on the primary photon energy. As the photon energy increases, the total Compton cross section decreases [36–38].

2.2.3.4 Pair production

When a photon with kinetic energy equal or superior to twice the electron's rest energy ($2m_ec^2 = 1.022$ MeV) comes close to a significantly sized charged object, like an atomic nucleus, the emergence of an electron and a positron as a consequence of that interaction becomes possible. If the photon exceeds 1.022 MeV, the extra energy will be equally distributed among the electron and the positron as kinetic energy. This process is represented in figure 2.14.

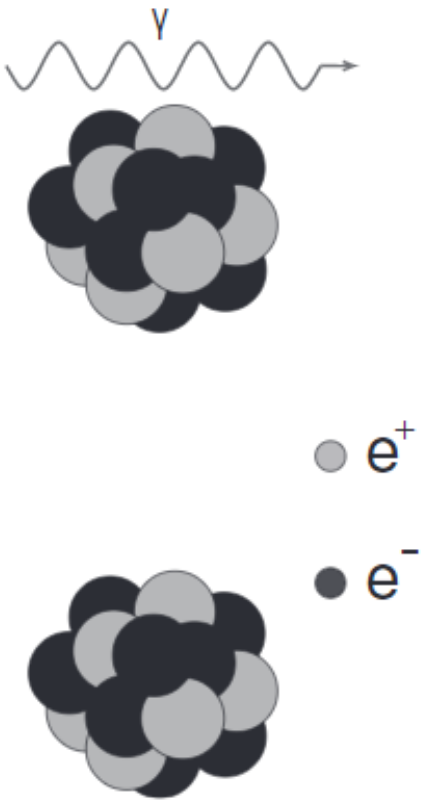

Figure 2.14: Pair production. Adapted from [38].

PP can only occur in the vicinity of a nucleus, as the small recoil energy it gains from the interaction is the only way to conserve momentum. The positron originating from this process is rapidly annihilated with a nearby electron, emitting two 511 keV γ-rays if the positron is annihilated at rest. These γ-rays might escape or further interact with the medium.

This interaction mechanism does not solely depend on the photon energy, but also on the nucleus whose Coulomb field the photon passes through. For that reason, the energy of the photon must take into consideration the recoil energy of the nucleus in the interaction. Equation (2.27) takes this energy correction into account.

$$E_{\gamma,min} = 2m_e c^2 \left(1 + \frac{m_e}{M}\right) \tag{2.27}$$

$E_{\gamma,min}$ is the threshold photon energy, m_e is the mass of the electron, c is the speed of light and M is the mass of the charged particle whose Coulomb field the photon is passing through. For heavy nuclei, the photon energy increase beyond 1.022 MeV is insignificant, as $\frac{m_e}{M}$ approaches 0. For PP to occur, for example, with electrons as the nearby charged particles, the photon must have 2.044 MeV, since M becomes m_e in equation (2.27) [36–38].

2.2.4 PIGE - *Particle Induced Gamma-ray Emission*

The PIGE technique is based on the detection of γ rays originating from the nuclear reactions occuring between the particles of the beam and the target atoms. This technique complements the Particle Induced X-ray Emission (PIXE) technique, which allows for analysis and quantification of elements whose atomic number is higher than or equal to 14. Lighter elements cannot be detected by PIXE, since the x-rays originating from these reactions have energies below 2 keV, which is a value very close to the minimum energy limit to which the detector is sensitive, thereby not triggering photoelectric effect on the detector.

Therefore, and since for the same beam energy γ radiation tends to be more energetic than X-radiation, due to interactions with the atoms' nuclei, it is possible to bypass the problem of detecting characteristic photons for elements with $Z \leq 14$ [34].

2.2.5 Gamma radiation spectra

The gamma radiation spectrum is a continuous spectrum containing energy peaks corresponding to emitted photons as a consequence of nuclear reactions. Background present in these spectra is essentially because of CS of high energy γ radiation. An example of a gamma specter is shown in figure 2.15.

The figure above clearly emphasizes the gamma emissions resulting from nuclear reactions between the beam and the represented elements in the sample. These reactions are predominantly (p, p'γ), although they can also be (p, $\alpha\gamma$) or (p, γ) [19, 39].

2.2.6 Determination of elementary concentrations

For thin films, the nuclear reaction cross-sections can be considered constant due to negligible losses of ion beam energy across the film. The yield of a given reaction, measured at an angle θ, is proportional to the number of incident particles Q/e, where

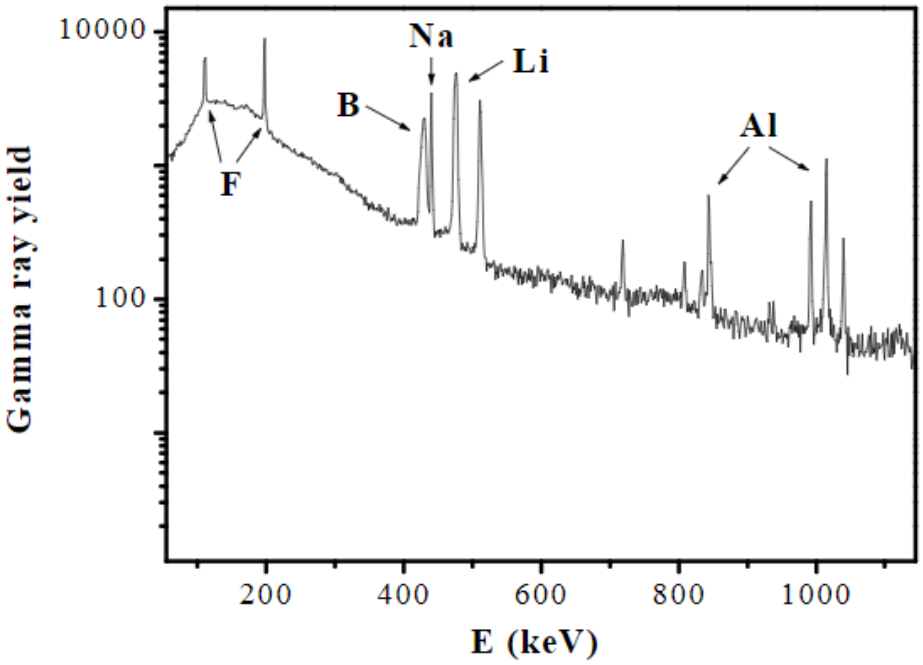

Figure 2.15: Gamma spectrum of a mineral sample containing fluorine, boron, sodium, lithium and aluminium [39].

Q is the collected charge and e is the beam's state of charge, to the number of atomic nuclei of a given isotope per unit area, N_{iA}, to the differential cross-section of the nuclear reaction, $\sigma(E,\theta)$, and to the absolute efficiency of the detector (equation 2.28).

$$Y(E,\theta) = 4\pi \cdot \epsilon_{abs}(E_\gamma) \cdot \left(\frac{Q}{e}\right) \cdot \sigma(E,\theta) \cdot N_{iA} = 4\pi \cdot \epsilon_{abs}(E_\gamma) \cdot \left(\frac{Q}{e}\right) \cdot \sigma(E,\theta) \cdot N_i \cdot \Delta x \qquad (2.28)$$

N_i and Δx are a conversion of N_{iA} into a product between the number of atomic nuclei per unit volume and the target sample's linear thickness.

If the target is not thin, one must consider the material's stopping power, which attenuates the beam's energy as it is passing through the target. Equation 2.28 can still be used, as long as there is a sectioning of the target into multiple thin layers of linear thickness, dx, or mass thickness, $d\Gamma$ (equivalent to $dx \cdot \rho$, where ρ is the mass density of the material). Figure 2.16 demonstrates the process of energy loss throughout a thick target.

These considerations can be put together to make the reaction yield differential equation, where f_m represents the mass fraction of a given element, f_i represents its isotopic abundance, N_{av} is *Avogadro´s* number and A is that element's atomic mass.

$$dY(E,\theta) = 4\pi \cdot \epsilon_{abs}(E_\gamma) \cdot \left(\frac{Q}{e}\right) \cdot \sigma(E,\theta) \cdot f_m \cdot f_i \cdot N_{av} \cdot A^{-1} \cdot d\Gamma \qquad (2.29)$$

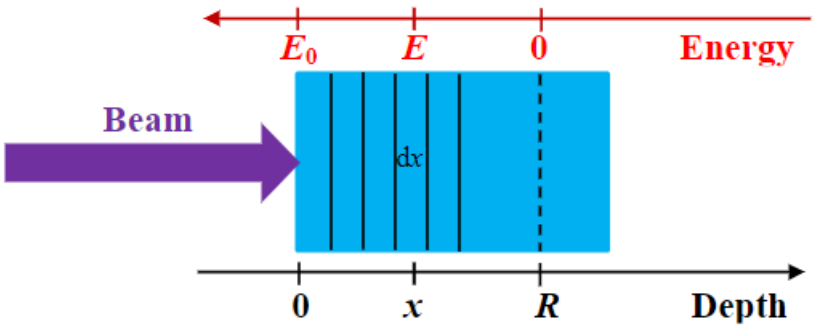

Figure 2.16: Energy loss of a particle beam throughout a thick target [39].

By integrating across the particles' maximum reach, represented by R in figure 2.16, the yield for a thick target is obtained (equation 2.30).

$$Y(E,\theta) = 4\pi \cdot \epsilon_{abs}(E_\gamma) \cdot \left(\frac{Q}{e}\right) \cdot f_m \cdot f_i \cdot N_{av} \cdot A^{-1} \cdot \int_0^R \sigma(\Gamma,\theta) d\Gamma \tag{2.30}$$

Since the beam's maximum reach is a function of its initial energy, E_0, and of the mass stopping power of the material, S_m, given in energy per unit area $\left(\frac{MeV}{g \cdot cm^{-2}}\right)$, the equation above can be rewritten accordingly (equation 2.31).

$$Y(E,\theta) = 4\pi \cdot \epsilon_{abs}(E_\gamma) \cdot \left(\frac{Q}{e}\right) \cdot f_m \cdot f_i \cdot N_{av} \cdot A^{-1} \cdot \int_0^{E_0} \frac{\sigma(E,\theta)}{S_m(E)} dE \tag{2.31}$$

ERYA *software* will use this last equation to calculate the mass concentration of a given element in a homogeneous sample, by resolving the integral through access to well-studied cross-section databases [11, 19, 39].

3

State of the Art

3.1 Effects of formalin fixation in biological tissue element concentration

The usage of formalin as a fixation agent has long been relevant for tissue preservation. With this is mind, some studies went forth and analyzed the impact of FF in the element concentrations of the respective tissue samples.

A report by Bush et al. [40] had already investigated the potential effects of formalin in several organ samples, with its main focus on essential and toxic trace elements. As stated in this paper, there was not a significant concentration change between the fresh and the formalin-fixated tissues for either type of trace element. However, the overall concentration uncertainties are extremely high, which might affect the credibility of these results.

A more recent study by Gellein et al. [41] was conducted in order to study the leaching of trace elements from biological tissue into formalin. An extensive report on several trace elements present in brain tissue was the main driving force of this work. Concentrations of As, Cd, Mg, Rb and Sb in formalin in which the brain tissue samples had been preserved over several years were more than 100 times greater when compared to their concentrations in fresh formalin. The concentration of essential trace elements like Fe, Zn and Cu in the utilized formalin was roughly 20 times higher than that verified for its fresh counterpart. Moreover, a significant decline in Mn tissue concentration and an increase in Al tissue concentration was also registered over a 1-year fixation period. In regards to Cr and Ni, their concentration remained mostly unaltered with FF.

This study concluded that the degree of leaching differs from element to element, and is closely related to the binding properties of the element in the tissue.

A complementary study regarding element distribution in formalin fixed slices of human mesencephalon was also investigated, as a means to understand if changes in element concentrations were accompanied by changes in element distribution with FF, in the various regions of the mesencephalon tissue [42]. The main outcome suggested that the specific distribution patterns of Fe, Pb, Ca and Mn were preserved in the tissue after

more than 10 years of FF.

3.2 Effects of formalin fixation in tumour size

Currently, some studies point to a change of size of biological tissue (specially tumours) when fixated in formalin during significant amounts of time. Most of these alterations came in the form of shrinkage of the biological tissue samples after fixation.

FF has already been studied for different types of tumour tissue. Among these there are head, neck (mostly oral cavity), thyroid and oropharynx tumours, which have been fixated during times ranging from 24h to 48h. Results pointed to an average decrease of length, width and depth of the tumours by 4.40%, 6.18% and 4.10%, respectively [43]. In addition, another study analyzed tumours from non-small-cell lung cancer. After overnight FF, 46.8% of tumours were registered to be, in average, 7.7% smaller, 4.8% increased in size, in average, by 9.2% and the remaining 48.4% did not show any size alterations [44].

Other studies suggest, however, that FF of certain tissues does not contribute at all to changes in their size or that registered changes are not significant.

Two studies brought forth on breast tumour specimens concluded, after fixation within several time frames, that shrinkage of formalin-fixated tumours was similar or equal to the shrinkage of non-fixated tumours [45, 46]. Moreover, prostatectomy specimens were also studied through fixation by formalin injection. After overnight fixation, results corroborate those verified for the breast tumours [47]. Only studies of ocular and tonsil tissue revealed slight decreases after FF. For ocular tissues, several evaluation parameters were taken. The average percentage difference after 24h of fixation was 1%. As for the tonsil tissues, it was stipulated that size variation over different times of fixation was negligible. Hence, the results had no clinical relevance whatsoever [48].

More recently, in the thesis titled "*Influence of paraffin embedding in the human biopsied soft tissue*"of student Alexandre da Veiga [49], tissues from several organs were studied after being fixated in formalin in times ranging from 3 to 24 days. The analyzed elements yielded some interesting results. In average, there was an increase of phosphorus and zinc in the tissue, while sulfur, chlorine, potassium and calcium suffered a decline. The rest of the detectable elements by XRF did not reveal significant changes.

3.3 Trace element analysis in cancer tissue

IBA techniques have long been used for elementary profiling of some biological samples, mostly tumours. Nowadays, there are already multiple cancer tissues being analyzed in this field.

One of the most well-studied pathological tissues regarding its elementary composition is the breast tumour tissue. It has been studied by techniques such as PIXE, Synchrotron Radiation Induced X-ray Emission (SRIXE) and Total Reflection X-ray Fluorescence (TXRF). All of these techniques detected increased levels of trace elements like, bromine, zinc, iron, copper and others [50, 51], probably due to the fact that many of these serve as enzymatic cofactors [52].

Gastrointestinal carcinoma studies (stomach, intestine and colon) also point to changes in elementary content, mostly phosphorus. There is some contradictory information regarding elements like chromium and nickel in stomach carcinomas, as there is no consensus on which tissue (healthy or cancerous) has higher concentrations of these elements. A possible justification to this discrepancy might be related with the different sensitivities of different techniques to these elements, but could also have to do with the fact that chromium and nickel variations do not influence the appearance of tumour tissue [50–52].

Generally, all analyzed cancer tissues presented some sort of fundamental alteration on an elementary level. Potassium is a curious element, since it presents very high values in any given tissue compared to those expected. Even though it is not a trace element, potassium is a minor element and has an incredibly important role in regards to electrolytic balance at a cellular level, as explained in section 2.1.1. In this specific case, concentration of this element can be correlated to the necessity of an increased blood supply to support the swift cancer cell multiplication [52].

3.4 Influence of paraffin embedding on soft tissue analysis

Within the scope of the master's thesis mentioned in section 3.2, the elementary analysis technique X-ray fluorescence was utilized to study certain trace elements in formalin-fixated and paraffin embedded specimens.

Since the preservation process of biological tissue not only includes its fixation, but also its embedding, the work developed in the aforementioned master's thesis was complementary to the work developed throughout this thesis, in that it is necessary not only to parameterise elementary changes caused by paraffin embedding, but also by FF, in order to have more rigorous studies for future histological interventions. In addition, sample analysis by PIGE allows for quantification of lighter elements than those quantified by XRF, assuring a broader vision of the multiple elementary alterations that might occur.

In regards to the specific study of paraffin influence, this endeavor was based on the establishment of correlations between elementary quantities of uniquely formalin-fixated samples and elementary quantities of formalin-fixated and paraffin-embedded samples.

The analysis method for each envisioned element consisted of a linear fit of elementary concentration representative points for a given formalin-fixated and paraffin-embedded tissue, in function of that same concentration for a uniquely formalin-fixated tissue. By

using the reduced χ^2 method, it was possible to establish some conclusions about the role of paraffin embedding in elementary oscillations in biological tissue. In a general manner, the results show that paraffin has a higher influence over lighter elements than heavier elements [49].

4

Materials and Methods

This chapter will expose and explain all the instruments and methods used to achieve the end-goal of this work.

4.1 Data sets

The data sets used for this work were made available by IPO - Instituto Português de Oncologia. These data sets consisted of different tissues, namely colon, stomach, spleen and ileon. Samples from each tissue were stored in formalin for variable periods of time, according to table 4.1

These data sets had been used before for XRF analysis, but lacked further studies regarding their light element composition, hence their inclusion in this work.

These sets included many different tissues and different times in formalin between them, including a fresh sample for each set. This conveys that they were not the most appropriate to conduct a study concerning the progressive description of FF effects, as the samples for each tissue were very limited and it would be unwise to use different tissue samples with different FF times to fill data gaps among them.

Table 4.1: Organ data sets and respective time in formalin.

Set of samples		Time in formalin / days												
		Fresh	2	3	5	6	7	8	9	10	12	14	15	23	24
1	Colon	x				x						x			
3	Stomach														
5	Spleen	x			x			x				x			
7	Colon														
8	Stomach														
9	Colon														
12	Ileon	x	x				x		x		x				x
14	Colon														
15	Colon	x		x	x					x	x				
17	Colon														

Table 4.2: Muscle data sets and respective storage time in formalin.

Set of samples		Time in formalin								
		Fresh	15m	30m	1h	3h	4h30	6h	24h	48h
328	Muscle	x				x				x
329	Muscle	x				x			x	
330	Muscle	x	x		x		x			x
331	Muscle	x	x		x		x		x	x
332	Muscle	x	x	x		x		x	x	
334	Muscle	x	x						x	x

With this in mind, only sample sets #1, #5, #12 and #15 were analyzed and studied resorting to PIGE.

To bridge this gap, additional data sets of muscle tissue were harvested and retrieved in order to achieve a more conclusive study on formalin effects on biological tissue. These new sets and their formalin fixation times are displayed in table 4.2 and their study allows to draw conclusions across data sets. In both tables, unmarked cells represent samples that were either not prepared or unfit to be analyzed in the Tandem accelerator. The cells marked with an x were analyzed recurring to PIGE.

4.2 Tandem accelerator

The Tandem accelerator present at IST-CTN was used for data acquisition throughout this work. This accelerator is an assembly of multiple distinct parts, and each of these parts has many different constituents. The accelerator voltage can go up to 3 MV, depending on the experience at hand [53, 54]. A tandem schematic is shown below, in figure 4.1.

4.2.1 Ion source

The ion source works by having a low pressure arc discharge in the gas, which is constricted by an intermediate electrode placed between a cathode and an anode. The presence of a strong magnetic field between the cathode and the anode allows for a narrow plasma beam to exit the aperture into the accelerator, with currents up to 30 μ A. For this specific work, H^- was the ion extracted from the hydrogen bottle. The ion source is mediated by several power supplies and meters, such as the filament, the magnet control, the gas control, the arc voltage, the extraction and the high voltage power supply [55].

4.2.2 Beam transportation system

The transportation system is divided in two parts: the low-energy stage and the high-energy stage, based on the particle energy in each of them. The entirety of the system is made of three switching magnets (one in the low-energy stage and two in the high-energy stage), electrostatic quadrupoles, triplets and doublets, Faraday cups for current

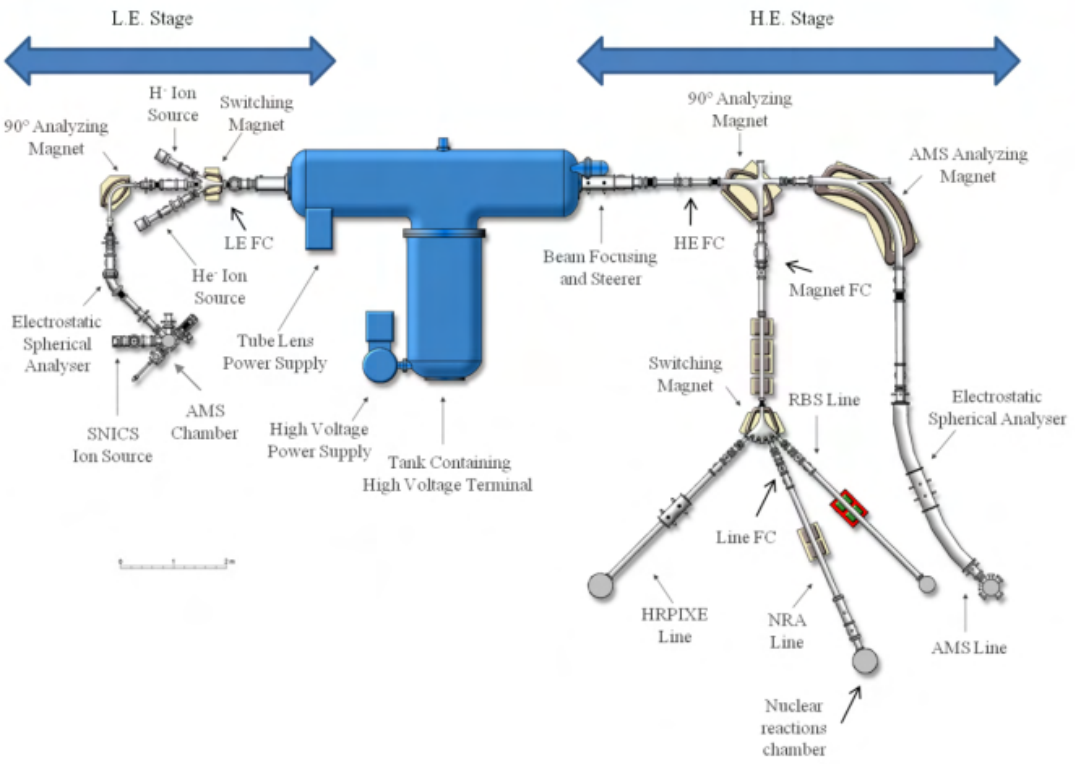

Figure 4.1: Tandem schematic. FC stands for Faraday cup, LE and HE stand for low-energy and high-energy, respectively, and NRA stands for Nuclear Reaction Analysis. Retrieved from [53]

measurements and collimators. The low-energy stage comes before the acceleration stage, while the high-energy stage comes after the acceleration stage [54, 55].

4.2.2.1 Low-energy stage

At this point, beam energy tends to be around 15 keV, and is given by equation (4.1)

$$E = eV_i \tag{4.1}$$

where e is the total charge of the ion and V_i is the extraction voltage. The switching magnet at the low-energy stage will filter out the ions that enter the accelerator according to their mass to charge ratio (m/q). The first Faraday cup allows for current maximization in this particular stage, by optimizing the ion source parameters and the switching magnet current [55].

4.2.2.2 High-energy stage

The high-energy portion of the transportation system contains a set of deflector plates and a set of focusing electrostatic quadrupoles. Preceding the high-energy Faraday cup,

there is a set of 4 slits that is utilized to alter the beam diameter. The components in the low-energy side, namely the matching lenses, the tube lenses and the deflector plates, are also used for beam optimization in the high-energy side. The high-energy Faraday cup is followed by a 90º analysing magnet that makes another m/q selection, which is measured in the following Faraday cup, named magnet Faraday cup. After this cup, a set of magnetic quadrupole triplets is used to focus the beam onto another switching magnet, which in turn deflects the beam to the nuclear reactions line. There, a tantalum collimator is used to choose the size of the beam, and is followed by a final Faraday cup that yields the final beam current entering the nuclear reactions chamber (see figure 4.1) [55].

4.2.3 3 MV Pressurized Tank

The Tandem is an electrostatic accelerator in which the accelerator tank is filled with high pressure SF_6 gas and incorporates a Crockroft-Walton generator of 3 MV, made by a network of capacitors and diodes to allow the generation of high voltages. The high voltage terminal creates a positive potential at the center of the accelerator, that accelerates the negatively charged ions coming from the low-energy side until they reach the center point, where the beam is stripped and further accelerated to higher energies. The stripping process consists of removing the outer electrons from the ions, changing their charge state from negative to positive, by resorting to a gas that interacts with the ions as they pass through it.

After becoming positively charged, the ions are repelled towards the high-energy side by the same positive potential, with energy according to the following equation (4.2)

$$E_f = E_i + (q+1)eV \tag{4.2}$$

where E_f is the final ion energy, q is the charge state of the particles after the stripping and V is the terminal voltage of the accelerator. For protons, E_f will be approximately twice the terminal voltage.

4.2.4 Nuclear Reaction Chamber

The Nuclear Reaction Chamber itself is a Faraday cup, electrically insulated from the rest of the beam transportation system. It is comprised of a collimating system, a movable target holder with respect to the beam axis and a beam stopper. Additionally, there are 3 detectors in the chamber: 2 particle detectors (MOVE and MOVD) and a γ-ray detector. This chamber must be placed under high vacuum to ensure the least possible interactions between the beam and air particles.

4.2.5 Detectors

4.2.5.1 Silicon detectors

Particle detectors used in the Nuclear Reaction Chamber are Passivated Implanted Planar Silicon detectors, or PIPS, with 50 mm^2 active area and a 100 μm depletion layer. Ionization by charged particles causes electron-hole pairs to form in the detector. As the energy of the incident charged particle increases, more pairs start to form, yielding a more intense signal [55, 56].

4.2.5.2 High Purity Germanium detector (HPGe)

For γ-rays, a HPGe detector is used. The crystal diameter is 64 mm with a length of 62.6 mm. It works the same as the silicon detectors, by creating electron-hole pairs. Instead of ionization by charged particles, the dominant interaction mechanisms are photoelectric effect and Compton scattering. The resulting electron cascade will be converted into a measurable signal [55, 57].

4.3 Sample Treatment

All the analyzed samples from the first data set had already been turned to pellets, since they were used in previous works [49], and were stored in a fridge for posterior usage.

The samples from the second data set were firstly lyophilized in FCT-UNL, in order to remove all water content from the sample, and turned to small portions of dry tissue. Each portion of dry tissue was grounded into a fine homogeneous powder, resorting to a pestle and mortar, as seen in figure 4.2.

The powders were stored in plastic containers and Petri dishes and brought to CTN-IST, where they were pressed into pellets, resorting to a pellet maker and a presser (figure 4.3). In order to achieve consistent pellets, and since the powder yield was small, a pressing mass of 10 tons was used. Compression lasted 1 to 2 minutes, depending on the powder yield.

The pellets were then kept in Mylar sheets and placed in a sample holder, as displayed in figure 4.4.

4.4 Data acquisition

4.4.1 Experimental setup

The Nuclear Reaction Chamber's target holder can carry up to 5 targets, depending on target size. All pellets were measured with a caliper in regards to the target holder's maximum height, with its top serving as the baseline, as represented in figure 4.5. Data

Figure 4.2: Lyophilized sample (left) and powdered sample (right)

Figure 4.3: Assembled pellet maker (left) and pressing process (right)

could be acquired consecutively across pellets through these measurements, by allowing correctly raising and lowering of the target holder inside the chamber.

For the purpose of this work, the top or bottom-most target was always a fluorescent material that served as a visual aid to check if the beam was correctly entering the chamber, with the help of a camera. If the beam was in contact with the fluorescent material, the camera lens would record a blue light emission and livestream it to the computer monitor. The intensity of this blue light was also a good indicator of how much beam current was reaching the target. Figure 4.6 shows a very intense light, which corresponds to roughly 25 nA of beam current hitting the fluorescent target.

The remaining target holder slots were used for pellet placement. Most pellets were

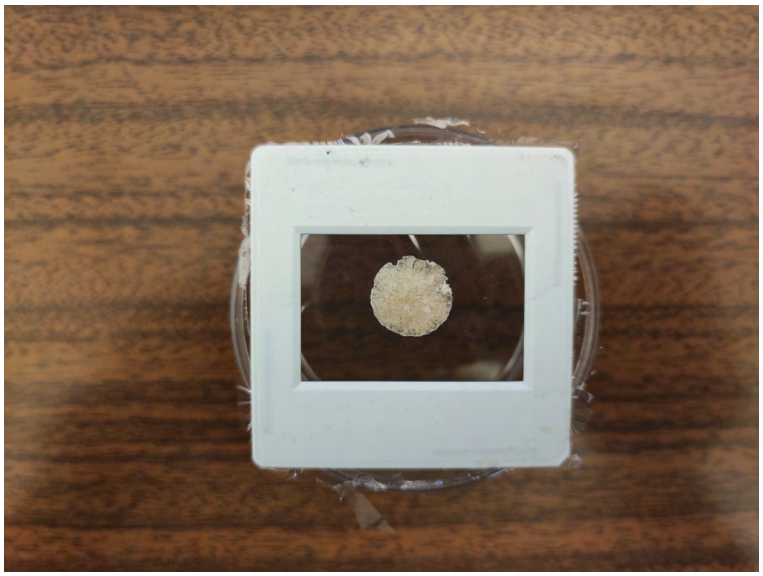

Figure 4.4: Final pellet for analysis

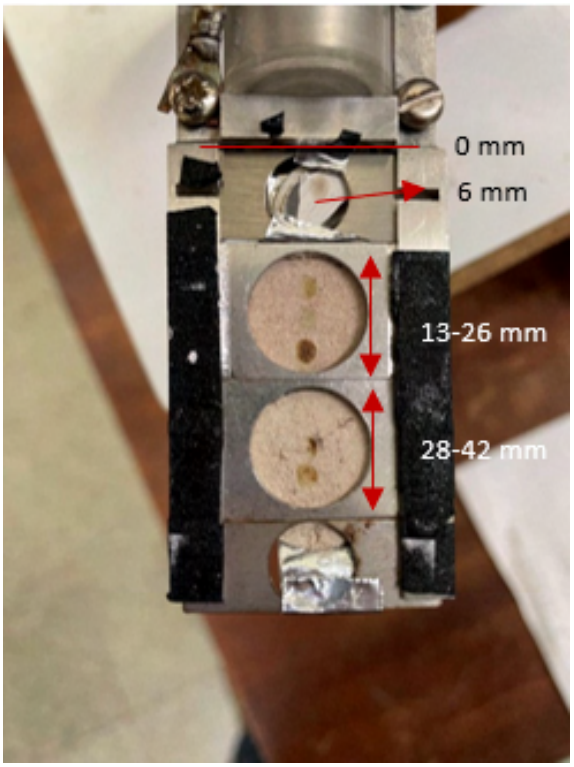

Figure 4.5: Pellet measurements

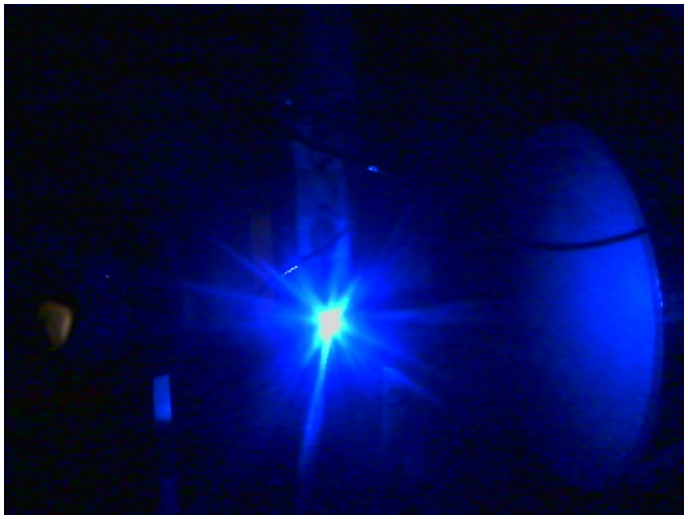

Figure 4.6: Fluorescence induced by a 25 nA beam current.

bombarded with protons in two distinct points to verify sample homogeneity, by analyzing and comparing the respective spectra. After analysis of all samples in the target holder, vacuum was broken and new samples were inserted.

4.4.2 Acquisition method

Each detector and electronic chain in the chamber was connected to an Analog-to-Digital Converter (ADC) that transformed the electrical signal into a digital signal. The spectra took shape over the course of 10-20 minutes and the dead time of the detectors was monitored throughout the duration of acquisition to avoid loss of statistic. Each set of spectra (2 EBS and 1 gamma) was then saved as a single column .mpa file. Each ADC had 8192 channels and each channel had an attributed spectrum data point, one for each file row. The .mpa file contained the data for all 3 ADCs. An example of acquired spectra is observable in figure 4.7.

4.5 Data Treatment

This section will cover the concepts and processes used for analysis of the EBS and the γ spectra taken from the biological tissue samples at the Tandem accelerator.

4.5.1 File Rearrangement

As a means to facilitate EBS spectra analysis, the spectra had to be compressed into 1024 channels instead of the default 8192. For that end, a Python program was created to read all the data regarding a single EBS spectrum from a .mpa file and rearrange it.

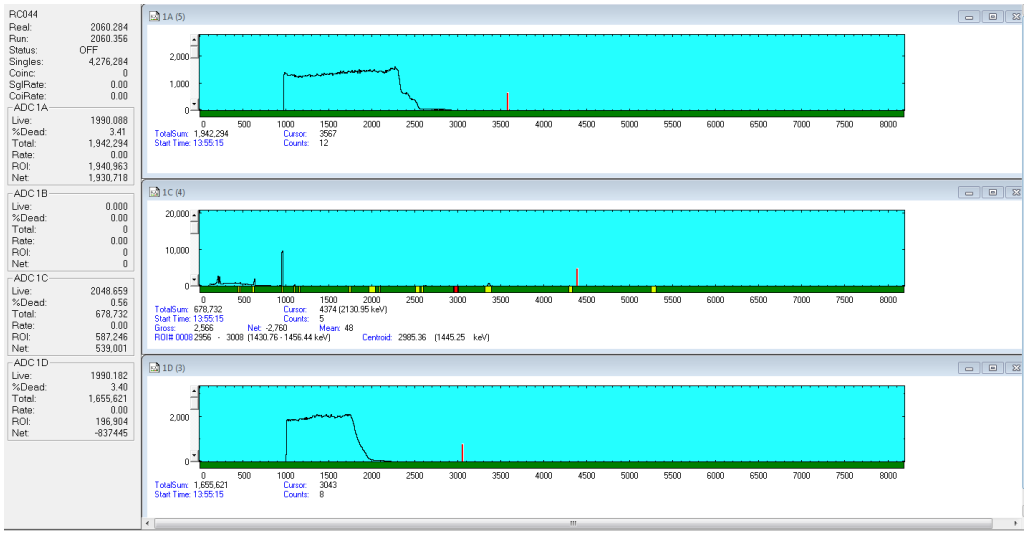

Figure 4.7: Spectra and respective ADCs, each with 8192 channels.

Firstly, all 8192 values of interest were selected and converted into a single column data frame with 8192 rows. These values were then added to each other in groups of 8 in the following way (equation (4.3)),

$$Value_{compressed}[x,0] = \sum_{k=1}^{8} Value_{default}[8(x+1)-k,0] \tag{4.3}$$

where $Value_{compressed}[x,0]$ is the new value for each of the 1024 rows , x is the new row number from 0 to 1023 and $Value_{default}[8(x+1)-k,0]$ is the default row value in the row number given by $8(x+1)-k$.

Subsequently, the 1024 new values had to be arranged in a readable format for the WiNDF software, which was the main tool used for EBS analysis. The most useful format was to rewrite the single column with 1024 rows as 128 rows with 8 columns each, as seen below in equation (4.4).

$$Value_{compressed}[x,0] = Value_{compressed}\left[\left\lfloor \frac{x}{8} \right\rfloor, r\left(\frac{x}{8}\right)\right] \tag{4.4}$$

$Value_{compressed}[x,0]$ is the value for each row in column 0, with x ranging from 0 to 1023, and $Value_{compressed}\left[\left\lfloor \frac{x}{8} \right\rfloor, r\left(\frac{x}{8}\right)\right]$ is the position of each value redistributed across 128 rows and 8 columns, where $\left\lfloor \frac{x}{8} \right\rfloor$ is the floor function of $\frac{x}{8}$ and $r\left(\frac{x}{8}\right)$ is the remainder of the division.

This format is specified to have the real time and the live time of the spectrum as its first two values. All EBS spectra had no data whatsoever in the first hundred channels, which allowed the replacement of the first two values of data with the real and live time without losing any sort of spectrum information.

The Python program also allowed the extraction of the 8192 values of the gamma spectrum to a single file, without the need of any processing.

All final files were saved with the .csv extension and were converted into .dat to be used in WiNDF.

4.5.2 EBS spectra analysis

EBS spectra were a fundamental stepping stone in this work's end-goal, granting a means to have an approximate elementary matrix composition of the biological tissue samples and for charge normalization. Collected charge is one of the required parameters for the yield equation in the PIGE technique, as stated in section 2.2.6. For that reason, it is imperative to simulate the spectrum data as best as possible with the help of WiNDF.

4.5.2.1 Simulation Fundamentals

WiNDF runs on 5 essential files for each EBS spectrum: a .spc, a .geo, a .str, a .dat and a ndf.prf files [58].

The .spc file is the batch file, and it accesses all the other files to run the simulation. It also includes the collected charge as one of its parameters.

The .geo file contains all the parameters that involve the beam and the target geometry, such as the type of incident particles, the type of scattered particles, the beam energy, the angle at which the scattered particles are detected, the energy resolution of the detector and the fitting interval, among others.

The .str file is where the elements present in the sample are defined. These elements can either have a fixed atomic fraction, unchangeable with the type of simulation, or be allowed to vary when running a simulation to optimize each element's atomic fraction to better fit to the experimental data.

The .dat file contains the experimental data that the simulation will try to fit and the ndf.prf file defines the amount of layers in the sample, each layer's thickness and the atomic fraction of each element in each layer.

For all spectra, some parameters were kept constant, mainly in the .geo and .str files. In the .geo file, both the incident and the scattered particles were protons, the beam energy was roughly 2.8 MeV, the scattering angle was 152.4º and the detector resolution was 30 keV. The .str files all contain carbon, hydrogen initially fixed at an atomic fraction of 63%, nitrogen, oxygen, sodium and phosphorus. Iron was also included for some spectra, since the beam slightly contacted the target holders in some measurements. Hydrogen is not detectable in the EBS spectra but it is one of the main constituents of the biological tissue. Thereby, standardized hydrogen values for soft tissue were taken from NIST - National Institute of Standards and Technology as a way to bypass the lack of information regarding hydrogen in the EBS technique. Hydrogen's mass fraction for soft tissue was approximately 10.4% which converted to an atomic fraction of 63%. This value was still much higher than intended, since there was a significant non-detectable hydrogen loss due to sample lyophilization.

With this in mind, further testing regarding hydrogen was also done with WiNDF, by running simulations where hydrogen's atomic fraction values were in the range of 10-63%. The results of these tests showed that the spectra would always keep their shape, regardless of hydrogen concentrations, but would have slight shifts in the yielded charge, as displayed below in figure 4.8.

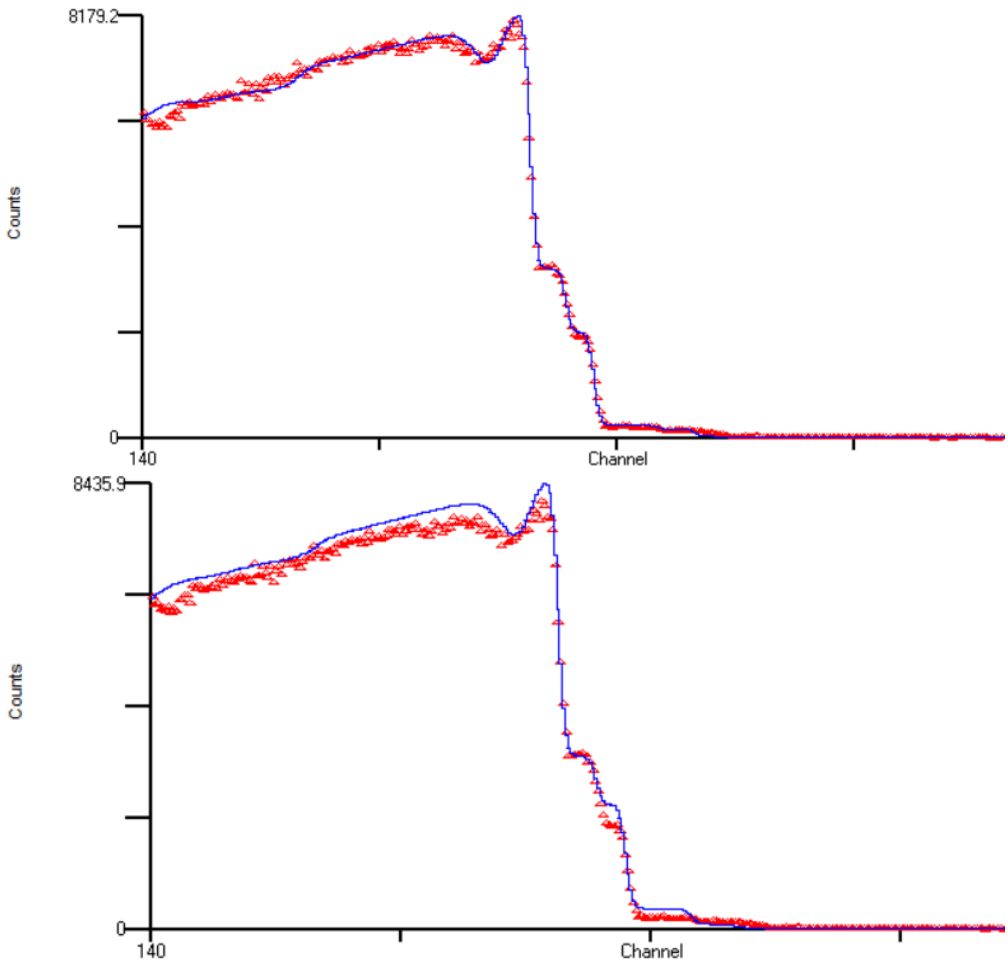

Figure 4.8: Charge shift due to hydrogen variations: hydrogen set to 63% (top) and hydrogen set to 35% (bottom). The blue line represents the simulated spectrum and the red triangles are the experimental data.

In the end, a hydrogen mass fraction of 30% was assumed to be a reasonable assessment for the lyophilized samples.

4.5.2.2 Running simulations

Considering there were no changes in the other files, and for each and every spectrum, the simulations began by inserting an initial guess for each element's atomic fraction in the ndf.prf file, according to the elements present in the .str file. Only one layer was used, under the assumption the pellets had an homogeneous element distribution.

After each simulation, the fractions were altered in order to best fit the spectrum to the experimental data, as a means to ensure that the following optimization process was as accurate as possible.

The main criteria for fitting the experimental data were the oxygen resonance, the carbon peak, the nitrogen barrier, the oxygen barrier and the heavier elements barriers, such as phosphorus and sodium. Each of these zones, as well as each element's individual EBS spectrum, is represented in figure 4.9.

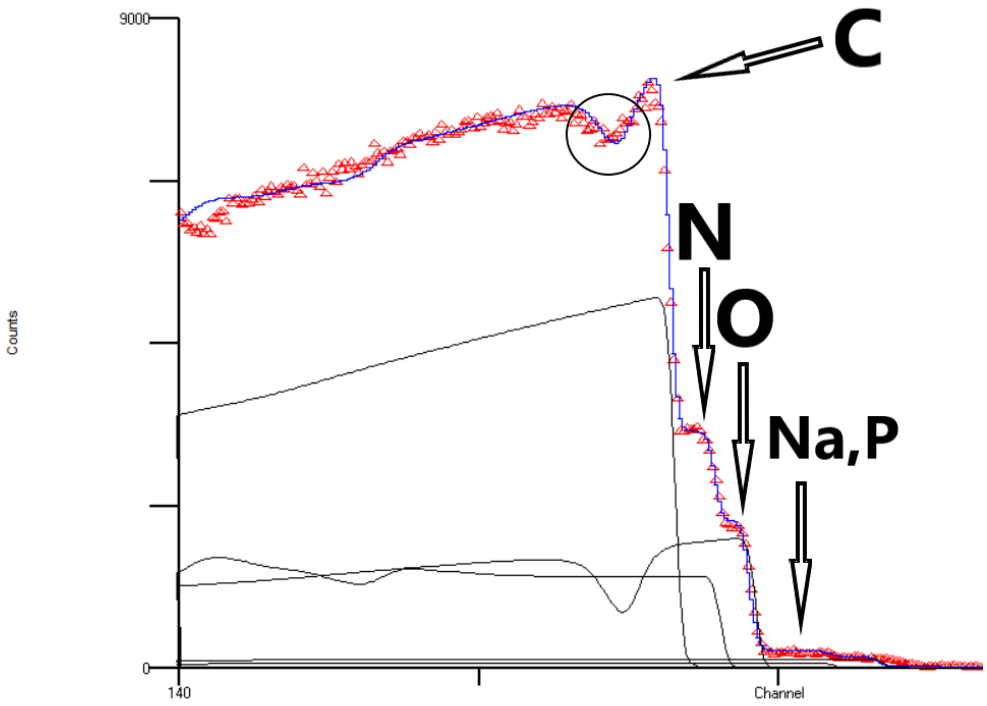

Figure 4.9: Biological tissue EBS spectrum: C - carbon peak; N - nitrogen barrier; O - oxygen barrier; Na,P - heavier elements barrier, like sodium and phosphorus. The circled area represents the oxygen resonance. All of these zones can be seen individually in the separate EBS spectra.

Both the oxygen resonance and the oxygen barrier were adjusted by increasing or decreasing the oxygen atomic fraction, while at the same time decreasing or increasing its carbon counterpart, respectively. The nitrogen barrier was adjusted the same way: increasing or decreasing the nitrogen atomic fraction to the detriment of carbon. The carbon peak was almost passively fitted, since it's comprised of the sum of each element's respective EBS spectrum in that region. For this reason, altering the quantities of oxygen and nitrogen at the expense of carbon did not affect the fitting of the peak significantly, since these are the most abundant elements and their total sum had approximately stayed the same. The heavier elements barriers were only roughly fitted due to lack of statistics, as shown in figure 4.10. Since these heavier elements were mostly sodium and phosphorus, which would be quantified later on recurring to gamma spectra, there was no need

for a more accurate fitting.

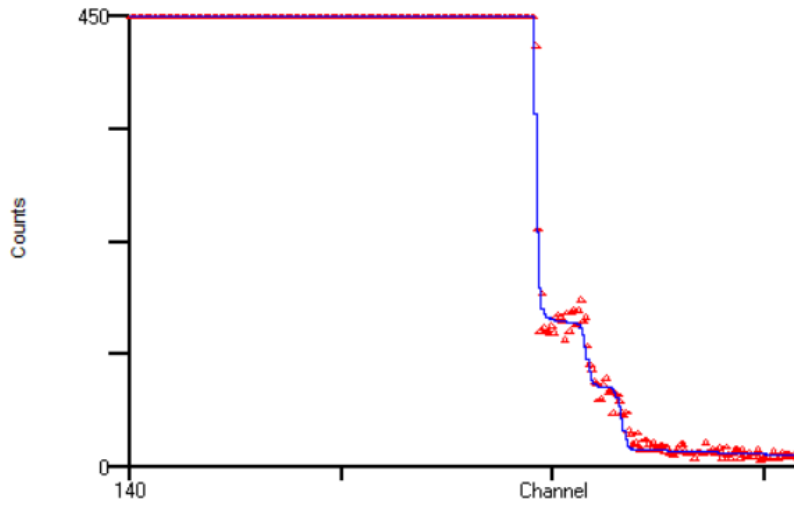

Figure 4.10: Sodium and phosphorus EBS fitting.

After adjusting to the criteria above, a final optimization was done. By searching from the ndf.prf file, the software allows for maximum fitting by slightly changing the atomic fractions and the collected charge to yield the best simulation of the experimental data. All final values were saved to be used afterwards.

4.5.3 Gamma spectra analysis

The gamma spectra carry the most information regarding this work's end-goal. The analysis of these spectra consisted on identifying which observable gamma peaks corresponded to each element, by firstly calibrating each channel to its respective energy value, and then extracting the areas of the relevant peaks to obtain the yield of that particular nuclear reaction.

4.5.3.1 Energy Calibration

The calibration was done with a radioactive ^{60}Co source, placed near the nuclear reaction chamber. The ^{60}Co decays into ^{60}Ni and, in the process, emits gamma-rays of 1173 and 1332 keV. The centroid channel for each one of these peaks was registered and used to attain a linear calibration equation in the form of $Energy = k * Channel + b$ where k and b are arbitrary values.

This calibration was done before the spectra acquisition, to allow the monitoring of the elements in the gamma spectra and to correlate them to the beam and sample conditions. As an example, aluminium peaks at 844 keV and 1014 keV were dominant in some spectra where the sample was cracked or misplaced due to poor conditioning, as the beam would pass through it and interact with other chamber components.

4.5.3.2 Gamma Peak Identification

All the data was loaded in OriginLab and the gamma spectra were analyzed one by one. The x-axis for each spectra was displayed according to the respective energy calibration. Figure 4.11 depicts one of the analyzed spectra. The circled peaks in the figure correspond to the elements that were most prone to analysis due to their high cross-section, and were present in every spectrum.

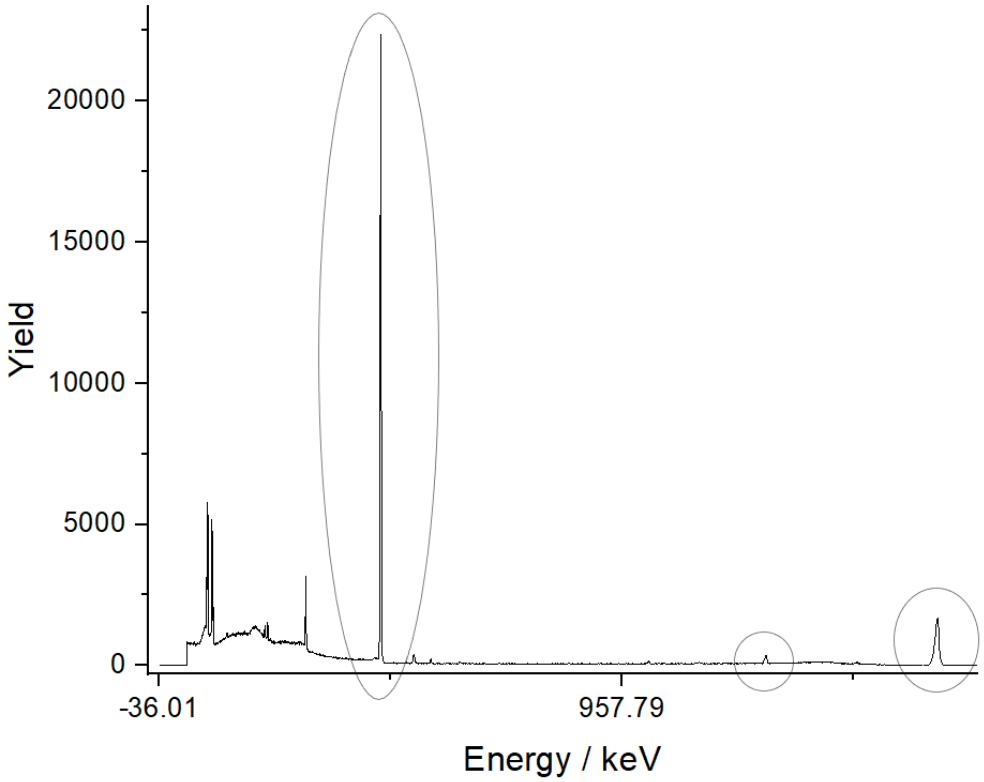

Figure 4.11: Gamma spectra for sample 331-4h30 in formalin.

The left-most circled peak is the 440 keV sodium peak and it originates from the ^{23}Na(p,p$_1\gamma$)^{23}Na nuclear reaction. The middle circled peak is the 1266 keV phosphorus peak, with ^{31}P(p,p$_1\gamma$)^{31}P as its originating nuclear reaction. The right-most circled peak is another sodium peak, at 1634 keV, and this γ-ray is emitted when the ^{23}Na(p,$\alpha_1\gamma$)^{20}Ne reaction occurs.

Additional peaks were also observable and identifiable across all the spectra. In the low-energy end, gold from the collimator emits a 68.806 keV Kα and a 77.982 kev Kβ x-rays, as well as a 279 keV γ-ray from its (p,p'γ) nuclear reaction. Other frequent gamma emissions were the aluminium's 844 and 1014 kev, whose nuclear reactions were ^{27}Al(p,p$_1\gamma$)^{27}Al and ^{27}Al(p,p$_2\gamma$)^{27}Al, respectively [34], the 511 keV from positron annihilation due to pair production and the 1460 keV from the radioactive behaviour of ^{40}K, which is a naturally occurring and abundant contaminant that decays to ^{40}Ar.

4.5.3.3 Peak Area Extraction

A first approach for retrieving peak areas was to use an analysis technique to remove the Compton background from each spectrum. The chosen technique was the asymmetric least squares smoothing, in which through the adjustment of several parameters, a background curve would be subtracted from the spectrum, setting the baseline of the peaks to 0. The peaks would then be integrated along the peak's width for area retrieval. This method was discarded early on, since the smoothing curve could not be rigorously adjusted to the spectrum due to its high background noise in the low energy region, which would in turn lead to some noise integration while trying to extract the areas of the peaks.

A more appropriate method was found by fitting the peaks with a Gauss curve. Most peaks could be fitted with a single Gauss curve plus a horizontal line, y_0, for background subtraction, except for the 1634 keV which required a double Gauss curve in order to be properly fitted. This technique allowed a more precise area extraction, as well as a fitting error that for uncertainty calculation purposes was considered to be the uncertainty associated to the peak area. Figure 4.12 depicts how well the Gauss curve was fitted to the 440 keV gamma peak, as well as the respective fitting parameters.

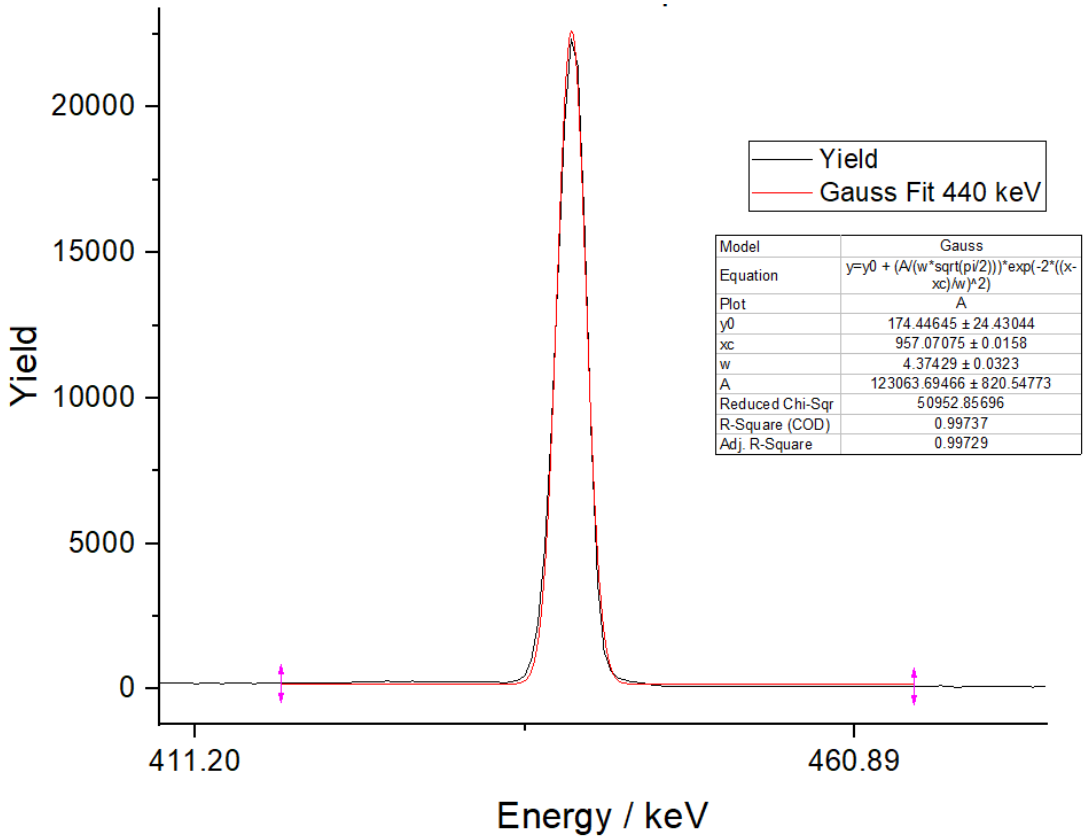

Figure 4.12: Gauss fit for the 440 keV gamma peak

Since the 1634 keV peak was double fitted, its area uncertainty was calculated the following way

$$\delta_{A_{1634keV}} = \sqrt{\delta_{G1}^2 + \delta_{G2}^2} \tag{4.5}$$

where δ_{G1} and δ_{G2} are the fitting uncertainties of the first and second Gauss curves, respectively.

Within the scope of this work, only the areas of the sodium and phosphorus peaks were registered, as they were subsequently used for quantification of these elements. The remaining element peaks did not come from the samples, thus not being useful.

4.6 Element quantification

The quantification of the studied elements was done with the help of ERYA-Bulk, as previously stated. ERYA-Bulk has an extensive database containing several gamma emission cross-sections, stopping power functions and a detector efficiency curve for the HPGe. While running simulations, this database is accessed to solve for equation (2.31). A few of the accessible excitation functions in the ERYA database are represented in figure 4.13.

The desired outcome of ERYA simulations is to have an approximate value of the mass/atomic fraction of the elements whose areas were retrieved while analysing the gamma spectra, as long as their cross-section functions exist in the database. To achieve this, ERYA must be given the collected charge, the maximum beam energy, the elements in the sample as well as their respective atomic fractions and the experimental yield of the registered gamma-emitting reactions.

The collected charge was acquired during EBS spectra fitting, the maximum beam energy was set to 2.8 MeV throughout sample analysis, the atomic fractions of the elements in the samples were as used in the ndf.prf files and the experimental yields were taken from the gamma spectra.

Throughout the simulations of this work, a standard ERYA-Bulk interface would look like the one shown in figure 4.14.

The final output of the simulations were sodium and phosphorus's mass fraction in each sample.

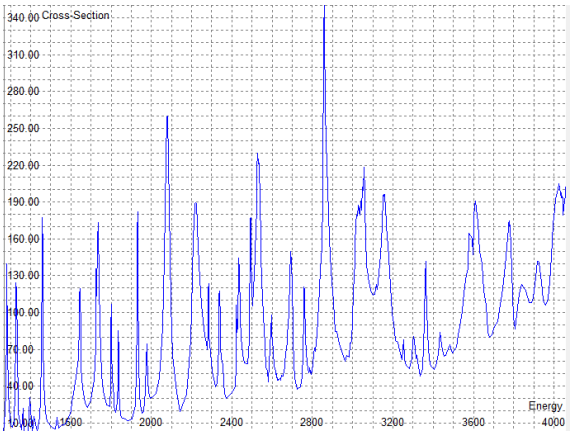

(a) ^{23}Na 440 keV gamma emission cross-section as a function of beam energy

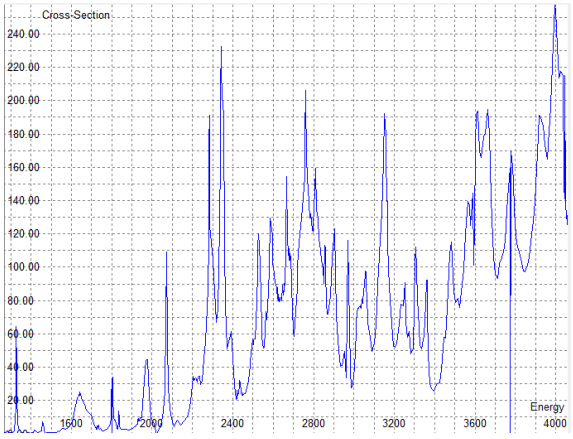

(b) ^{23}Na 1634 keV gamma emission cross-section as a function of beam energy

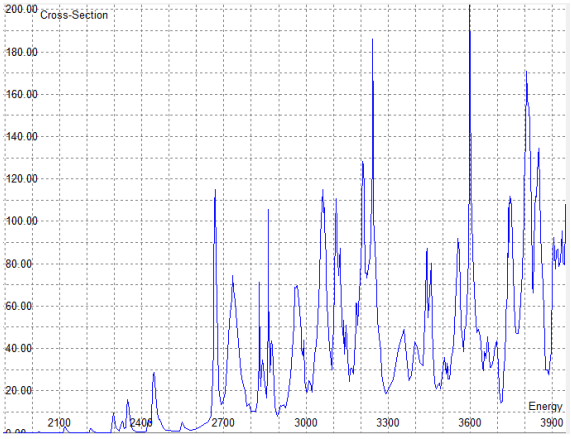

(c) ^{31}P 1266 keV gamma emission cross-section as a function of beam energy

Figure 4.13: Cross-section functions for the ^{23}Na(p,p$_1\gamma$)^{23}Na, ^{23}Na(p,$\alpha_1\gamma$)^{20} and ^{31}P(p,p$_1\gamma$)^{31}P nuclear reactions

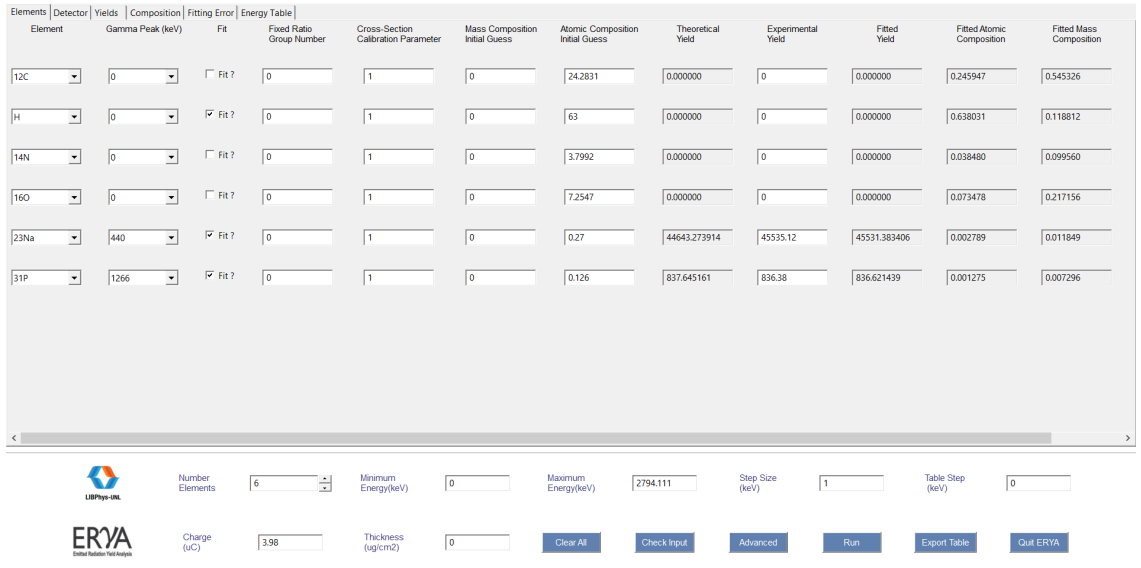

Figure 4.14: ERYA interface

5

Results and Discussion

The following chapter exposes and discusses the final results of this study, regarding light element sample content, namely sodium and phosphorus, after progressive FF.

5.1 Uncertainty calculation

As mentioned previously, the PIGE yield equation (2.31) in section 2.2.6, lays the foundation for this work's results. The formula can be rearranged to isolate the wanted variable, which is the mass fraction of the studied element, as presented in equation (5.1).

$$f_m = \frac{4\pi \cdot \epsilon_{abs}(E_\gamma) \cdot \left(\frac{Q}{e}\right) \cdot \cdot f_i \cdot N_{av} \cdot A^{-1} \cdot \int_0^{E_0} \frac{\sigma(E,\theta)}{S_m(E)} dE}{Y(E,\theta)} \tag{5.1}$$

The uncertainty for f_m was calculated by uncertainty propagation. Since N_{av}, A^{-1} and f_i are constants, only the uncertainties of $\epsilon_{abs}(E_\gamma)$, $\frac{Q}{e}$, $\sigma(E,\theta)$, $S_m(E)$ and $Y(E,\theta)$ were considered.

The uncertainty propagation formula of a multiplication or a division of variables can be written as the square root of the sum of each variable's squared relative uncertainty. For this specific case, the relative uncertainty of f_m was given by equation (5.2).

$$\delta_{f_m} = \sqrt{\delta^2_{\epsilon_{abs}} + \delta^2_{\frac{Q}{e}} + \delta^2_{\sigma(E,\theta)} + \delta^2_{S_m(E)} + \delta^2_{Y(E,\theta)}} \tag{5.2}$$

Table 5.1 shows the values used for each uncertainty.

The relative uncertainty of the gamma yields is not represented since it varies with sample and gamma energy. Every single one of them was calculated by dividing the absolute uncertainty of each peak area by the corresponding area, according to the respective Gauss fit. Also, the uncertainty associated with the collected charge is a systematic uncertainty, since it was calculated based on the observable charge shift in the EBS spectra due to hydrogen variation. As explained in 4.5.2.1, the hydrogen atomic fraction was reasonably assumed to be 30%. The charge uncertainty was calculated by presuming that the hydrogen atomic fraction could vary from 20 to 40%. The relative uncertainty of collected charge between the assumed value and the variance range was 4.3%.

Table 5.1: Relative uncertainties of PIGE equation variables.

$\delta_{\epsilon_{abs}}$	5.0%
$\delta_{\frac{Q}{e}}$	4.3 %
$\delta_{\sigma(440,\theta)}$	3.2%
$\delta_{\sigma(844,\theta)}$	4.2%
$\delta_{\sigma(1014,\theta)}$	5.1 %
$\delta_{\sigma(1266,\theta)}$	4.0 %
$\delta_{\sigma(1634,\theta)}$	4.1 %
$\delta_{S_m(E)}$	5.0%

5.2 Influence of FF time on soft tissue sodium content

Sodium mass fraction (SMF) for each sample set was calculated resorting to both the 440 keV and the 1634 keV sodium gamma peaks. For each type of analyzed tissue, both plots were examined regarding the variation of sodium with increasing FF time. They were also compared to one another, as calculations for both peaks should yield the same results.

5.2.1 Colon tissue

There were two colon data sets that were surveyed for the purposes of this work. Figure 5.1 portrays how colon #1 sodium content changed during a 14 day FF time span.

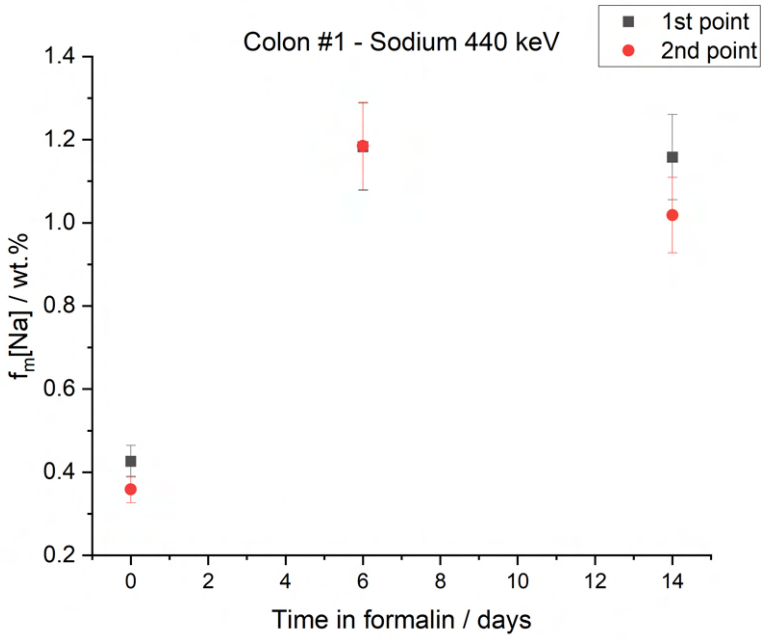

Figure 5.1: Plot of sodium mass fraction as a function of FF time for the Colon #1 data set, using the 440 keV gamma peak. Both 6-day data points are overlapped.

Across all data points, it is possible to infer that samples with 6 and 14 days of FF present a SMF about 3 times higher than that of the fresh sample, even though there is not enough statistic to parameterize an evolution curve.

The data points taken from the 1634 keV sodium gamma peak are represented in figure 5.2.

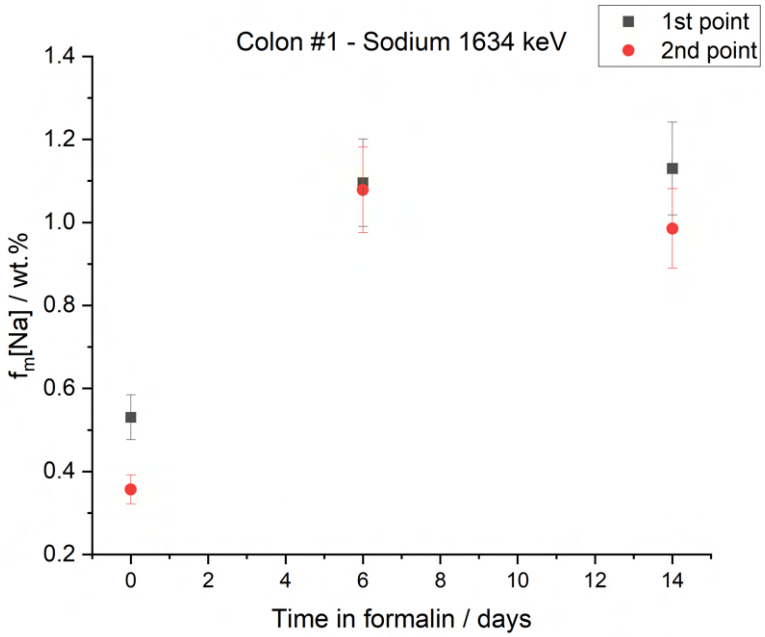

Figure 5.2: Plot of sodium mass fraction as a function of FF time for the Colon #1 data set, using the 1634 keV gamma peak.

Although the values are not exactly the same as those in figure 5.1, the difference between the 440 keV and the 1634 keV data seems to be a modest 10%, on average. The reasons for this difference are still being investigated. In spite of this, the overall data distribution follows the same trend. The 6-day sample data points show equal values within the error bar range, and there is a wider gap between the fresh sample data points, most probably because the samples were not completely homogeneous. One noteworthy feature of both plots is how the SMF appears to be at a plateau after the 6-day FF time, as the 14-day data points do not deviate significantly from the 6-day data, at least when compared to the fresh sample data points.

Regarding the colon #15 data set, subfigures a) and b) of figure 5.3 represent how sodium content changed throughout a 5-day FF time period, with the first recurring to the 440 keV gamma peak and the latter to the 1634 keV gamma peak.

The plots present a striking resemblance when compared to those of the colon #1 data set. Once again, there is a very significant increase of sodium content after a few days of FF, for the reason that the 5-day data point indicates twice as much SMF than the average of the fresh data points. The aforementioned plateau is still within error bar

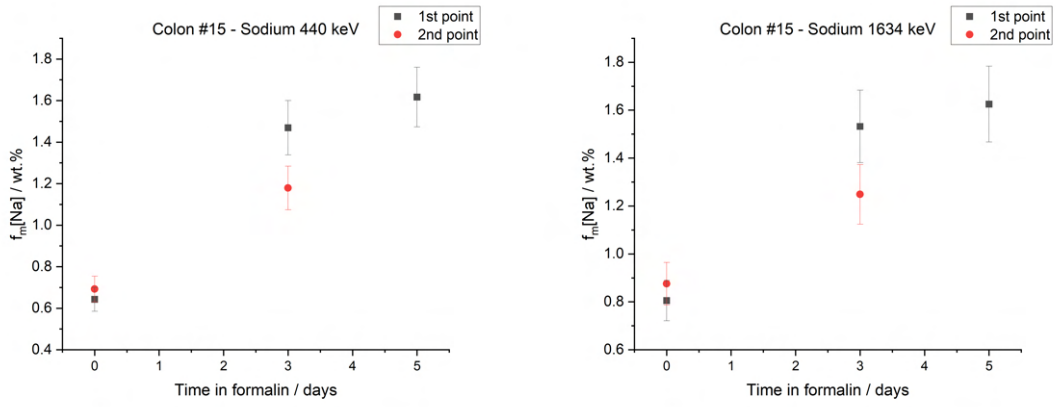

(a) Plot of sodium mass fraction as a function of FF time for the #15 Colon data set, using the 440 keV gamma peak.

(b) Plot of sodium mass fraction as a function of FF time for the #15 Colon data set, using the 1634 keV gamma peak.

Figure 5.3: Plots of sodium mass fraction as a function of FF time for the #15 Colon data set for each gamma peak.

range, even though the time span of FF is much shorter. Additionally, colon #15 presents higher values of SMF for all data points when compared to colon #1.

5.2.2 Ileon tissue

Ileon tissue has better statistics than the colon tissue when it comes to SMF. Figures 5.4 and 5.6 represent SMF over a period of 24 days of FF, for 440 keV and 1634 keV, respectively.

Figure 5.4 shows there is a steep SMF increase between the fresh data points and the 2-day data points. From that point onward, SMF keeps increasing but at a steadier rate. The 24-day data points indicate a small decrease of SMF from the 12-day data points, possibly hinting at a sodium stabilization over longer periods of time. However, it is also possible that there is a stabilization of SMF across all data points with FF time, since the oscillations due to error bars are compatible with a horizontal plateau around the 1.5% SMF mark, as shown in figure 5.5.

At the same time, figure 5.6 shows a very similar SMF evolution. Once again, there is a very clear difference in SMF between the formalin-fixated samples and the fresh samples. The data points seem to slightly increase and decrease in SMF over time, but within the error bars the plateau observed in the 440 keV plot is maintained around the 1.5% SMF mark, as depicted in figure 5.7.

5.2.3 Spleen tissue

Spleen tissue has SMF data from fresh, 5-day FF and 9-day FF, represented in subfigures a) and b) of figure 5.8 for 440 keV and 1634 keV respectively. Both plots have very

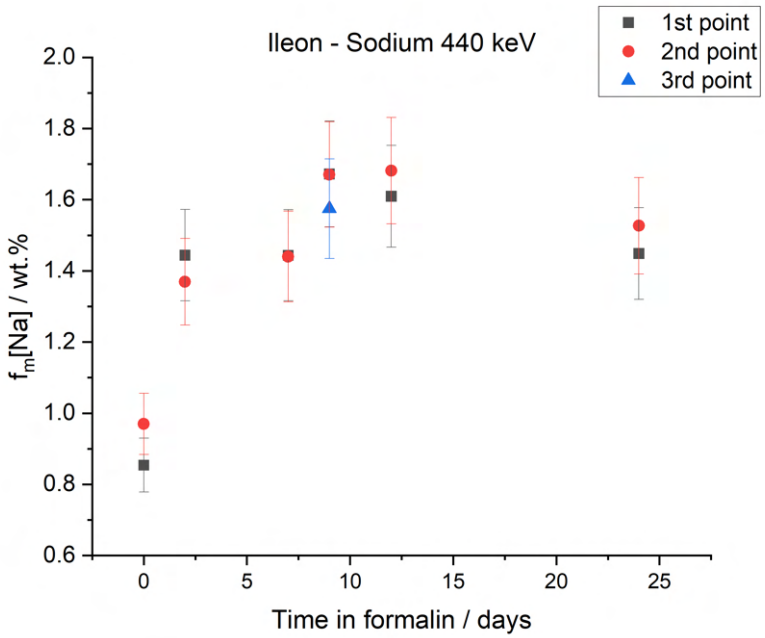

Figure 5.4: Plot of sodium mass fraction as a function of FF time for the ileon data set, using the 440 keV gamma peak.

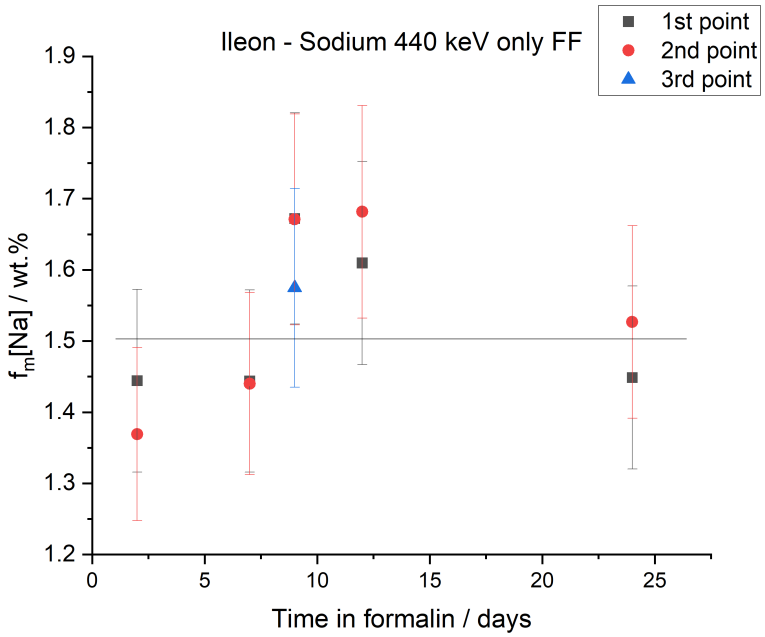

Figure 5.5: Plot of sodium mass fraction as a function of FF time for the ileon formalin-fixated samples, using the 440 keV gamma peak. The black line represents a plateau within the error bars across all data points.

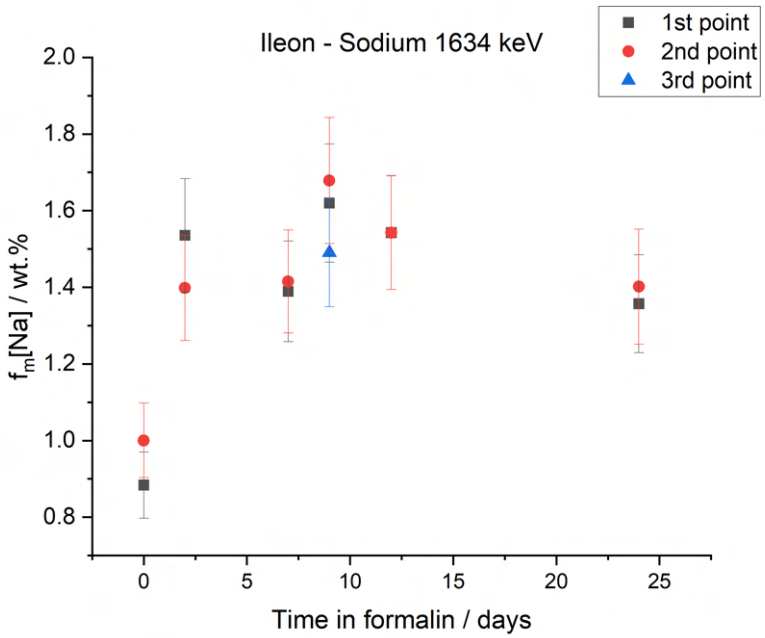

Figure 5.6: Plot of sodium mass fraction as a function of FF time for the ileon data set, using the 1634 keV gamma peak.

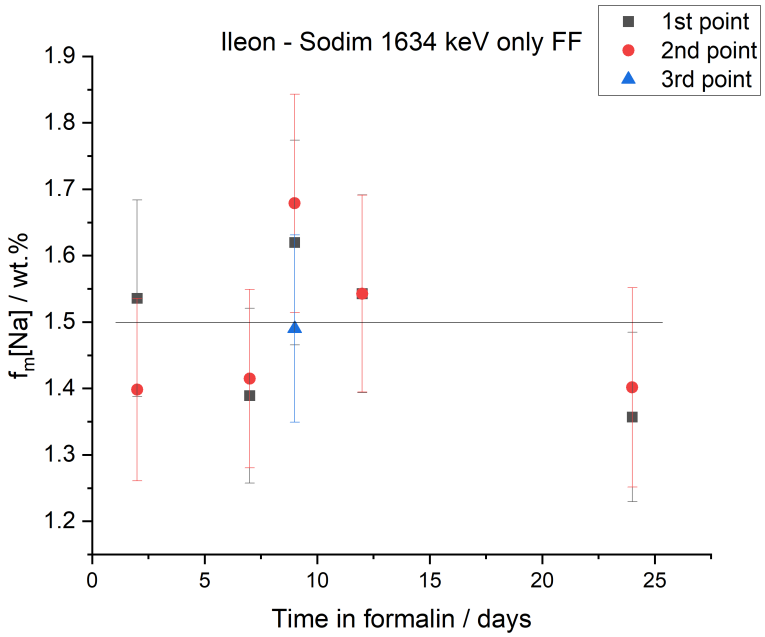

Figure 5.7: Plot of sodium mass fraction as a function of FF time for the ileon formalin-fixated samples, using the 1634 keV gamma peak. The black line represents a plateau within the error bars across all data points.

similar data points, which means the calculations for the 440 keV and 1634 keV peaks were in agreement.

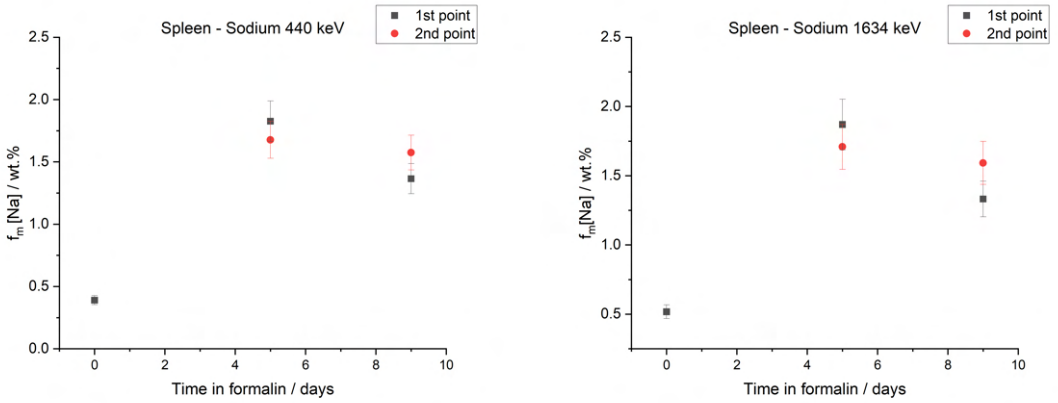

(a) Plot of sodium mass fraction as a function of FF time for the spleen data set, using the 440 keV gamma peak.

(b) Plot of sodium mass fraction as a function of FF time for the spleen data set, using the 1634 keV gamma peak.

Figure 5.8: Plots of sodium mass fraction as a function of FF time for the spleen data set for each gamma peak.

Yet again, the 5-day and 9-day formalin fixated samples have much higher sodium concentrations than the fresh samples. According to both plots, after 5 days of FF, the SMF peaks in the 1.5%-2.0% range, which is almost a 300% sodium increase when comparing to the SMF of the fresh samples. At 9 days of FF, a small decline of about 0.3% of SMF is observable.

5.2.4 Muscle tissue

Conversely to the other tissues, muscle tissue data sets were harvested in a later date and solely for this work's purposes, to corroborate previous findings. It was speculated among the work group that most of the element trade-offs between the tissue and the formalin happened very shortly after FF, which means these data sets have much shorter FF times.

Since all the retrieved data sets were comprised of the same tissue, they were analyzed together in order to bypass the lack of data that existed due to some samples not being suitable for PIGE analysis. Plots for individual muscle data sets SMF are displayed in I.

Figure 5.9 displays all data points from all samples across all muscle data sets.

Seeing the data is very cluttered, an average SMF between points of the same sample and points of all samples with the same FF time was made in order to better examine the data.

Data points 329-24h and 328-48h were discarded for these calculations as they behave very differently from the remaining data points in their respective FF time. This happened

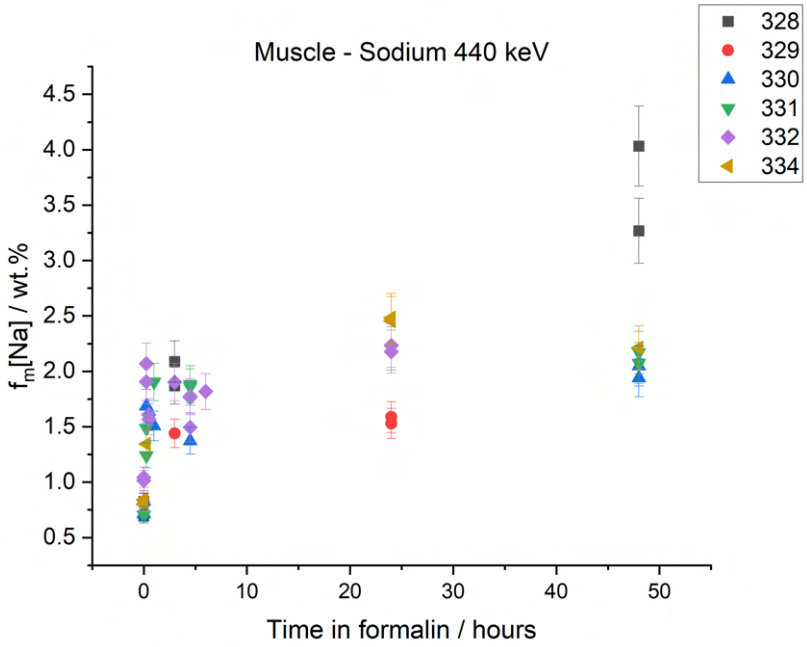

Figure 5.9: Plot of sodium mass fraction as a function of FF time for the muscle data sets, using the 440 keV gamma peak.

as a consequence of unusual elements, such as iron, in the respective EBS spectra, which greatly affected the ERYA simulation results and made them inaccurate.

By averaging data points for each sample, a trend starts to become visible, as depicted in figure 5.10

It is clearly noticeable how the SMF almost instantaneously rises once the FF time begins. 15 minutes in into the FF time, there is already a considerable increase in the SMF. At 24 hours, the tissue reaches its peak SMF, decreasing slightly over the next 24 hours.

Further decluttering of the data can be done by averaging points from all samples with the same FF time instead of averaging data point for each sample. Figure 5.11 portrays a plot of those averages.

This plot emphasizes not only the sudden SMF increase after 15 minutes of FF, but also characterizes its behaviour over the next few hours. After the first 15 minutes, and if the 4h30m data point is not taken into account, there is a steady increase of the SMF, at least until the 6-hour time mark. The fact that the SMF peaks at the 24-hour time mark suggests that it might keep steadily increasing until it reaches that point. The 48-hour data point indicates a decrease after the first day of FF, but there is not enough data to ensure if this is what actually occurs.

The same procedure was applied to the 1634 keV data points, to verify the results obtained with the 440 keV data points. The end-plot is displayed in figure 5.12.

Both plots are very similar, even if there are a few data points that do not exactly

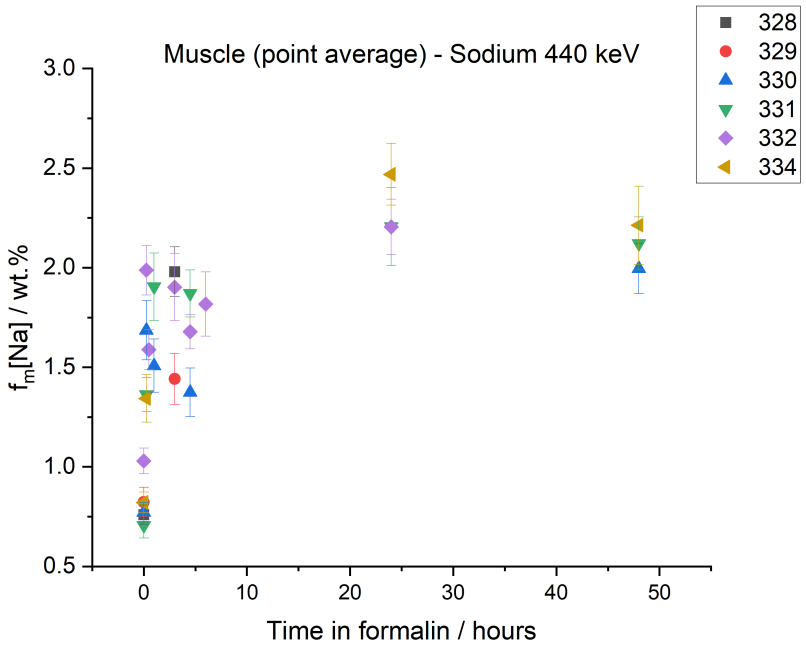

Figure 5.10: Plot of sodium mass fraction as a function of FF time for the muscle data sets, using the 440 keV gamma peak. Each data point in the plot is an average value of data points from the same sample.

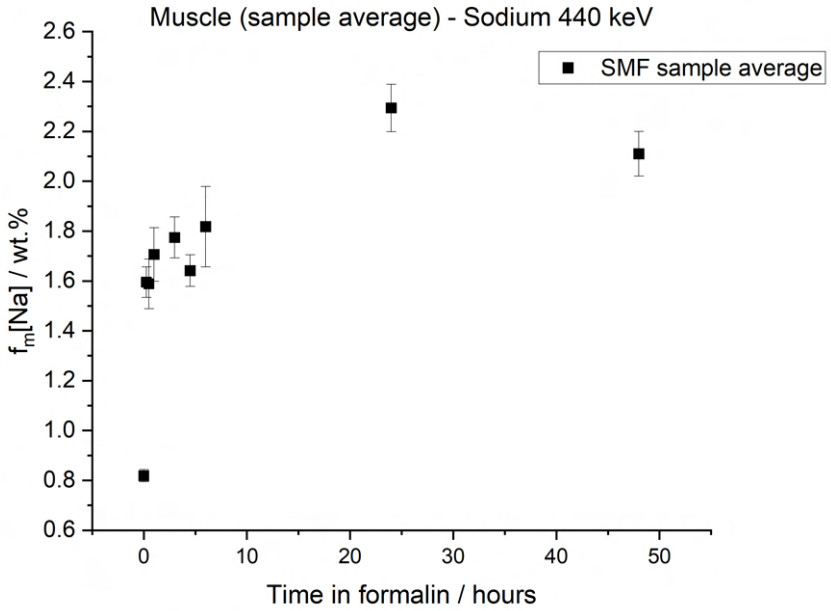

Figure 5.11: Plot of sodium mass fraction as a function of FF time for the muscle data sets, using the 440 keV gamma peak. Each data point in the plot is an average value of data points from all samples with the same FF time.

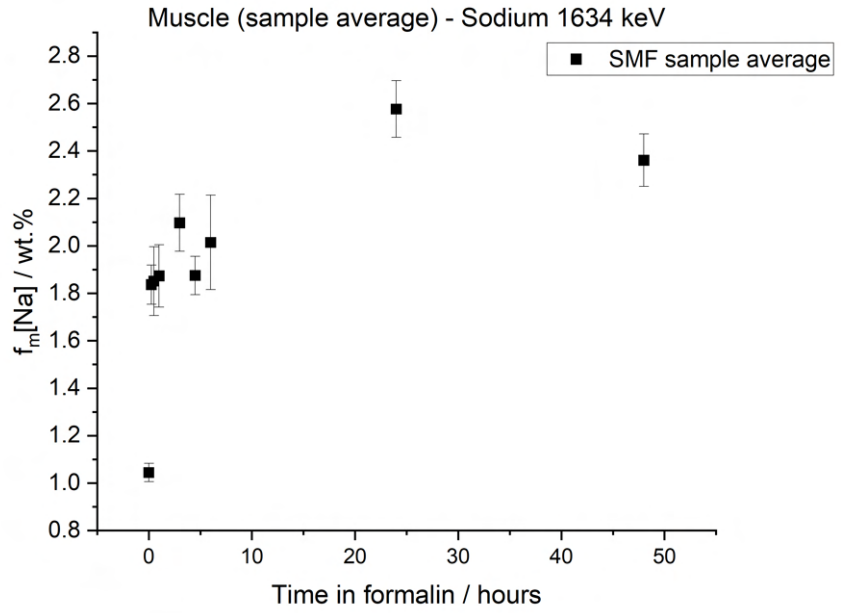

Figure 5.12: Plot of sodium mass fraction as a function of FF time for the muscle data sets, using the 1634 keV gamma peak. Each data point is an average value of data points from all samples with the same FF time.

match in terms of the curve shape. One interesting feature of the 1634 keV plot is the fact that the SMF data points seem to have slightly higher average values when compared to those of the 440 keV plot. Nevertheless, the ascending SMF trend is maintained, which allows to infer that there is in fact a rapid increase in SMF in the first 15 minutes of FF and a slow increase until the first full day of FF.

5.3 Influence of FF time on soft tissue phosphorus content

Phosphorus mass fraction (PMF) was quantified resorting to the 1266 keV phosphorus gamma peak. Since there was only one detectable gamma peak for this element, each tissue only has one PMF plot as a function of FF time.

5.3.1 Colon tissue

Unlike its sodium counterpart, PMF presents very distinct behaviours between the #1 and #15 data sets, even though their FF time frames are very different.

Figure 5.13 shows the PMF variation throughout a 14 day time frame for the #1 Colon data set.

The plot indicates a very significant phosphorus increase during the first 6 days of FF, as the 6-day data points reflect PMF values about twice as large as those of the fresh data-points. This is followed by a subsequent PMF falloff after a fortnight of FF, possibly

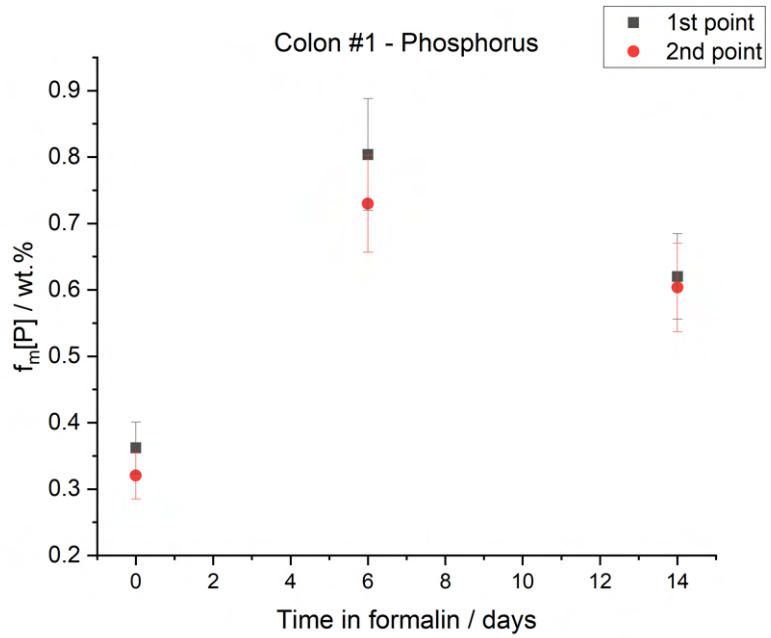

Figure 5.13: Plot of phosphorus mass fraction as a function of FF time for the Colon #1 data set.

indicating that phosphorus content, just like sodium, might also stabilize and plateau over longer periods of FF.

On the other hand, figure 5.14 depicts the PMF variation for the #15 Colon data set over a period of 5 days of FF.

Overall, the PMF values are much higher in this data set, with the fresh sample data points averaging twice the values of their counterpart. Curiously, the evolution of phosphorus over the 5-day period in which the samples were fixated shows an almost linear increase of PMF, peaking at the 5-day time mark.

The provided data of both data sets is not sufficient to describe accurately how phosphorus colon content shifts over a two week period of FF, but it is possible to infer, however, that FF over a few days triggers a phosphorus increase in this type of soft tissue.

5.3.2 Ileon tissue

The evolution of PMF in formalin-fixated ileon tissue is portrayed in figure 5.15.

Once again, the fresh tissue has the lowest PMF of all the analyzed samples, with all the other samples averaging at least twice the average of the fresh data points. During the first 9 days of FF, phosphorus seems to increase at an almost linear rate. PMF then seems to slowly decay until the 24-day time mark, where it reaches its lowest values of the previous 15 days. Nevertheless, by considering an approach based on the error interval of all formalin-fixated data points, it is possible to establish a plateau across all data points that sits around the 0.9% PMF, as portrayed in figure 5.16.

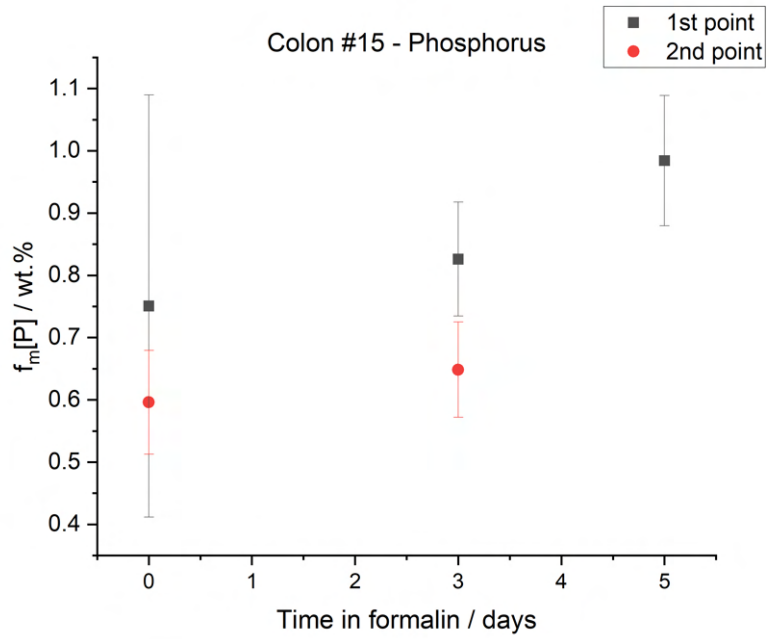

Figure 5.14: Plot of phosphorus mass fraction as a function of FF time for the Colon #15 data set.

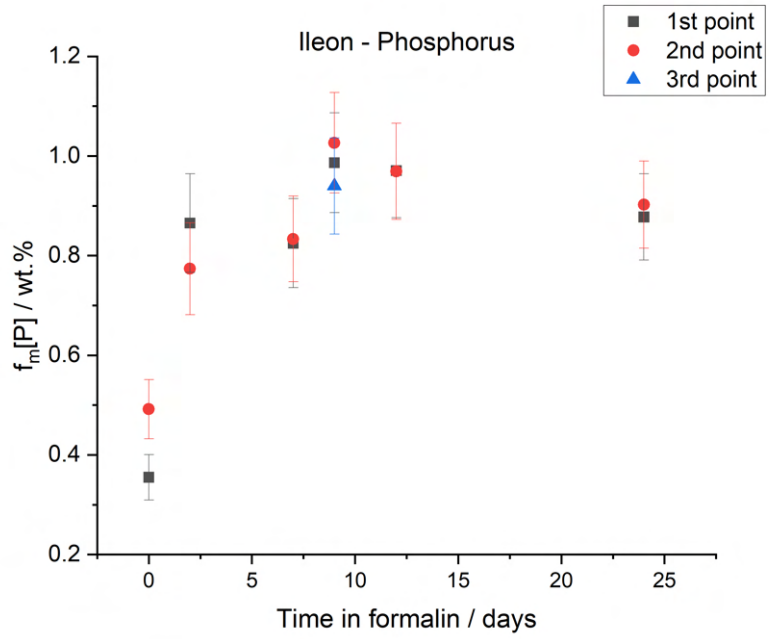

Figure 5.15: Plot of phosphorus mass fraction as a function of FF time for the ileon data set.

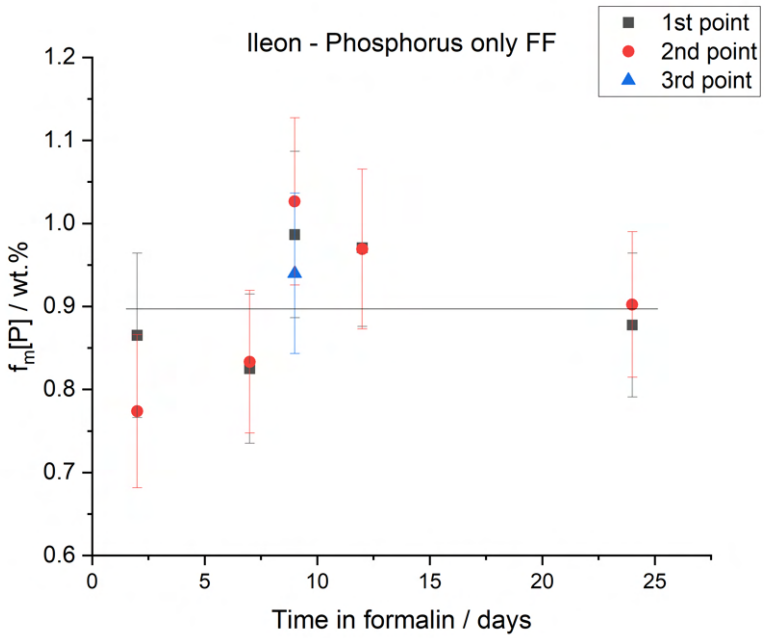

Figure 5.16: Plot of phosphorus mass fraction as a function of FF time for the ileon formalin-fixated samples. The black line represents a plateau within the error bars across all data points.

5.3.3 Spleen tissue

Spleen is a particular tissue regarding phosphorus content, since its baseline PMF is (1.09 ± 0.12 %), which is a value much higher than that of all the previous analyzed tissues. The plot for PMF evolution over 9 days of FF is shown in figure 5.17.

Unlike all the other tissues, there is only a slight PMF increase in the first 5 days in formalin, followed by an even smaller phosphorus decrease over the next 4 days. Since the baseline PMF is significantly higher for the spleen, the phosphorus balance between the tissue and the formalin might not be as critical and the PMF shift might be much smaller. This leads to the observed pattern in the figure, which almost forms a PMF plateau along the 9-day FF period when contrasting with the remaining tissues.

5.3.4 Muscle tissue

The muscle tissue data sets were handled in the same way as they were for sodium quantification. The phosphorus peak for the 328-48h and the 329-fresh samples was not noticeable in the gamma spectra and is not part of the presented data. Individual plots for PMF as a function of FF time for each muscle data set are presented in I.

All data points from all samples are represented in figure 5.18. In the decluttering process, the 329-24h data point was removed to achieve a better overall data trend. The plot with the average data from all the samples is illustrated in figure 5.19.

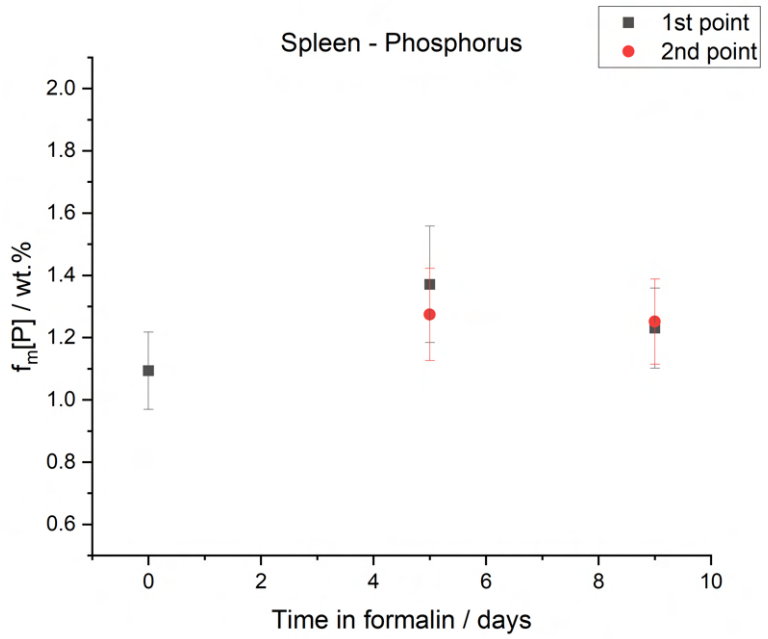

Figure 5.17: Plot of phosphorus mass fraction as a function of FF time for the spleen data set.

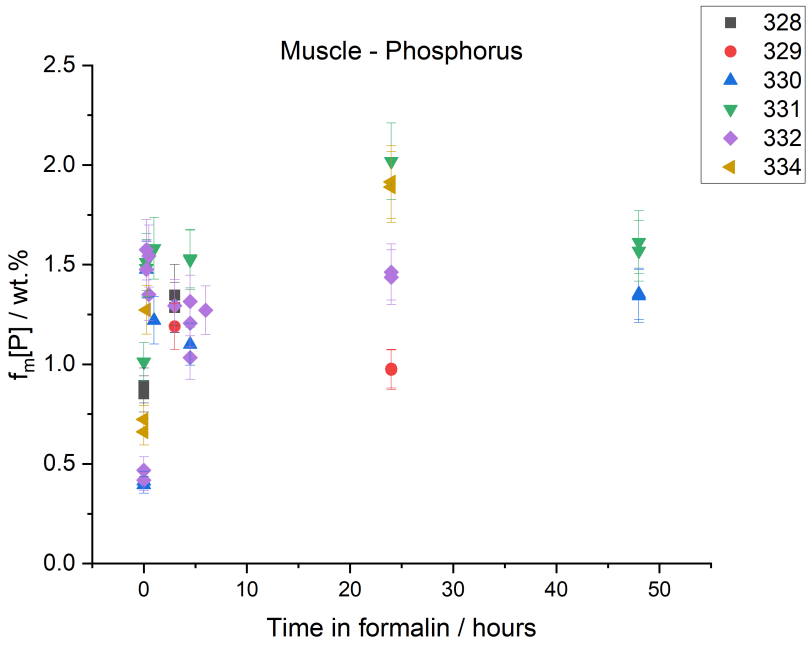

Figure 5.18: Plot of phosphorus mass fraction as a function of FF time for the muscle data sets.

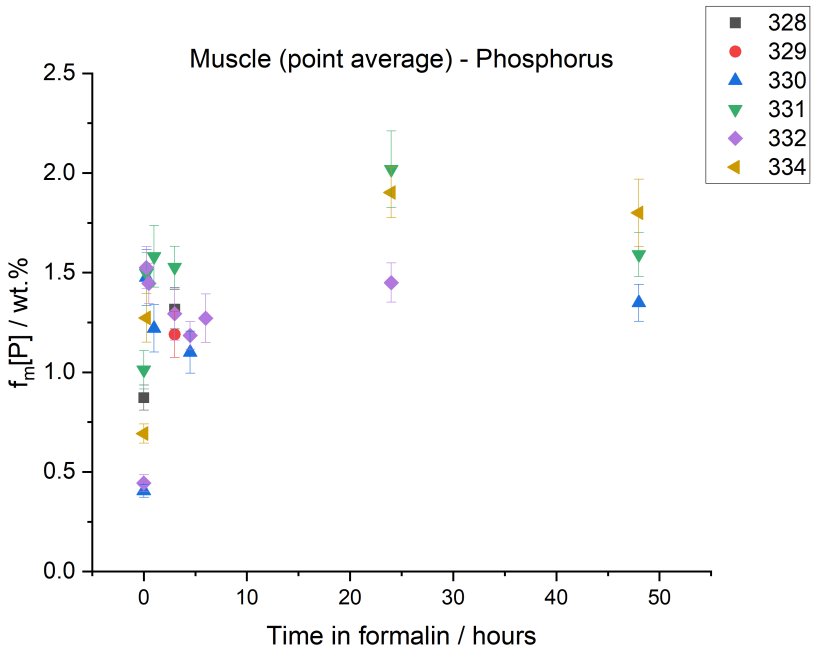

Figure 5.19: Plot of phosphorus mass fraction as a function of FF time for the muscle data sets. Each data point is an average value of data points from the same sample.

By performing the point average some plot features start to become clearer. There seems to be an instantaneous phosphorus rise within the first minutes of FF, followed by a small decline in the next few hours. At the 24-hour time mark there is a PMF peak and at the 48-hour mark there is a noticeable falloff, just as observed for the SMF.

The final data cleanup was then performed by calculating the average value of all data points corresponding to the same FF time, just as it was done for sodium. This data plot is displayed in figure 5.20.

The PMF sample average curve is slightly different from the SMF sample average curve. According to the data in the figure, there isn't a continuous increase of the PMF until the peak, but instead there is a rapid rise in the first 30 minutes of FF that leads to a slight falloff and a subsequent plateau between the 3h and the 6h time marks. After this point, the PMF behaves just like the SMF did. There is a substantial increase of phosphorus after 24 hours of formalin storage followed by a PMF diminishing in the 24 hours after that point.

5.4 Aluminium measurements

Aluminium was mentioned throughout this work as a quantifiable element and the areas of its gamma peaks were extracted just like they were for sodium and phosphorus, for the reason that there was interest in knowing whether the analyzed soft tissue samples had any amount of this element in them. The observed pattern in the extracted areas

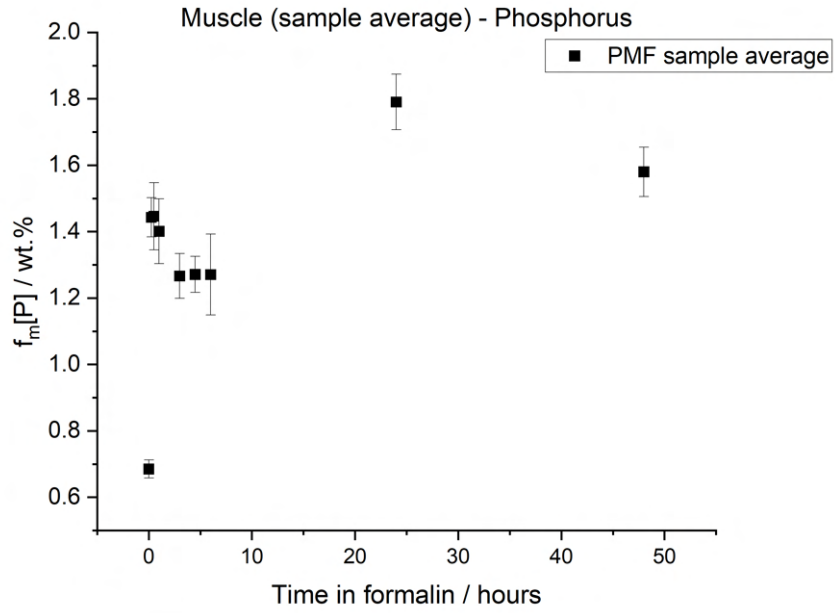

Figure 5.20: Plot of phosphorus mass fraction as a function of FF time for the muscle data sets. Each data point is an average value of data points from all samples with the same FF time.

led to believe that aluminium was not only not present in the tissue samples, but its presence in the gamma spectra was also a byproduct of poor sample conditioning or beam misplacement, due to interactions with the chamber walls, the target holders or the aluminium foil keeping the samples in place.

With this in mind, while running the ERYA-Bulk simulations, aluminium was not accounted for as one of the elements present in the samples.

Figure 5.21 shows the correlation between the conditioning of the sample with the greatest aluminium gamma yield and the area of the respective peaks.

It is clear that the sample was severely fractured, which might have led to the proton beam hitting the aluminium foil behind it. The areas of the 844 keV and 1014 keV gamma peaks represented in the figure were on par with those registered for the 440 keV sodium peak- The 844 keV peak had an area of 29749 and the 1014 keV peak had an area of 41842, while sodium 440 keV had an area of 46522. In addition to this, background gamma spectra and EBS spectra were taken without any samples in the chamber. The gamma spectra kept showing aluminium peaks, but there was no sign of either sodium or phosphorus peaks, which comes to show that the gamma-rays for both these elements were only coming from the samples, while aluminium gamma-rays resulted from interactions somewhere else. The background EBS spectra did not reveal any sodium or phosphorus as well. Since well-assembled samples had no or barely any aluminium in their gamma spectra and since aluminium was not used for the EBS spectra

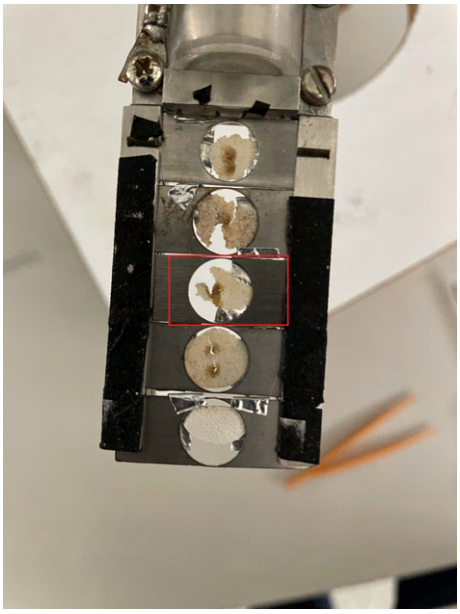

(a) Sample 330 4h30h in formalin.

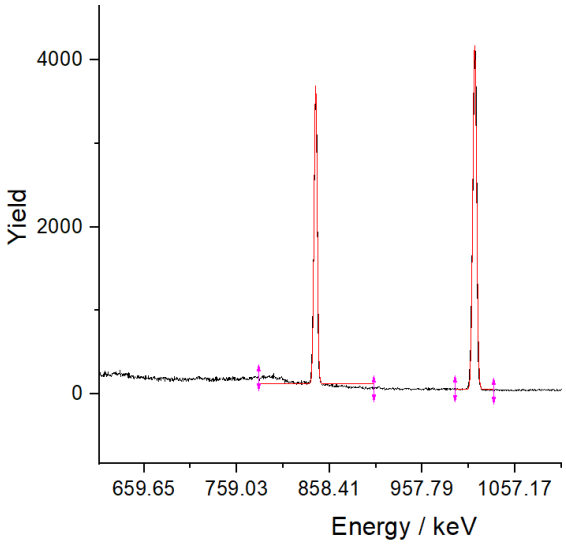

(b) Sample 330 4h30 aluminium gamma peaks.

Figure 5.21: Correlation between sample conditioning and the respective aluminium gamma peaks

analysis, its quantification as part of the biological samples was discarded.

6

Conclusions

The fundamental objective of this work was to quantify light elements in formalin-fixated biological samples over increasing periods of time and to parameterize the evolution curve of their respective mass fractions in the samples. The chosen method to achieve this goal had the main advantage of having a much better sensitivity for lighter elements (such as sodium) when compared to the methods used so far for research in this field, namely XRF. The experimental conditions used throughout this work only allowed the quantification of phosphorus and sodium. Aluminium was also very detectable but, as stated before, it appeared as a byproduct of poor sample conditioning. Other elements were also identifiable in the gamma spectra but were not compelling for this work's end results.

There were some adversities regarding sample collection throughout the duration of this study. Whereas the organ samples (colon, ileon and spleen) had very suitable pellets for analysis due to their size and thickness, the muscle tissue samples were very small, which led to little powder yields after grinding. This presented a problem while making the pellets, since most of the samples simply lacked enough powder. Most of the pellets either crumbled into dust right away of were too thin or poorly shaped for analysis. XRF technique had ways to bypass this problem, but for PIGE analysis this meant a loss of available samples, hence the existence of some data gaps in this work's results.

In spite of this, this work achieved very interesting conclusions. For the organ tissues, the sodium and phosphorus behaviour over several days shows, on average, there is a rise of their mass fraction until the 5 to 9-day time mark, followed by a slight falloff in the days after. For the muscle tissue, the parameterization curves showed very promising results, with fast sodium and phosphorus increases in the first minutes of FF and then a steady rise for sodium and a small decline followed by a plateau for phosphorus. Additionally, the existence of two viable gamma peaks for sodium quantification was very useful to verify the achieved results.

For future work, there are some aspects that can be improved upon. Firstly, this type of analysis requires more extensive data sets, as well as samples with bigger volumes to avoid the waste of tissue if the pellets are unfit for analysis with this method. Furthermore,

trying to analyze the formalin respective to each sample, as well as obtaining its chemical formula, might help to verify the outcome of this work, since the element behaviour in formalin should be the opposite to that verified for the tissues, in order to maintain the system elementary balance. Finally, one of the hardships of this work was coming to terms with the hydrogen atomic percentage in the tissues to proceed with the EBS analysis. There are a few ion beam analysis techniques and other methods that allow measurements of hydrogen. Adding one of these techniques to the lyophilized sample analysis would prove invaluable for an even more accurate hydrogen estimation.

This thesis sought to achieve a preliminary study regarding how tissue composition changes during preservation in formalin. Hopefully, the next steps in this area take a closer look at cancer tissue and its composition in comparison with healthy tissue. By fixating cancer tissue samples in formalin for posterior studies, it will be important to keep in mind not only the structural changes of the tissue caused by the presence of cancer cells, but also the formalin-induced elementary changes. If both these studies are merged, further knowledge about cancer and its diagnostics becomes a very realistic prospect.

Bibliography

[1] J. M. Lourenço. *The NOVAthesis LaTeX Template User's Manual*. NOVA University Lisbon. 2021. URL: https://github.com/joaomlourenco/novathesis/raw/master/template.pdf (cit. on p. iii).

[2] R. J. D. Berardinis and N. S. Chandel. "Fundamentals of cancer metabolism". In: *Science Advances* 2 (5 May 2016). ISSN: 23752548. DOI: 10.1126/sciadv.1600200 (cit. on p. 1).

[3] J. Ferlay et al. "Estimating the global cancer incidence and mortality in 2018: GLOBOCAN sources and methods". In: *International Journal of Cancer* 144 (8 Apr. 2019), pp. 1941–1953. ISSN: 10970215. DOI: 10.1002/ijc.31937 (cit. on p. 1).

[4] J. Ferlay et al. "Cancer statistics for the year 2020: An overview". In: *International Journal of Cancer* 149 (4 Aug. 2021), pp. 778–789. ISSN: 10970215. DOI: 10.1002/ijc.33588 (cit. on p. 1).

[5] H. Sung et al. "Global Cancer Statistics 2020: GLOBOCAN Estimates of Incidence and Mortality Worldwide for 36 Cancers in 185 Countries". In: *CA: A Cancer Journal for Clinicians* 71 (3 May 2021), pp. 209–249. ISSN: 0007-9235. DOI: 10.3322/caac.21660 (cit. on p. 1).

[6] S. A. Silvera and T. E. Rohan. "Trace elements and cancer risk: A review of the epidemiologic evidence". In: *Cancer Causes and Control* 18 (1 Feb. 2007), pp. 7–27. ISSN: 09575243. DOI: 10.1007/s10552-006-0057-z (cit. on p. 1).

[7] R. Mateus et al. "The sensitivity of the PIGE analytical technique". In: *Nuclear Instruments and Methods in Physics Research, Section B: Beam Interactions with Materials and Atoms* 264 (2 Nov. 2007), pp. 340–344. ISSN: 0168583X. DOI: 10.1016/j.nimb.2007.09.030 (cit. on p. 1).

[8] T. R. Rautray et al. "Analysis of blood and tissue in gallbladder cancer". In: *Nuclear Instruments and Methods in Physics Research, Section B: Beam Interactions with Materials and Atoms* 267 (17 Sept. 2009), pp. 2878–2883. ISSN: 0168583X. DOI: 10.1016/j.nimb.2009.06.084 (cit. on p. 1).

[9] I. M. Leiva, M. R. Emmert-Buck, and J. W. Gillespie. *Molecular Profiling Studies 27 Handling of Clinical Tissue Specimens for Molecular Profiling Studies*. 2003, pp. 27–35 (cit. on pp. 1, 6–8).

[10] S. Cacciatore et al. "Metabolic profiling in formalin-fixed and paraffin-embedded prostate cancer tissues". In: *Molecular Cancer Research* 15 (4 Apr. 2017), pp. 439–447. ISSN: 15573125. DOI: 10.1158/1541-7786.MCR-16-0262 (cit. on p. 2).

[11] "International Atomic Energy Agency inter-comparison of particle induced gamma-ray emission codes for bulk samples". In: *Nuclear Instruments and Methods in Physics Research, Section B: Beam Interactions with Materials and Atoms* 468 (Apr. 2020), pp. 37–47. ISSN: 0168583X. DOI: 10.1016/j.nimb.2020.02.019 (cit. on pp. 2, 24).

[12] S. Pirkmajer and A. V. Chibalin. "ATPase regulation in skeletal muscle". In: *Am J Physiol Endocrinol Metab* 311 (2016), pp. 1–31. DOI: 10.1152/ajpendo.00539.2015.-Skeletal. URL: http://www.ajpendo.org (cit. on pp. 3, 4).

[13] S. V. Pierre and Z. Xie. "The Na, K-ATPase receptor complex". In: *Cell biochemistry and biophysics* 46.3 (2006), pp. 303–315 (cit. on pp. 3, 4).

[14] A. G. Therien and R. Blostein. *invited review Mechanisms of sodium pump regulation*. 2000. URL: http://www.ajpcell.org (cit. on p. 4).

[15] P. L. Jørgensen. *Structure, function and regulation of Na,K-ATPase in the kidney*. 1986, pp. 10–20 (cit. on p. 4).

[16] E. Féraille and A. Doucet. *Sodium-Potassium-Adenosinetriphosphatase-Dependent Sodium Transport in the Kidney: Hormonal Control*. 2001. URL: http://physrev.physiology.org (cit. on p. 4).

[17] A. A. McDonough and R. A. Farley. "Regulation of Na, K-ATPase activity." In: *Current opinion in nephrology and hypertension* 2.5 (1993), pp. 725–734 (cit. on p. 4).

[18] N. K. Aras and O. Y. Ataman. *Trace element analysis of food and diet*. Royal Society of Chemistry, 2007 (cit. on p. 5).

[19] C. S. R. d. S. Silva. "Desenvolvimento de Metodologias para Análise Elementar de Osso com Patologia". In: (2016) (cit. on pp. 6, 22, 24).

[20] S. B. Goldhaber. "Trace element risk assessment: Essentiality vs. toxicity". In: *Regulatory Toxicology and Pharmacology* 38 (2 2003), pp. 232–242. ISSN: 02732300. DOI: 10.1016/S0273-2300(02)00020-X (cit. on p. 6).

[21] J. Puhar et al. "Reduction of cost, energy and emissions of the formalin production process via methane steam reforming". In: *Systems* 9 (1 Jan. 2021), pp. 1–17. ISSN: 20798954. DOI: 10.3390/systems9010005 (cit. on p. 6).

[22] E. Brenner. "Human body preservation - old and new techniques". In: *Journal of Anatomy* 224 (3 Mar. 2014), pp. 316–344. ISSN: 00218782. DOI: 10.1111/joa.12160 (cit. on p. 6).

[23] A. A. Fonseca et al. "Effect of 10% formalin on radiographic optical density of bone specimens". In: *Dentomaxillofacial Radiology* 37 (3 Mar. 2008), pp. 137–141. ISSN: 0250832X. DOI: 10.1259/dmfr/18109064 (cit. on p. 6).

[24] A. Kouchmeshky. *Snap Freezing Retinoid Signaling Pathways*, p. 2020 (cit. on pp. 7, 8).

[25] "Histopathology procedures: from tissue sampling to histopathological evaluation." In: *Methods in molecular biology (Clifton, N.J.)* 691 (2011), pp. 69–82. ISSN: 19406029. DOI: 10.1007/978-1-60761-849-2_4 (cit. on pp. 7, 8).

[26] O. Zhanmu et al. "Paraffin-embedding for large volume bio-tissue". In: *Scientific Reports* 10 (1 Dec. 2020). ISSN: 20452322. DOI: 10.1038/s41598-020-68876-5 (cit. on p. 8).

[27] A. Sadeghipour and P. Babaheidarian. *Making formalin-fixed, paraffin embedded blocks*. Vol. 1897. Humana Press Inc., 2019, pp. 253–268. DOI: 10.1007/978-1-4939-8935-5_22 (cit. on p. 8).

[28] W. D. Newhauser and R. Zhang. *The physics of proton therapy*. Apr. 2015. DOI: 10.1088/0031-9155/60/8/R155 (cit. on pp. 9–14).

[29] H. Paganetti. *Proton therapy physics*. CRC press, 2018 (cit. on pp. 9, 10).

[30] R. C. Bird and J. S. Williams. *Ion beams for materials analysis*. Elsevier, 1989 (cit. on pp. 9–11).

[31] A. J. Lomax. *Charged Particle Therapy: The Physics of Interaction*. 2009. URL: www.journalppo.com (cit. on pp. 10, 14).

[32] H. Paganetti. *Range uncertainties in proton therapy and the role of Monte Carlo simulations*. June 2012. DOI: 10.1088/0031-9155/57/11/R99 (cit. on p. 11).

[33] C. A. Bertulani and P. Danielewicz. *Introduction to Nuclear Reactions*. 2003. URL: http://www.copyright.com/ (cit. on p. 14).

[34] J. R. Tesmer and M. Nastasi. "Handbook of modern ion beam materials analysis". In: *Materials Research Society, 9800 McKnight Rd, Suite 327, Pittsburgh, PA 15237, USA, 1995. 700* (1995) (cit. on pp. 14–16, 22, 42).

[35] M. Mayer. *Rutherford Backscattering Spectrometry (RBS)* (cit. on pp. 14–17).

[36] G. Butcher. *Tour of the electromagnetic spectrum*. Government Printing Office, 2016 (cit. on pp. 17, 18, 21, 22).

[37] M. Ragheb. "Gamma Rays Interaction with matter". In: *Nuclear, Plasma and Radiation Science. Inventing the Future," https://netfiles. uiuc. edu/mragheb/www* (2011) (cit. on pp. 17–22).

[38] C. Leroy and P.-G. Rancoita. *Principles of radiation interaction in matter and detection*. World Scientific, 2009 (cit. on pp. 18, 21, 22).

[39] IAEA. *Development of a Reference Database for Particle Induced Gamma Ray Emission (PIGE) Spectroscopy*. IAEA, 2017, p. 246. ISBN: 9789201063175 (cit. on pp. 22–24).

[40] V. J. Bush et al. *Essential and Toxic Element Concentrations in Fresh and Formalin-Fixed Human Autopsy Tissues*. 1995, pp. 284–294. URL: https://academic.oup.com/clinchem/article/41/2/284/5646077 (cit. on p. 25).

[41] "Leaching of trace elements from biological tissue by formalin fixation". In: *Biological Trace Element Research* 121 (3 Mar. 2008), pp. 221–225. ISSN: 01634984. DOI: 10.1007/s12011-007-8051-1 (cit. on p. 25).

[42] A. Matusch, A. Bauer, and J. S. Becker. "Element imaging in formalin fixed slices of human mesencephalon". In: *International Journal of Mass Spectrometry* 307 (1-3 Oct. 2011), pp. 240–244. ISSN: 13873806. DOI: 10.1016/j.ijms.2011.03.006 (cit. on p. 25).

[43] C. H. Chen et al. "Shrinkage of head and neck cancer specimens after formalin fixation". In: *Journal of the Chinese Medical Association* 75 (3 Mar. 2012), pp. 109–113. ISSN: 17264901. DOI: 10.1016/j.jcma.2012.02.006 (cit. on p. 26).

[44] H. S. Park et al. "Effect of formalin fixation and tumour size in small-sized non-small-cell lung cancer: a prospective, single-centre study". In: *Histopathology* 71 (3 Sept. 2017), pp. 437–445. ISSN: 13652559. DOI: 10.1111/his.13237 (cit. on p. 26).

[45] C. Horn and C. Naugler. "Breast specimen shrinkage following formalin fixation". In: *Pathology and Laboratory Medicine International* (Feb. 2014), p. 11. ISSN: 1179-2698. DOI: 10.2147/plmi.s59842 (cit. on p. 26).

[46] B. Pritt et al. "The effect of tissue fixation and processing on breast cancer size". In: *Human Pathology* 36 (7 July 2005), pp. 756–760. ISSN: 00468177. DOI: 10.1016/j.humpath.2005.04.018 (cit. on p. 26).

[47] S. Jonmarker et al. "Tissue shrinkage after fixation with formalin injection of prostatectomy specimens". In: *Virchows Archiv* 449 (3 Sept. 2006), pp. 297–301. ISSN: 09456317. DOI: 10.1007/s00428-006-0259-5 (cit. on p. 26).

[48] J. Vent et al. "Influence of formalin fixation on tissue dimensions in palatal tonsils". In: *Pathology Research and Practice* 210 (1 Jan. 2014), pp. 59–61. ISSN: 03440338. DOI: 10.1016/j.prp.2013.10.002 (cit. on p. 26).

[49] A. F. O. E. da Veiga. *Influence of paraffin embedding in the analysis of human biopsied soft tissue*. 2021 (cit. on pp. 26, 28, 33).

[50] M. L. Carvalho et al. *Trace elements in human cancerous and healthy tissues: A comparative study by EDXRF, TXRF, synchrotron radiation and PIXE*. Sept. 2007. DOI: 10.1016/j.sab.2007.03.030 (cit. on p. 27).

[51] S. J. Mulware. *Comparative trace elemental analysis in cancerous and noncancerous human tissues using PIXE*. 2013. DOI: 10.1155/2013/192026 (cit. on p. 27).

[52] T. Magalhães et al. "Study on trace elements behaviour in cancerous and healthy tissues of colon, breast and stomach: Total reflection X-ray fluorescence applications". In: vol. 65. Elsevier, 2010, pp. 493–498. DOI: 10.1016/j.sab.2010.04.001 (cit. on p. 27).

[53] H. F. Luis. *Study of nuclear reactions relevant for Astrophysics by Micro-AMS*. 2013 (cit. on pp. 30, 31).

[54] M. J. dos Santos Moreira da Silva. *Optimization and Automation of the Nuclear Reaction Chamber*. 2021 (cit. on pp. 30, 31).

[55] H. M. M. F. da Silva. *Elastic scattering of protons and oxygen ions from light nuclei*. 2018 (cit. on pp. 30–33).

[56] H. G. Moser. *Silicon detector systems in high energy physics*. July 2009. DOI: 10.1016/j.ppnp.2008.12.002 (cit. on p. 33).

[57] M. U. Khandaker. "High purity germanium detector in gamma-ray spectrometry". In: *International Journal of Fundamental Physical Sciences* 1 (2 June 2011), pp. 42–46. DOI: 10.14331/ijfps.2011.330011 (cit. on p. 33).

[58] N. P. Barradas and C. Jeynes. "Advanced physics and algorithms in the IBA DataFurnace". In: *Nuclear Instruments and Methods in Physics Research, Section B: Beam Interactions with Materials and Atoms* 266 (8 Apr. 2008), pp. 1875–1879. ISSN: 0168583X. DOI: 10.1016/j.nimb.2007.10.044 (cit. on p. 38).

I

Annex 1 - Plots of SMF and PMF for individual muscle data sets

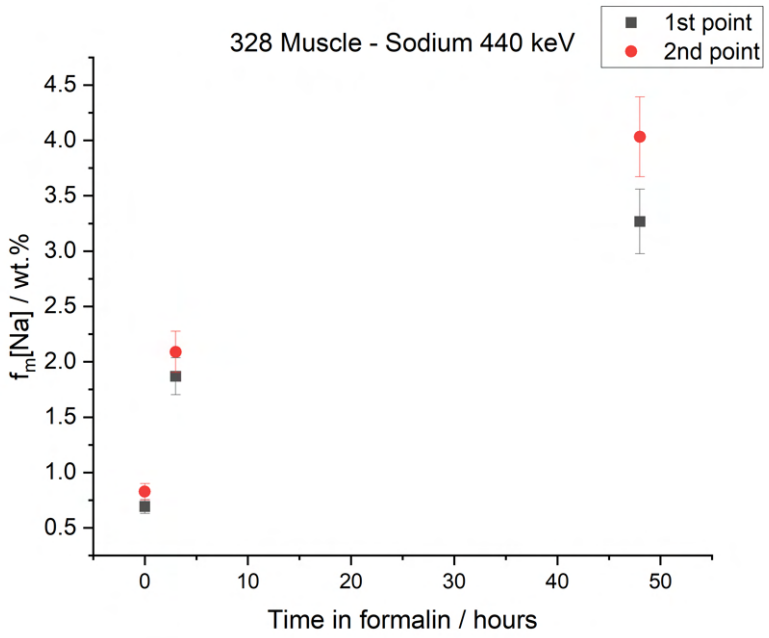

Figure I.1: Plot of sodium mass fraction as a function of FF time for the 328 muscle data set, using the 440 keV peak.

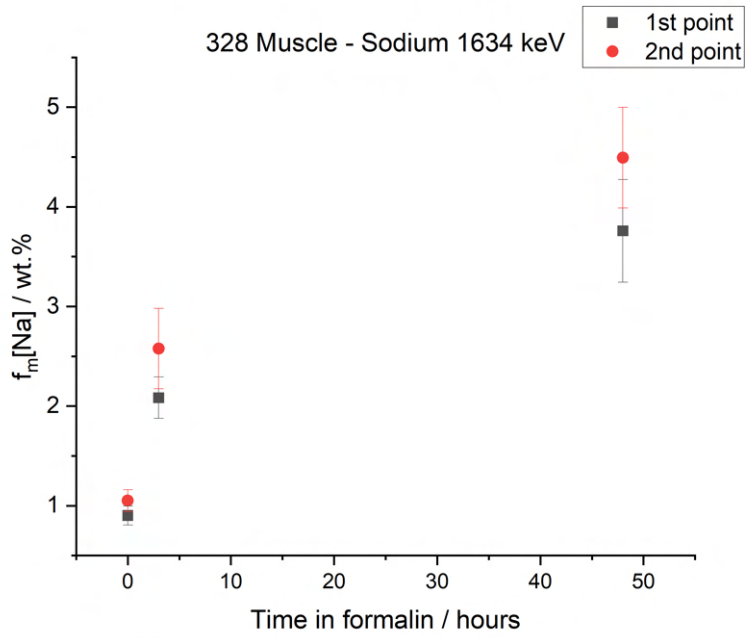

Figure I.2: Plot of sodium mass fraction as a function of FF time for the 328 muscle data set, using the 1634 keV peak.

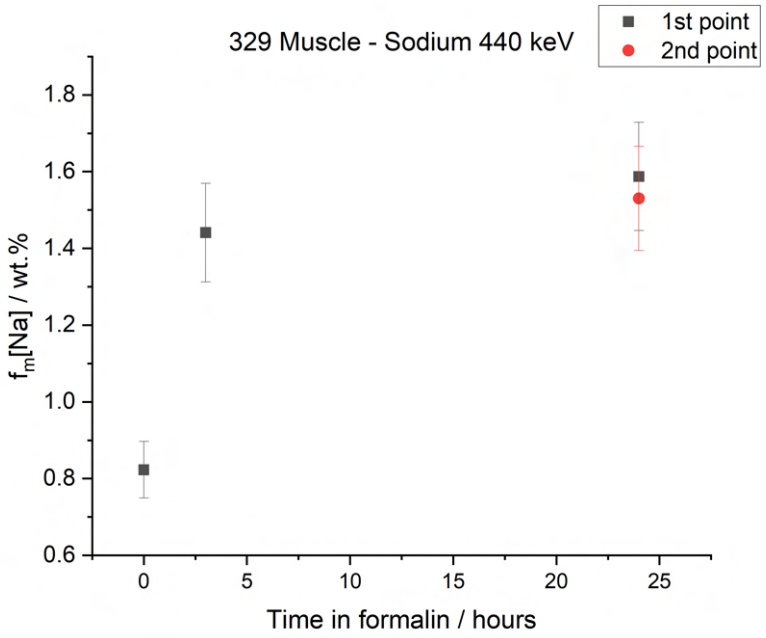

Figure I.3: Plot of sodium mass fraction as a function of FF time for the 329 muscle data set, using the 440 keV peak.

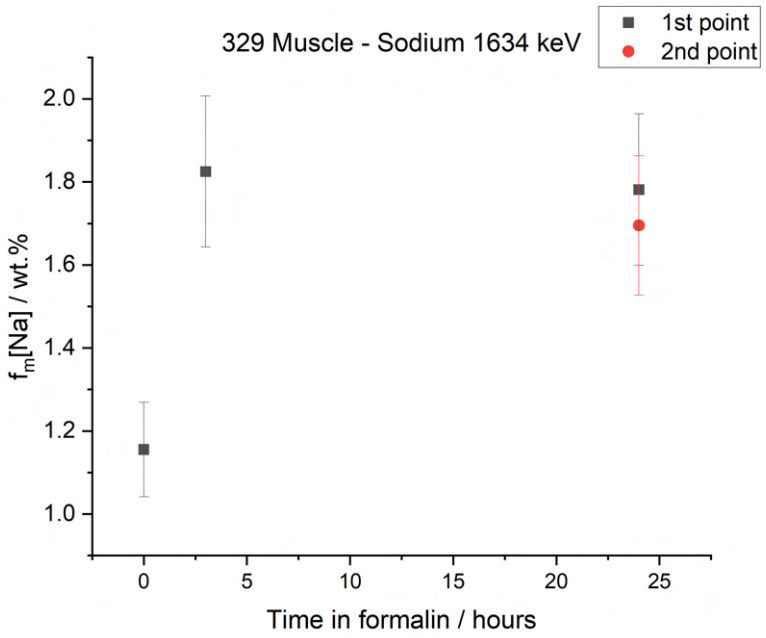

Figure I.4: Plot of sodium mass fraction as a function of FF time for the 329 muscle data set, using the 1634 keV peak.

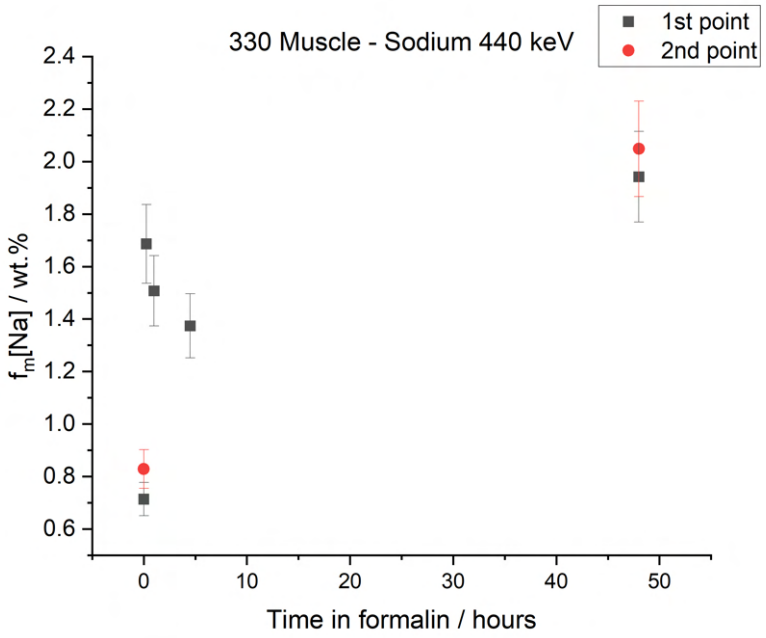

Figure I.5: Plot of sodium mass fraction as a function of FF time for the 330 muscle data set, using the 440 keV peak.

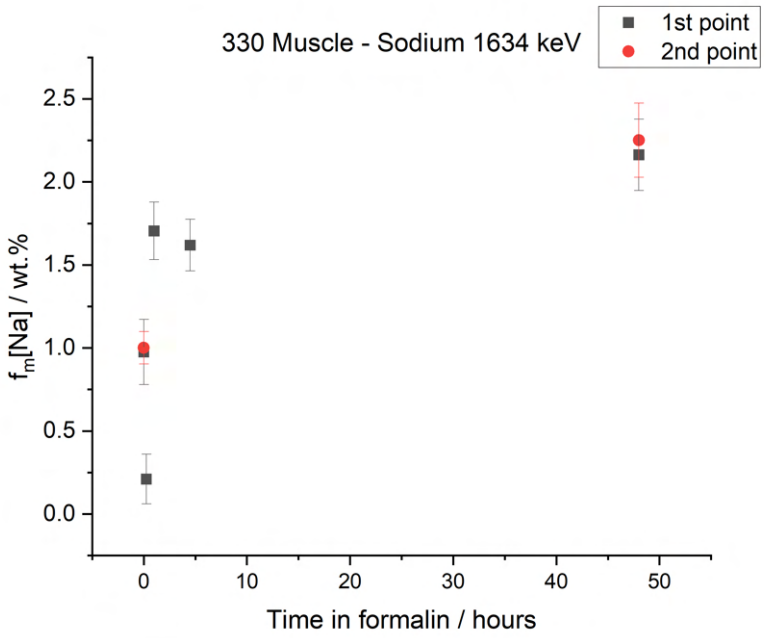

Figure I.6: Plot of sodium mass fraction as a function of FF time for the 330 muscle data set, using the 1634 keV peak.

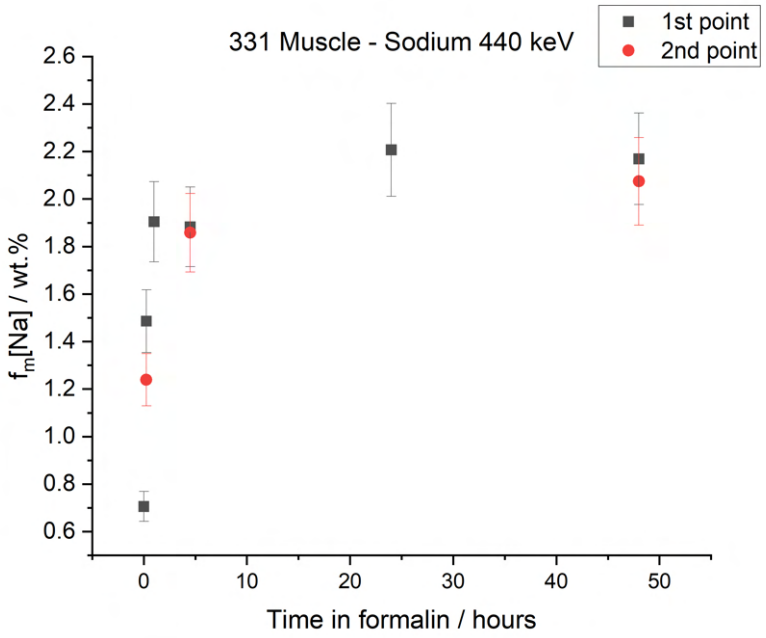

Figure I.7: Plot of sodium mass fraction as a function of FF time for the 331 muscle data set, using the 440 keV peak.

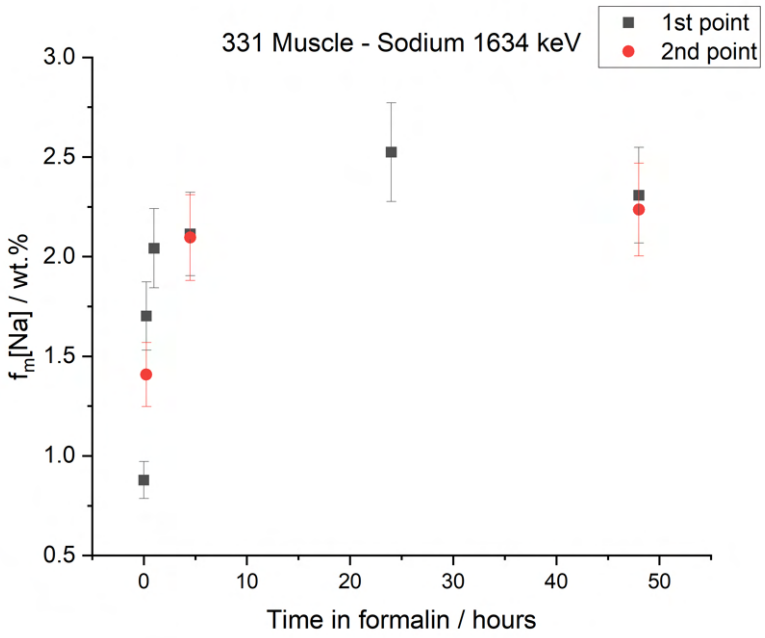

Figure I.8: Plot of sodium mass fraction as a function of FF time for the 331 muscle data set, using the 1634 keV peak.

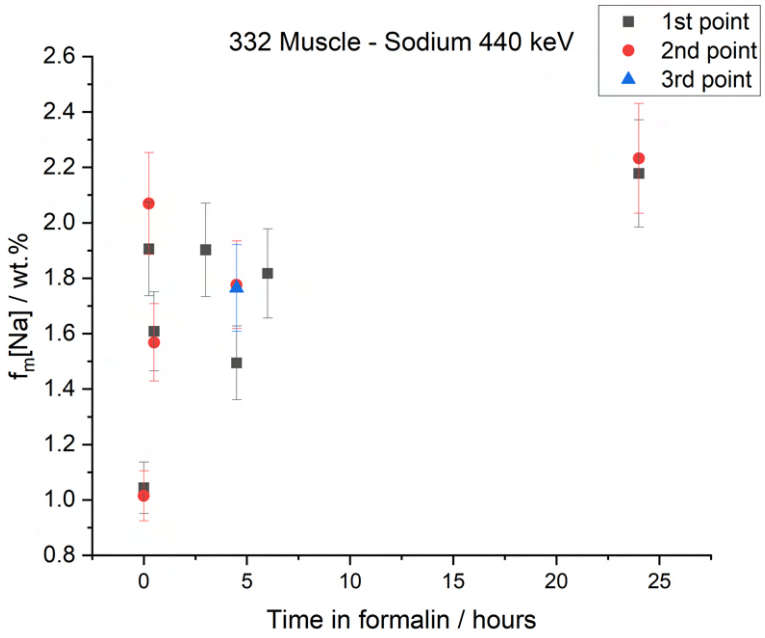

Figure I.9: Plot of sodium mass fraction as a function of FF time for the 332 muscle data set, using the 440 keV peak.

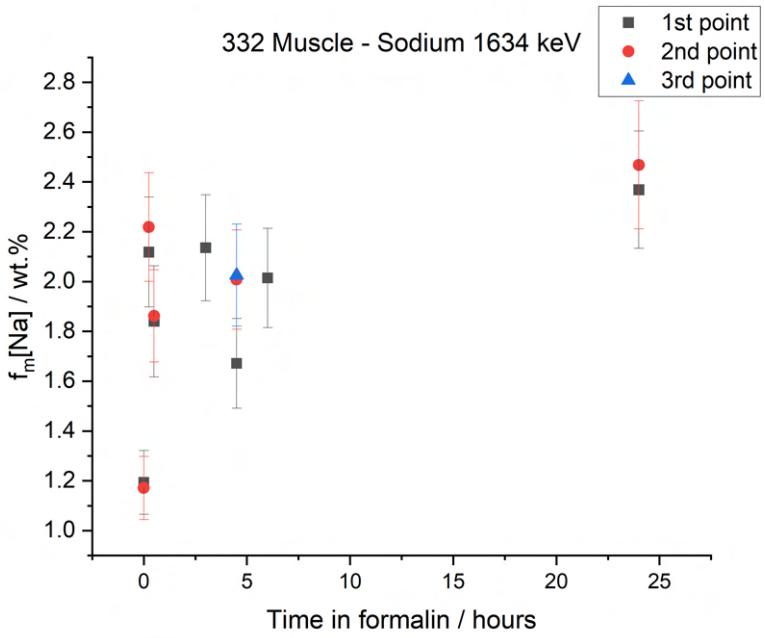

Figure I.10: Plot of sodium mass fraction as a function of FF time for the 332 muscle data set, using the 1634 keV peak.

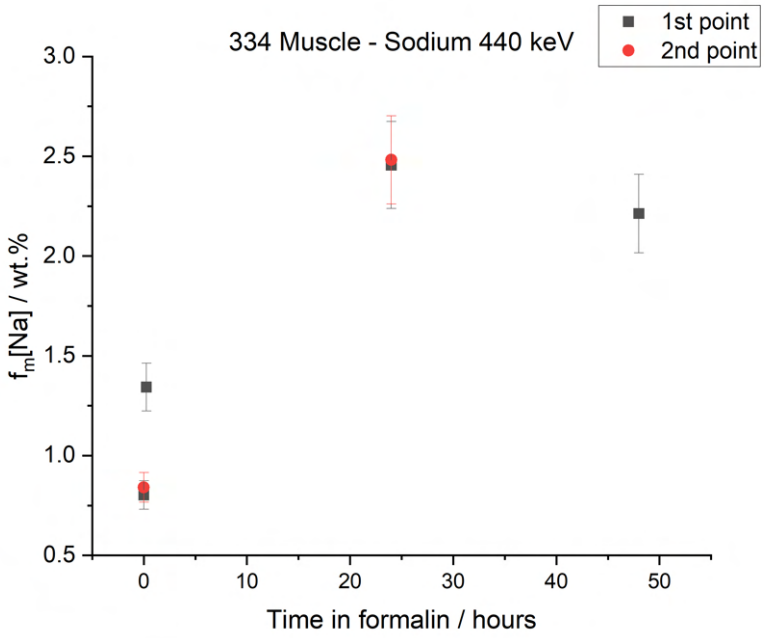

Figure I.11: Plot of sodium mass fraction as a function of FF time for the 334 muscle data set, using the 440 keV peak.

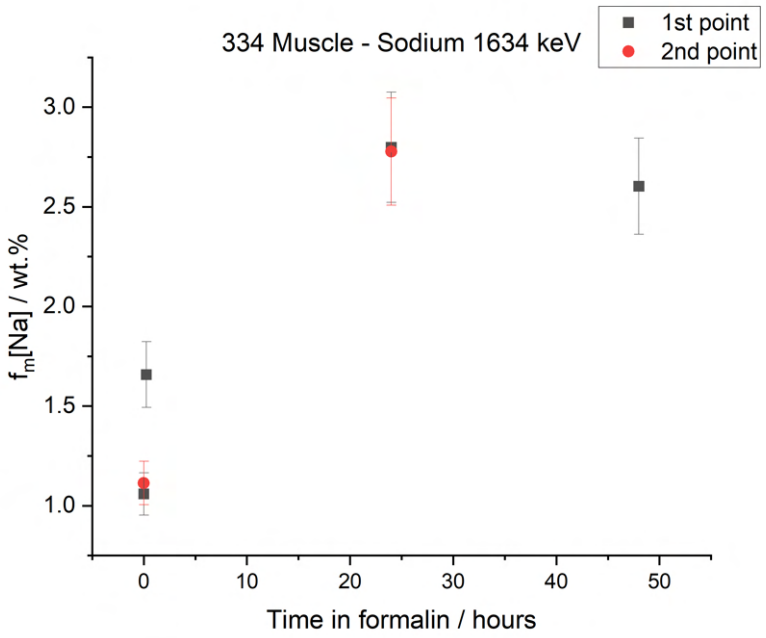

Figure I.12: Plot of sodium mass fraction as a function of FF time for the 334 muscle data set, using the 1634 keV peak.

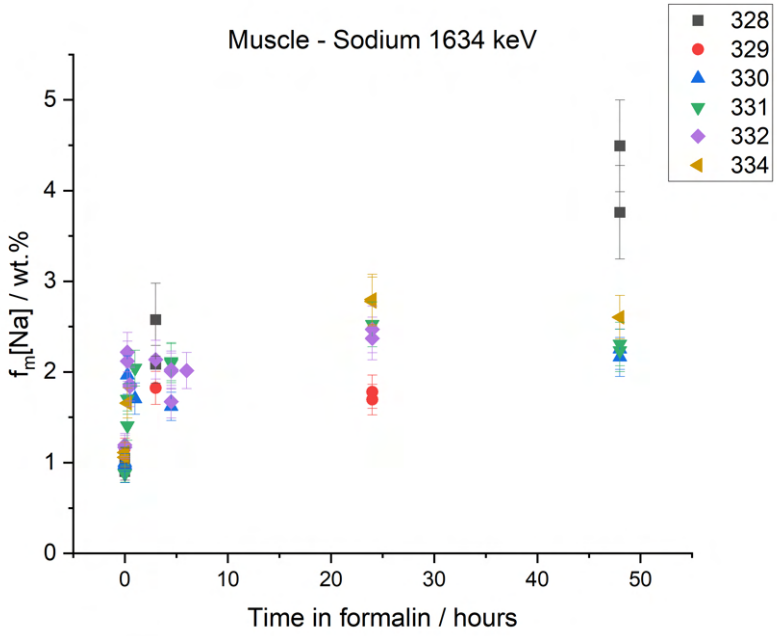

Figure I.13: Plot of sodium mass fraction as a function of FF time for the muscle data sets, using the 1634 keV peak.

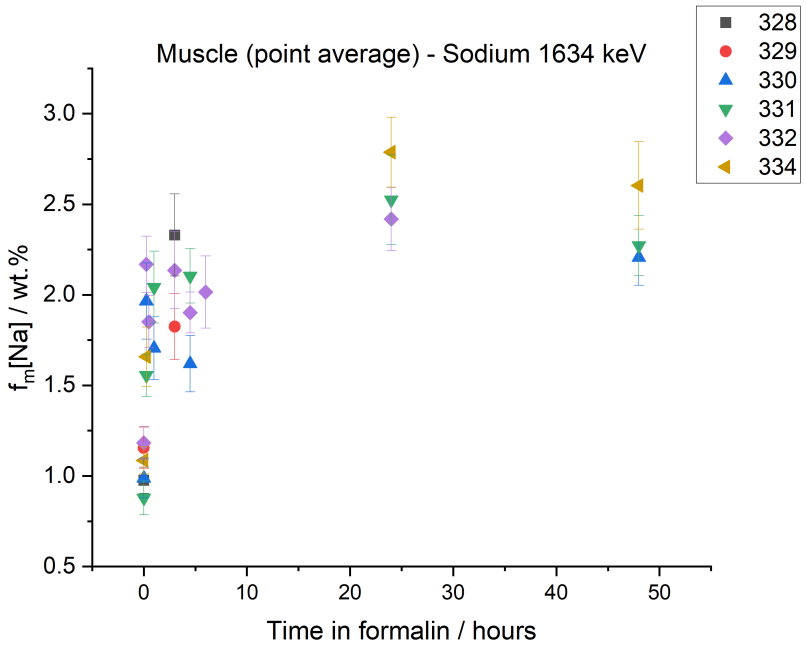

Figure I.14: Plot of sodium mass fraction as a function of FF time for the muscle data sets, using the 1634 keV gamma peak. Each data point in the plot is an average value of data points from the same sample.

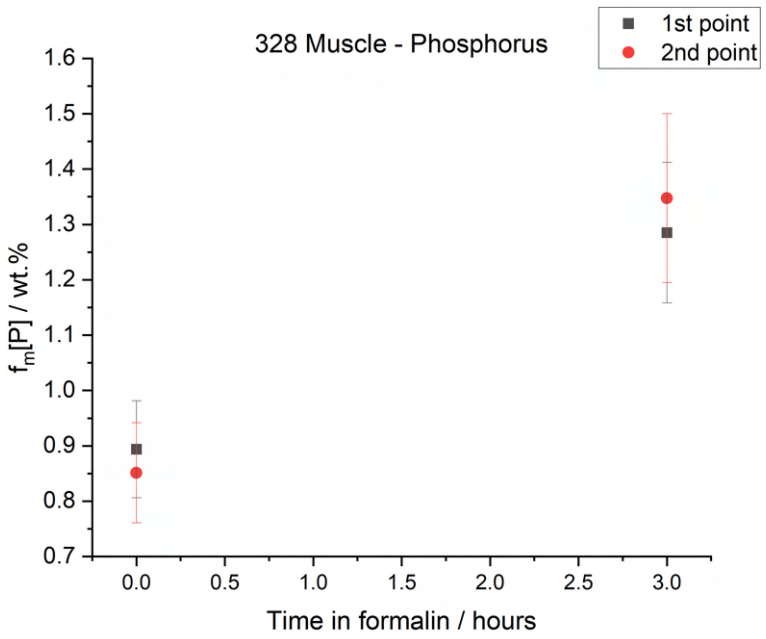

Figure I.15: Plot of phosphorus mass fraction as a function of FF time for the 328 muscle data set.

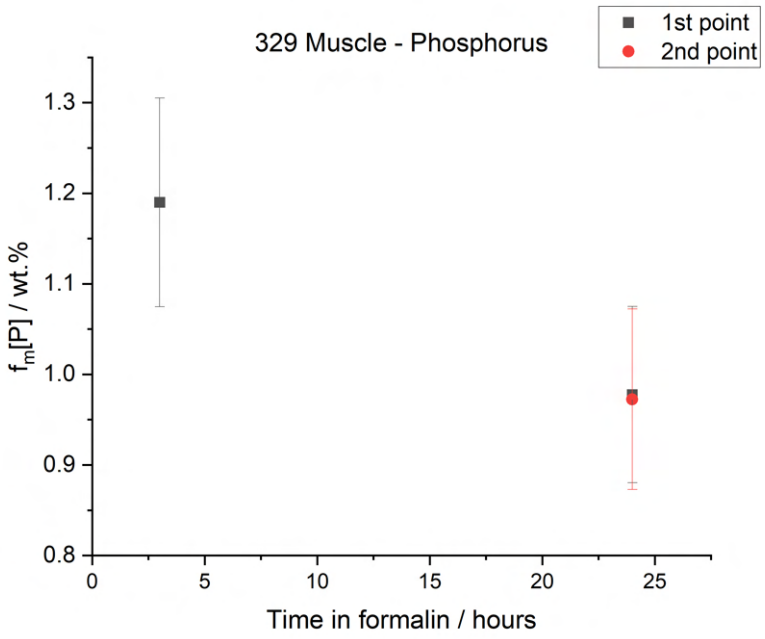

Figure I.16: Plot of phosphorus mass fraction as a function of FF time for the 329 muscle data set.

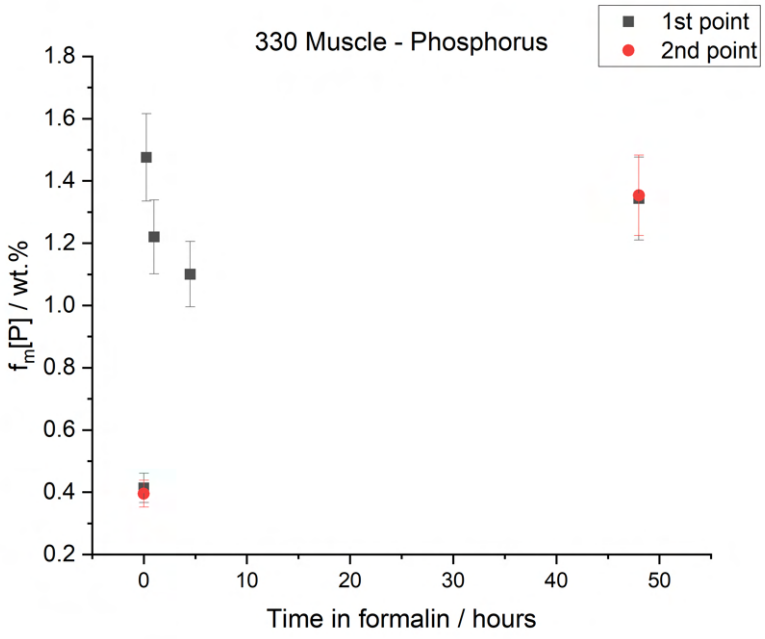

Figure I.17: Plot of phosphorus mass fraction as a function of FF time for the 330 muscle data set.

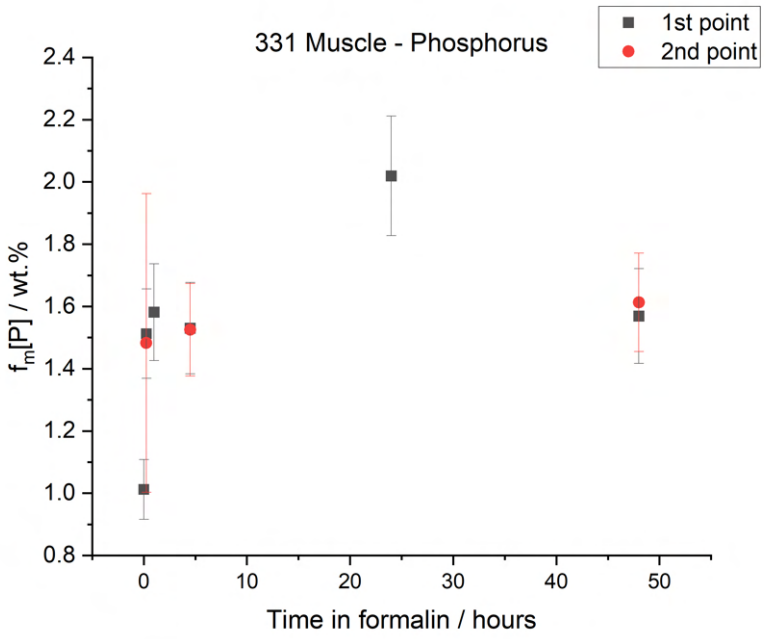

Figure I.18: Plot of phosphorus mass fraction as a function of FF time for the 331 muscle data set.

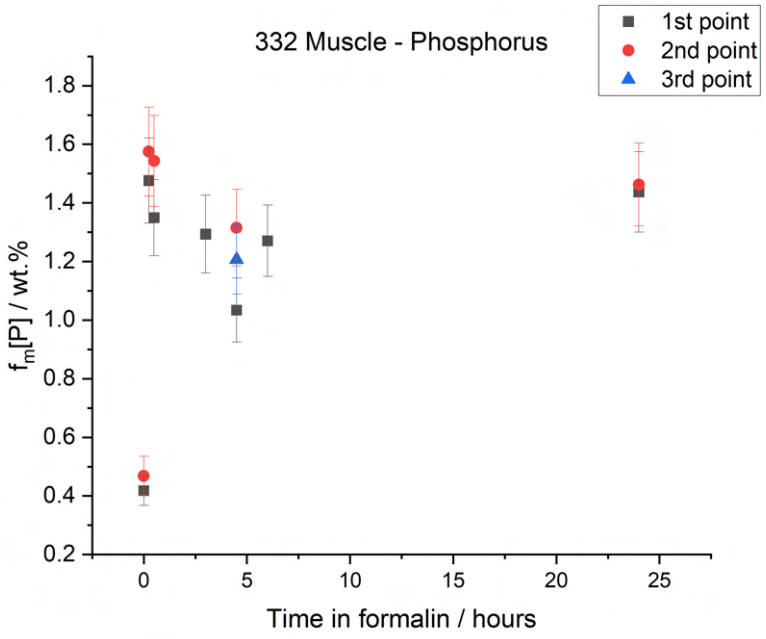

Figure I.19: Plot of phosphorus mass fraction as a function of FF time for the 332 muscle data set.

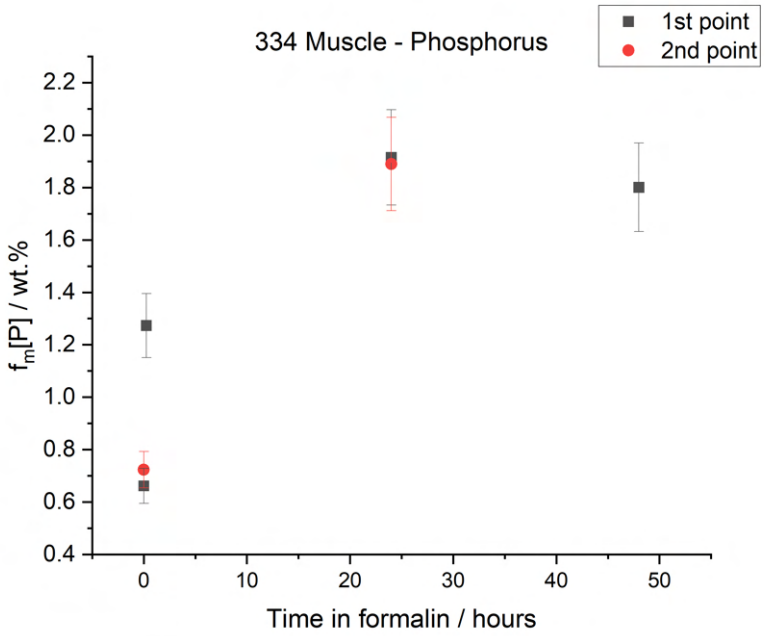

Figure I.20: Plot of phosphorus mass fraction as a function of FF time for the 334 muscle data set.